Combined theoretical-experimental study of chromium doped zinc gallate phosphor

Arthur De Vos

Supervisors: Prof. Dr. ir. Karen Hemelsoet, Prof. Dr. Philippe Smet
Counsellors: Dr. Dr. Danny Vanpoucke, Dr. ir. Kurt Lejaeghere, Jonas Joos

Master's dissertation submitted in order to obtain the academic degree of
Master of Science in Engineering Physics

Department of Applied Physics
Chairman: Prof. Dr. ir. Christophe Leys

Department of Solid State Sciences
Chairman: Prof. Dr. Freddy Callens

Faculty of Engineering and Architecture
Academic year 2014-2015

UNIVERSITEIT
GENT

This research was performed as a collaboration between the Center for Molecular Modeling and LumiLab.

Preface

I want to begin this thesis with thanking the people that made this exciting research possible. First of all I want to thank my supervisor Karen Hemelsoet, for giving me the opportunity to work on such an exciting topic at the Center for Molecular Modeling. Secondly I want to thank my co-supervisor Philippe Smet for the infrastructure making experiments possible at LumiLab. I would also like to thank Danny Vanpoucke and Kurt Lejaeghere with whom discussions about the computational aspects always lead to fresh and new ideas. Besides them Jonas Joos also helped me to develop insight in the unknown world of experiments, his insight and library of books made my life much easier.

The monthly meetings with my supervisors and counsellors, where my monthly work was displayed, always helped me in explaining and linking experiment to theory. I want to thank them all for these monthly meetings that helped me focus my mind on the next problem.

This preface would not be complete without mentioning my fellow students, whom I thank for the many lunch breaks waiting in the queue for our sandwiches. In the same way it was comforting knowing that other students doing their thesis at CMM such as my dear friends Sam De Waele, Michiel Gossye and Jelle Wieme were waiting patiently for the job queue to disappear, their companionship made my time at the office wonderful. Last but not least I want to thanks my parents for their support: even though they do not understand what I am working on, they are my greatest supporters.

The author gives permission to make this master dissertation available for consultation and to copy parts of this master dissertation for personal use.
In the case of any other use, the limitations of the copyright have to be respected, in particular with regard to the obligation to state expressly the source when quoting results from this master dissertation.

Arthur De Vos
Gent, May 22, 2015

Combined theoretical-experimental study of chromium doped zinc gallate phosphor

Arthur De Vos

Master's dissertation submitted in partial fulfillment of the requirements for the degree of Master of Science in Engineering Physics
Academic year 2014–2015
Supervisors: Prof. Dr. ir. Karen Hemelsoet, Prof. Dr. Smet Philippe
Counsellors: Dr. Dr. Danny Vanpoucke, Dr. ir. Kurt Lejaeghere, Jonas Joos

Faculty of Engineering and Architecture – University of Ghent
Center for Molecular Modeling and LumiLab

Summary

Persistent luminescent materials form an interesting group of materials with a variety of applications. To date, many questions remain on the precise physical processes responsible for their luminescent behavior. A combination of theory and experiment is often needed to gain a deeper understanding. Herein, we will combine theory (periodic density-functional theory simulations) and experiment to investigate persistent phosphors, chromium doped zinc gallate.

The most stable dopant configuration is determined by introducing a substitutional chromium atom on different atomic sites and examining their electronic, structural and spectroscopic properties. The low concentration of dopants in the host material, used in experiments to create a persistent phosphor, requires the use of a supercell. A supercell however induces band folding, leading to a complicated band structure. In order to make our supercell results more transparent we unfolded the band structures.

Afterwards we introduce different antisite defect configurations in the two most stable doped materials. An antisite defect configuration consists of two initial atoms that are exchanged, zinc and gallium. The stability of these defects is analyzed, as well as the interaction of the chromium states with the antisite defect sites.

In experiment, persistent phosphors are made with different zinc and chromium doping concentration. We investigate them using X-ray diffraction. Internal and external quantum efficiency are derived from measurements for the different samples. The most important analyses of the samples are their excitation and emissions scans that are used to compare with the calculated quantities.

The relation between the density of states and the Tanabe-Sugano diagram is, with input of our density-functional theory calculations, compared with experimentally observed bands. Charge transfer bands are deduced as well. Finally, we attempt to investigate a model for persistent luminescence using our simulations.

Keywords: Spectroscopy, $ZnGa_2O_4$:Cr^{3+}, density-functional theory, experiments

Combined theoretical-experimental study of chromium doped zinc gallate phosphor

Arthur De Vos

Supervisor(s): Prof. Dr. ir.Karen Hemelsoet, Prof. Dr. Philippe Smet

Counsellors: Dr. Dr. Danny Vanpoucke, Dr. ir. Kurt Lejaeghere, Jonas Joos

Abstract—**Persistent phosphors form an interesting group of materials with a variety of applications. To date, many questions remain on the precise physical processes responsible for their particular luminescent behavior and a combination of theory and experiment is suited to gain a deeper understanding. This theoretical study investigates the persistent phosphor, zinc gallate doped with chromium (ZGO:Cr), through periodic density-functional theory simulations. The dopant, Cr^{3+}, inside the inorganic host crystal and their interactions determine the luminescent behavior of this persistent phosphor. The stability of the dopant on different sites is investigated and the electronic structure is calculated. The introduction of an antisite defect, a configuration where two cationic elements of the host material are exchanged, creates an electrical field that is important for the proposed trapping mechanism. The effect of an antisite defect on the spectroscopic and electronic properties is examined together with its stability. The density of states is calculated for these different materials and is used to explain the different interactions between states and the experimentally measured excitation bands.**

Keywords—**Spectroscopy, $ZnGa_2O_4$:Cr^{3+}, density-functional theory, experiments**

I. Introduction

CHROMIUM doped zinc gallate ($ZGO : Cr$) is a persistent phosphor that emits light during a long period when the excitation source is switched off [1]. This long-lasting luminescence, or afterglow, is due to storage of the excitation energy in traps present in the solid host [2], [3], [4], [5]. The long-lasting luminescence makes these materials interesting for application domains such as imaging and emergency lighting. In particular $ZGO : Cr$ is a suited candidate for *in vivo* imaging by its combination of emission and excitation wavelength that can penetrate human tissue without harm [6], [7]. The chromium atom that is the luminescent center in the host material determines these excitation and emission peaks. The filling of traps can be a process where conduction and valence bands play an important role. An important defect with respect to this trapping mechanism is when two atoms of the host material (a gallium and a zinc atom) exchange positions, in $ZGO : Cr$. This is called an antisite defect [8]. These defects create an electrical field, because the atoms in the antisite defect are located at sites expecting an other valence state. This leads to a net charge on the two antisite defects sites. To gain insight into the stability of the emission center and its interaction with the antisite defect configurations in the doped persistent phosphor, a combination of theory and experiment can lead to a better understanding. The introduction of a defect induces small changes that can be quantitatively determined with respect to structural and electronic properties much easier by simulations than by experiments. The combination with experiment will gain insight in how electronic properties are related to experimentally observed quantities.

II. Methods

The host material, zinc gallate (ZGO), was first studied with respect to its band structure. The conventional face-centered cubic cell was used as periodic unit in our simulations. This conventional unit cell consists of 8 zinc, 16 gallium and 32 oxygen atoms, with all atoms of the same kind symmetric equivalent. The low concentration of dopants in the host material, used in experiments to created a persistent phosphor, requires the use of such a supercell (SC). Such a supercell induces band folding, leading to a complicated band structure compared to that of the primitive cell (PC). In order to make it more transparent, we unfolded the band structures with an existing algorithm: BANDUP [9], [10]. The unfolded band structure for host materials was confirmed to be identical to the band structure of the PC.

Afterwards the three different sites corresponding to gallium, zinc and oxygen where subsequently replaced by a chromium atom. The different defect energies of the chromium atom where calculated to determine which dopant site is the most stable. Band structures were again calculated for these different incorporations and were unfolded. In the two most stable doped materials, an antisite defect was introduced. The interaction between the antisite defect and the chromium dopant was studied by means of the density of states.

Experimentally $ZGO : Cr$ samples where made with different dopant concentration staring from the precursors (ZnO, Ga_2O_3 and Cr_2O_3) sintered together at 1400 °C where the temperature is linearly increased during 1 hour and fixed for 4 hours. Their structure is afterwards examined by X-ray diffraction. Quantum internal and external coefficient where measured by using an integrating sphere (152 mm diameter), coated with Spectralon (see [11]) and excita-

tion and emission scans were performed (Edinburgh Instruments FS920).

The excitation wavelength can be deduced from the DFT input and the Tanabe-Sugano diagram [12], [13], [14], [15], [16] making a comparison between the observed and calculated excitation bands possible. All simulations were performed with density-functional theory (DFT) through the software package VASP [17]. We used a PBE functional [18] and a PAW [19], [20] basis set with a cutoff energy of 500eV and k-mesh equal to 282 points$\mathring{A}^3$.

III. Results and Discussions

The chromium is doped on the three different sites replacing a zinc, gallium and oxygen atom. The formation energy is calculated with respect to formation out of the basic materials (ZnO, Ga_2O_3 and Cr_2O_3) indicated by $\triangle F^b$ and out of the pure solids ($\triangle F^p$) (see Table. I). From the formation energies (Table. I) it

	$\triangle F^b$	$\triangle F^p$	E_{Cr}	$E_{Cr_2O_3}$
ZGO	-0.328	-12.358	N.A.	N.A.
$ZGO : Cr^{3+}_{Ga}$	-0.316	-12.389	-0.248	0.096
$ZGO : Cr^{3+}_{Zn}$	0.106	-12.182	1.408	3.463
$ZGO : Cr^{3+}_{O}$	1.385	-11.260	8.780	13.704

TABLE I: Formation energy for one $ZGO : Cr$ chemical unit (7 atoms) and defect energy for one defect introduced in the SC. All energies are given in eV.

is confirmed that chromium doped on the gallium site is the most stable doped material. The difference between the two types of formation energy is caused by the stability of the starting materials. When starting from the basic materials the undoped host material is the most stable, when starting from the pure solid materials the $ZGO : Cr_{Ga}$ is most stable. This is also seen in the defect energies. E_{Cr} is the energy stability of a chromium defect relative to chromium clustering around it. As chromium clustering is related to pure chromium metal it follows the trend where chromium doped on the gallium site is the most stable. As one looks at clustering relative to Cr_2O_3, $E_{Cr_2O_3}$, the reference is related to the basic material and indeed only positive defect energies are observed related to the fact that the formation energy of the host materials is the smallest when related to basic starting materials. With respect to formation energy, the doping on a zinc site is only slightly less stable than the doping on a gallium site. However when we look at the different dopant energies it is seen that a chromium atom located on a zinc site is much less stable than on a gallium site. We conclude that from simulation the chromium doped on the gallium site is the most probable.

With respect to the electronic properties of the persistent phosphor the density of states was calculated for the doped materials and compared to the host material (see Fig. 1). In the density of

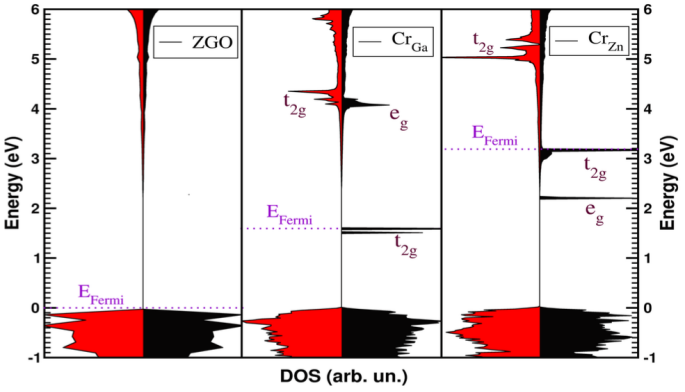

Fig. 1: The density of state of ZGO (left), $ZGO : Cr_{Ga}$ (middle) and $ZGO : Cr_{Zn}$ (right)

states it can be seen that the splitting of the levels, introduced by a Kohn-Sham potential, are those of a d^1 configurations located in tetrahedral or octahedral surrounding. This is indicated by the irreducible representations e_g and t_{2g} in Fig. 1.

After the host material is doped, we introduce antisite defect configurations. To model a lower concentration of antisite defects only the ionic positions are optimized while keeping the volume fixed. The different antisite defect configurations are labeled according to Fig. 2. Different defect energies are studied for the

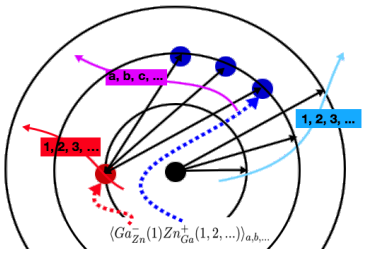

Fig. 2: Classification of different antisite defect configurations. When a chromium atom is doped on zinc site the meaning of the first to numbers are reversed.

combination of an antisite defect and dopant. These defect energies are respectively $E_{Anti-Cr}$ indicating the stability of the antisite defect with respect to chromium doped ZGO, $E_{Cr-Anti}$ related to the stability of chromium and E_{Anti} the stability of anti defect site. The relation between these different defect energies is schematically shown in Fig. 3. The stability of the different antisite defects in $ZGO : Cr_{Ga}$ and $ZGO : Cr_{Zn}$ are shown in Fig. 4 and 5 . The two figures show that the defect energies ($E_{Anti-Cr}$ and $E_{Cr-Anti}$) can be explained by charge compensation. As introducing an antisite defect causes a charge on the misplaced atom it causes instability. This charge can be compensated by placing another defect which carries an opposite charge close

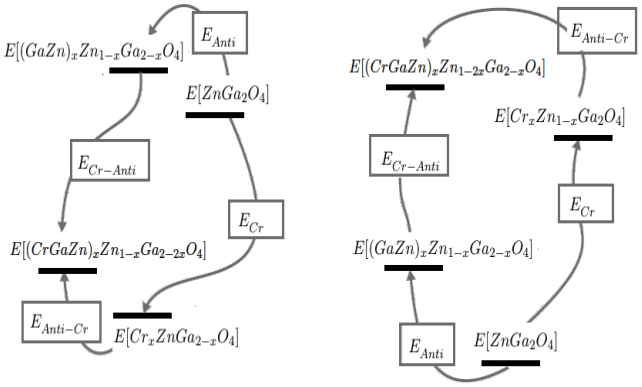

(a) Cr_{Ga} (b) Cr_{Zn}

Fig. 3: Different definitions of defect energies with their relative order.

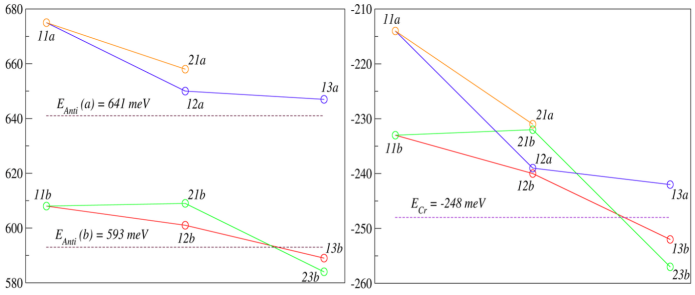

(a) $E_{Anti-Cr}(meV)$ (b) $E_{Cr-Anti}(meV)$

Fig. 4: Comparing of $E_{Anti-Cr}$ with $E_{Cr-Anti}$ for different antisite defect configurations in the doped chromium ZGO on a gallium site.

to it. In our case, the charged defects are Cr^+_{Zn}, Ga^+_{Zn} and Zn^-_{Ga}. From the figures we learn that for in $ZGO : Cr_{Ga}$ both antisite defect sites want to sit as close as possible to each other, while being as far away from the chromium atom. When chromium is doped on the zinc site also the chromium atom is charged (Cr^+_{Zn}) and can compensate charge on the antisite defect sites. We now observe that the negative antisite defect site (Zn^-_{Ga}) is located close to the chromium atom to compensate its charge while the other antisite defect site wants to be as far as possible from both. The antisite defect energy E_{Anti} is not displayed because it is observed that its value is only dependent on the distance between the two antisite defect sites. From Fig. 4 (b) and 5 (b) we conclude that the stability, for the most stable antisite defect configuration, $ZGO : Cr_{Ga}$, remains almost constant while the instability of the chromium dopant is reduced.

The interaction between the chromium levels (t_{2g} and e_g) and the antisite defect sites was analyzed through the densities of states. It is observed that Zn^-_{Ga} creates four band gap states in

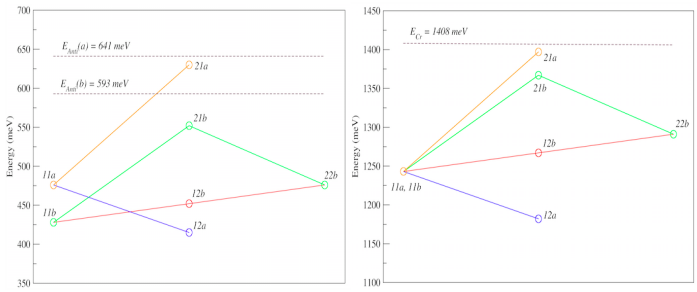

(a) $E_{Anti-Cr}(meV)$ (b) $E_{Cr-Anti}(meV)$

Fig. 5: Comparing of $E_{Anti-Cr}$ with $E_{Cr-Anti}$ for different anti defect configuration in the chromium doped ZGO on a zinc site.

contrast to the Ga^+_{Zn}. These band gap states have room four 4 electrons. The interaction between the Cr_{Ga} states an the antisite defect sites is only observed when Zn^-_{Ga} is located close to the chromium state ($\cong 3\mathring{A}$). This interaction causes extra splitting of the chromium states resulting in non-degenerate states. When the Zn^-_{Ga} antisite defect site is placed further no additional splitting, interaction with the chromium atom, is observed. The band gap states are composed of 2 two-particles states and when the two antisite defect are close to each other they further split in 4 one-particle states.

The interaction between Cr^+_{Zn} and the antisite defect sites can be understood by realizing that the chromium atom behaves as a Ga^+_{Zn} antisite defect site. By putting a Zn^-_{Ga} close to the chromium atom extra splitting is observed. When the antisite defect site Ga^+_{Zn} is located close and the Zn^-_{Ga} are put further from the chromium atom the splitting of chromium states is reduced and becomes equal to the doped material (Cr^+_{Zn}) with the addition of the band gap state. This interaction suggests that the most interesting defect for electronic and spectroscopic properties is induced by the presence of the Zn^-_{Ga} antisite defect site. The interaction between the two antisite defect sites is again only dependent on the distance between both. However, in contrast to chromium doped on the gallium site, the chromium induces an equivalent Ga^+_{Zn} antisite defect site and the distance between the "2" antisite defects, Ga^+_{Zn} and Cr^+_{Zn}, configurations should be taken to see if splitting of the 2 two-particles bad gap states to 4 one-particle states occurs.

The differently doped material were made by sintering the grinded basic materials (ZnO, Ga_2O_3 and Cr_2O_3) in a crucible that was put in a furnace. The structure of the doped materials was analyzed using X-ray diffraction confirming the formation of doped ZGO. In experiments the excitation scan revealed three excitation bands resembling the excitation scans given in literature [2]. Also the emission scans nicely resembled existing literature data. The quantum efficiency of the doped materials was measured and at high doping levels no emission was observed (see Table. II and

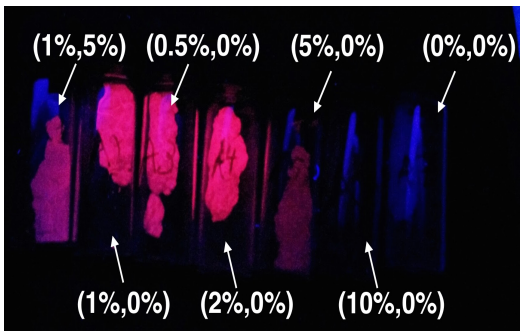

Fig. 6: Luminescence of the synthesized materials upon UV irradiation labeled with there their introduced notation.

Fig. 6) The Tanabe-Sugano diagram that displays the different energy levels as a function of the crystal field was used to determine the values of three excitation wavelengths (see Fig. 7 [16]) where DFT calculations provided the crystal field strength. This comparison was done solely for $ZGO : Cr_{Ga}$ as this is the experimentally observed one. An inset is also given displaying a measured excitation scan. An extra excitation band can be calculated by considering an excitation from the valence band to the first unoccupied chromium state. This charge transfer band is expected to coincide with the excitation band of smallest wavelength. A total of 4 excitation bands are obtained which are compared with experiments in Table. III.

	(1%,5%)	(1%,0%)	(0.5%,0%)	(2%,0%)	(5%,0%)
QEi	0.54	0.78	0.58	0.58	0.053
QEe	0.18	0.21	0.17	0.27	0.030

TABLE II: Internal QEi and external QEe quantum efficiency of $ZGO : Cr^{3+}$ for different (x%,y%) samples where x% indicates the doping of chromium and y% indicates the excess of zinc atoms.

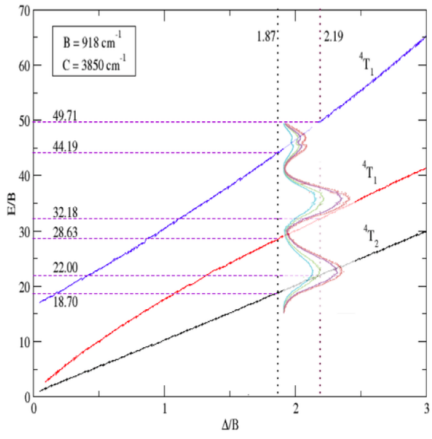

Fig. 7: Partial Tanabe-Sugano diagram where the different excitation bands are deduced from the crystal field strength determined by DFT.

	$\lambda_1(nm)$	$\lambda_2(nm)$	$\lambda_3(nm)$	$\lambda_{CT}(nm)$
Theory	583-495	380-339	246-219	317-300
Exp	575-525	425-375	325-275	

TABLE III: The comparison between experimentally observed bands and the theoretically calculated bands.

Lastly a proposed model of persistent model was examined where a lowering of the conduction band is assumed by the presence of the electric field created by the antisite defect around the dopant [8]. This lowering causes an easy charge separation even for excitation wavelength in the near infrared. A small lowering of the conduction band was indeed seen in the density of states. It was also observed that the only important antisite defect site Zn_{Ga}^{-} affects the conduction band when located close to the chromium atom. However a bigger SC should be used to introduce more antisite defect configurations to further test this observation.

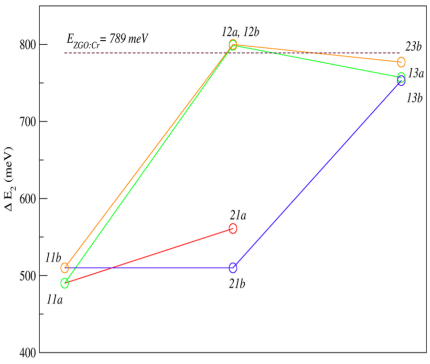

Fig. 8: The energy difference between the t_{2g} level and the conduction band for the different antisite defect configurations.

IV. Conclusion

In considering the different doping configurations of chromium in ZGO it was confirmed that, just as in experiment, the chromium is most stable when it is located on a gallium site. The instability with respect to the formation energy of chromium on a zinc site compared to chromium doped on a gallium site, makes it possible for the former to exist theoretically. However when considering the defect energy, which displays the instability of the dopant, a clear instability of doping on a zinc site is observed. It was observed that the local charge instability of antisite defect sites determines which configuration is most stable.

The interaction of the antisite defects with the chromium states is determined from the negatively charged defect Zn_{Ga}^{-} and not from the other defect site. When this interacting defect was taken

far from the chromium atom, the chromium states where similar to the states where no antisite defect was present. Also band gap states of the Zn_{Ga}^{-} where observed. The other defect site, Ga_{Zn}^{+}, does not creates band gap states. These band gap states correspond to 2 two-particle states when the Zn_{Ga}^{-} is located far from a Ga_{Zn}^{+} and when chromium is doped on a zinc site the Zn_{Ga}^{-} should also be far from this chromium atom. If this is not the case the band gap states split in 4 one-particle states.

When the antisite defect is introduced in a $ZGO : Cr_{Ga}$ it is observed that the two antisite defects want to be as far as possible from the chromium atom and as close as possible to each other. This most stable configuration is in correspondence with charge compensation. As no charge is created at the chromium no charge compensation by one of the two antisite defect sites is necessary and only the charge in the two antisite defect sites should compensate each other.

When the chromium atom is doped on the zinc site a positive charge is introduced. In correspondence with charge compensation the most stable configuration is now when the negative antisite defect site Zn_{Ga}^{-} is located close to the chromium atom. This leads to a positively charged Cr_{Zn}^{+} and the supplementary positive charge of the other defect site should be as far as possible. .

In the optical spectroscopy experiments the excitation bands are explained using the Tanabe-Sugano diagram. From the DFT calculations, the splitting of the chromium states can be extracted and is a good approximation of the crystal field strength used in the Tanabe-Sugano diagram where the excitation bands can be determined. An extra charge transfer band was obtained that can not be determined from the Tanabe-Sugano diagram. The calculated excitation bands were in good agreement with experimental results.

Finally a model which assumes a lowering of the conduction band relative to the chromium t_{2g} states was compared with the evolution of the conduction band for different antisite defect configurations. In experiments, the theory assumes the conduction band to lower compared to the chromium states by the presence of the electrical field induced by the antisite defect around the chromium atom. This lowering could be observed. However, more antisite defect configuration should be considered to confirm this model and will be tested in further research.

ACKNOWLEDGEMENT

The computational resources (Stevin Supercomputer Infrastructure) and services used in this work were provided by the VSC (Flemish Supercomputer Center), funded by Ghent University, the Hercules Foundation and the Flemish Government - department EWI. The author would also like to thank both the CMM and LumiLab research groups for the opportunity to perform this research as well as their knowledge and guidance.

REFERENCES

[1] J. Hölsä, "Persistent Luminescence Beats the Afterglow - 400 Hundred Years of Persistent Luminescence," *Electrochemical Society Interface, The 18(2009)4,42-45*.

[2] S. K. Sharma, A. Bessière, N. Basavaraju, K. R. Priolkar, L. Binet, B. Viana, and D. Gourier, "Interplay between chromium content and lattice disorder on persistent luminescence of $ZnGa_2O_4 : Cr^{3+}$ for in vivo imaging," *Journal of Luminescence*, vol. 155, pp. 251–256, Nov. 2014.

[3] S. Sharma, D. Gourier, B. Viana, T. Maldiney, E. Teston, D. Scherman, and C. Richard, "Persistent luminescence of $AB_2O_4 : Cr^{3+}$ (A=Zn, Mg, B=Ga, Al) spinels: New biomarkers for in vivo imaging," *Optical Materials*, vol. 36, pp. 1901–1906, Sept. 2014.

[4] A. Bessière, S. K. Sharma, N. Basavaraju, K. R. Priolkar, L. Binet, B. Viana, A. J. J. Bos, T. Maldiney, C. Richard, D. Scherman, and D. Gourier, "Storage of Visible Light for Long-Lasting Phosphorescence in Chromium-Doped Zinc Gallate," *Chemistry of Materials*, vol. 26, pp. 1365–1373, Feb. 2014.

[5] N. Basavaraju, K. R. Priolkar, D. Gourier, S. K. Sharma, A. Bessière, and B. Viana, "The importance of inversion disorder in the visible light induced persistent luminescence in Cr^{3+} doped AB_2O_4 (A = Zn or Mg and B = Ga or Al)," *Phys. Chem. Chem. Phys.*, vol. 17, no. 3, pp. 1790–1799, 2015.

[6] T. Maldiney, A. Bessière, J. Seguin, E. Teston, S. K. Sharma, B. Viana, A. J. J. Bos, P. Dorenbos, M. Bessodes, D. Gourier, D. Scherman, and C. Richard, "The in vivo activation of persistent nanophosphors for optical imaging of vascularization, tumours and grafted cells," *Nat Mater*, vol. 13, pp. 418–426, Apr. 2014.

[7] H. F. Brito, J. Hölsä, T. Laamanen, M. Lastusaari, M. Malkamäki, and L. C. V. Rodrigues, "Persistent luminescence mechanisms: human imagination at work," *Optical Materials Express*, vol. 2, pp. 371–381, Apr. 2012.

[8] D. Gourier, A. Bessière, S. Sharma, L. Binet, B. Viana, N. Basavaraju, and K. R. Priolkar, "Origin of the visible light induced persistent luminescence of Cr^{3+}-doped zinc gallate," *Journal of Physics and Chemistry of Solids*, vol. 75, pp. 826–837, July 2014.

[9] P. V. C. Medeiros, S. Stafström, and J. Björk, "Effects of extrinsic and intrinsic perturbations on the electronic structure of graphene: Retaining an effective primitive cell band structure by band unfolding," *Physical Review B*, vol. 89, Jan. 2014.

[10] P. V. Medeiros, S. S. Tsirkin, S. Stafström, and J. Björk, "Unfolding spinor wavefunctions and expectation values of general operators: Introducing the unfolding-density operator," *arXiv preprint arXiv:1409.5343*, 2014.

[11] S. Leyre, E. Coutino-Gonzalez, J. Joos, J. Ryckaert, Y. Meuret, D. Poelman, P. Smet, G. Durinck, J. Hofkens, G. Deconinck, and P. Hanselaer, "Absolute determination of photoluminescence quantum efficiency using an integrating sphere setup," *Review of Scientific Instruments*, vol. 85, no. 12, p. 9, 2014.

[12] G. Racah, "Theory of complex spectra. ii," *Phys. Rev.*, vol. 62, pp. 438–462, Nov 1942.

[13] G. Racah, "Theory of complex spectra. i," *Phys. Rev.*, vol. 61, pp. 186–197, Feb 1942.

[14] Y. Tanabe and S. Sugano, "On the absorption spectra of complex ions, iii the calculation of the crystalline field strength," *Journal of the Physical Society of Japan*, vol. 11, no. 8, pp. 864–877, 1956.

[15] Y. Tanabe and S. Sugano, "On the absorption spectra of complex ions. i," *Journal of the Physical Society of Japan*, vol. 9, no. 5, pp. 753–766, 1954.

[16] Y. Tanabe and S. Sugano, "On the absorption spectra of complex ions ii," *Journal of the Physical Society of Japan*, vol. 9, no. 5, pp. 766–779, 1954.

[17] J. Hafner, "Ab-initio simulations of materials using VASP: Density-functional theory and beyond," *Journal of Computational Chemistry*, vol. 29, pp. 2044–2078, Oct. 2008.

[18] J. P. Perdew, K. Burke, and M. Ernzerhof, "Generalized gradient approximation made simple," *Phys. Rev. Lett.*, vol. 77, pp. 3865–3868, Oct 1996.

[19] P. E. Blöchl, "Projector augmented-wave method," *Phys. Rev. B*, vol. 50, pp. 17953–17979, Dec 1994.

[20] G. Kresse and D. Joubert, "From ultrasoft pseudopotentials to the projector augmented-wave method," *Phys. Rev. B*, vol. 59, pp. 1758–1775, Jan 1999.

Contents

Abbreviations

ZGO	Zinc gallate
DFT	Density functional theory
SDFT	Spin density functional theory
LDA	Local density approximation
GGA	Generalized gradient approximation
PBE	Perdew, Burke and Ernzerhof
KS	Kohn-Sham
PP	Pseudopotential
PAW	Projected-Augmented wave
VASP	The Vienna Ab-Initio Simulation Package
1BZ	First Brillouin zone
IBZ	Irreducible Brillouin zone
DOS	Density of states
LDOS	Local Density of states
PC	Primitive cell
SC	Supercell
LCAO	Linear combination of atomic orbitals
HSE	Heyd-Scuseria-Ernzerhof
QSGW	Quasiparticle Self-consistent GW
FCC	Face-centered cubic
BCC	Body-centered cubic
XRD	X-ray diffraction
QE	Quantum efficiency
VB	Valence band
CB	Conduction band
(A)S-PSB	(Anti) Stokes phonon side bands
AS-PSB	Anti Stokes phonon side bands

Symbols

$n_0(\overline{r})$	Ground state density
Ψ_0	Ground state wavefunction
$T_s[n]$	Kinetic energy of the Kohn-Sham orbitals
$E_{xc}[n]$	Exchange-correlation functional
$E_H[n]$	Hartree energy
$V[n]$	External potential
$v_{eff}(\overline{r})$	Effective potential for the Kohn-Sham orbitals
$v_H(\overline{r})$	Hartree potential
$v_{xc}(\overline{r})$	Exchange-correlation potential
ϵ_j	Kohn-Sham eigenvalues
$\overline{T}$	Real lattice vector
$\overline{G}$	Reciprocal lattice vector
$\Psi_{\overline{k},n}(\overline{r})$	Single-particle Bloch-like orbital characterized by $\overline{k}, n$
$D(E)$	Density of states
$D_{\alpha,\mu}(E)$	Local density of states
I_k	"Ionization" energy for a system where the k^{th} Kohn-Sham orbital is unoccupied
V_p	Volume of the primitive cell
V	Volume of the total crystal
$E_g^{integer}$	Band gap from an energy difference
E_g^{deriv}	Band gap from energy derivatives
E_{Fermi}	Fermi energy
I	Ionization energy
A	Electron affinity
$\Sigma(\overline{r}, \overline{r'}, E_i)$	Self energy
E_{Cutoff}	Cut-off energy

$\overline{R}_m$	Position of nucleus m
Z_m	The atomic number of the nucleus m located at $\overline{R}_m$
$\overline{r}_i$	Position of the electron i
$\triangle F^p$	Formation energy from the pure materials
$\triangle F^b$	Formation energy from the basic materials
E_{Cr}	Defect energy of a chromium relative to chromium clustering
$E_{Cr_2O_3}$	Defect energy of a chromium atom relative to chromium oxide clustering
$E_{Anti-Cr}$	Defect energy of a chromium + antisite defect relative to chromium without anti defect
$E_{Cr-Anti}$	Defect energy of a chromium + antisite defect relative to clustering of chromium atoms around the anti defect
E_{Anti}	Defect energy of an anti defect
F	Structure parameter
d_{hkl}	Distance between two closest planes with (hkl) Miller indeces
QEi	Internal quantum efficiency
N_{em}	Number of emitted photons
N_{abs}	Number of absorbed photons
QEe	External quantum efficiency
N_{in}	Number of incident photons
V_{O_h}	Perturbation potential caused by an octahedral surrounding
V_{T_d}	Pertubation potential caused by an tetrahedral surrounding
θ_D	Debye temperature
$\triangle E_{mol}$	Energy difference per atom between the crystalline material and its gas-like molecules.
$\alpha_{V,rt}$	The temperature-dependent volume expansion coefficient at room temperature
B_0	The bulk modulus
B_1	Derivative of the bulk modulus with respect to pressure
B_2	Second-order derivative of the bulk modulus with respect to pressure
$\triangle V^{(1)}$	Thermal volume expansion correction
$\triangle V^{(2)}$	The zero-point volume shift
$\triangle B^{(1)}$	Thermal bulk modulus expansion correction
$\triangle B^{(2)}$	The zero-point correction on the bulk modulus

Chapter 1

Introduction

Photoluminescence is light emission from any form of matter after the absorption of photons. Persistent luminescence is a specific type of photoluminescence in which the emission can last for hours or days after the irradiation source has been switched off [1, 2, 3]. This long-lasting luminescence, or afterglow, is due to storage of the excitation energy by traps present in the solid host [4, 5, 6].

This thesis focuses on a persistent phosphor with as host material zinc gallate ($ZnGa_2O_4$ denoted as ZGO) doped with chromium ions ($ZGO : Cr^{3+}$). Understanding the optical behavior of this persistent phosphor is a challenging task, which is most ideally tackled using a combined theoretical-experimental approach.

The influence of defect sites in the persistent phosphor is closely examined by using simulations, as in experiments it is much more difficult to attribute a given defect to a specific feature of the material.

Firstly the host material will be studied. Next a chromium atom will be introduced as a dopant in the this defect-free host material. Different configurations site of the chromium atom will be looked at to see which configuration is the most stable. In addition, the inclusion of dopants induces additional energy levels in the band structure of the host material. Knowledge of their exact position is crucial as several models for persistent luminescence involve interactions between the excited states, the dopant ion and the conduction band (CB) levels.

We therefore take a closer look at the band structure of the persistent luminescent where the chromium atom is doped on different sites.

Persistent luminescence is also closely related with defects present in the material. Experimentally it is not so easy to study these different defects and simulations allow us to look at the probability of the presence of certain defects. The combined approach of simulations and experiments is thereby fundamental in obtaining a better picture of the spectroscopic and electronic properties of the persistent luminescent material.

1.1 Application of persistent luminescence

Persistent luminescent materials have a variety of applications and are traditionally used in security and traffic signs, dials, displays, toys and gadgets. Recently, also their use as markers for *in vivo* imaging is explored [7]. The persistent phosphor $ZGO : Cr^{3+}$ is an ideal candidate

for *in vivo* imaging because of its interesting spectroscopic properties. This section focuses on this intriguing application used for medical imaging.

Tumors are very chaotic vascular system and nanoparticles particles can be trapped in them [8]. By examining the luminescence of a substance that is injected into the patient, one can produce an image and chart these chaotic vascular systems. The luminescence of the injected substance has to go through the patient's skin and has to be able to emit during a long period. Many medical procedures nowadays use radioactive substances that are harmful for living tissue [9]. The persistent phosphor $ZGO : Cr^{3+}$ is an alternative for this, having a long period of luminescence and causing almost no harm to living tissue, which makes it an attractive alternative. ‘

The reason $ZGO : Cr^{3+}$ can be used for imaging is because it emits mostly in the infrared (IR) and near infrared (NIR) region (see Fig. 1.1). This light, emitted by our persistent phosphor, can penetrate living tissue without harm.

An extra advantage is that $ZGO : Cr^{3+}$ can efficiently be excited with NIR light [10]. At these wavelengths, the penetration depth in human tissue is large enough to excite the persistent phosphor inside the body, making it possible to re-excite the particles when brought into the patient.

The most efficient wavelength for exciting the particles is in the ultraviolet (UV) region. UV light is however harmful for living tissue, making this excitation wavelength only useful for exciting the substance outside the patient. The persistent luminescence is therefore of importance because even without re-exciting them we can follow the particles during a long time (see Fig. 1.1).

1.2 Crystallographic and optical properties of $ZGO : Cr^{3+}$

Crystallographically the host material, ZGO, belongs to the spinel structures, similar to the spinel $MgAl_2O_4$. In these AB_2O_4 compounds, A is typically a divalent ion (Zn, Mg, Ca, Sr), while B is trivalent (Al, Ga, Cr).

A spinel structure consist of 2x2x2 face-centered cubic (FCC) unit cells formed by oxygen atoms accompanied by A^{2+} and B^{3+}. In one FCC cell there are 8 tetrahedral and 4 octahedral voids. The total spinel structure thereby consist of 32 tetrahedral and 64 octahedral voids. In the normal spinel noted as AB_2O_4 (8 chemical units in one spinel structure) the A^{2+} occupies 1/8 of the tetrahedral voids and the B^{3+} occupies 1/2 of the tetrahedral voids. This site occupation can however be changed, depending on the composition, resulting in a mixed or inverse spinel. In an inverse spinel noted as $B(AB)O_4$, half of the B^{3+} occupy tetrahedral accompanied by the A^{2+}. The other half of B^{3+} occupy octahedral voids. Consequently, occupational disorder is often naturally present in these compounds, playing a crucial role in $ZGO : Cr^{3+}$ persistent luminescent behavior [6]. It has been shown by experiment [11] and theory [12] that for ZGO, the normal spinel is more stable than the inverse spinel structure.

Careful Electron Paramagnetic Resonance (EPR) spectroscopy and photoluminescence measurements revealed that the luminescence results from excitation of specific Cr^{3+} ions having an antisite defect site as first cationic neighbor [4, 13]. In addition, other structural defects (such as oxygen vacancies, interstitials or cation vacancies) have been suspected in other persistent

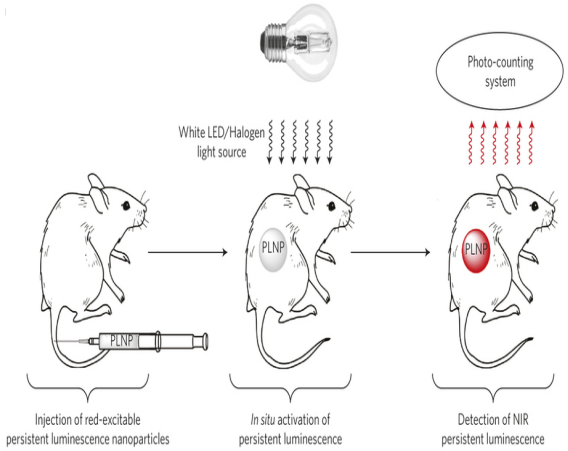

(a)

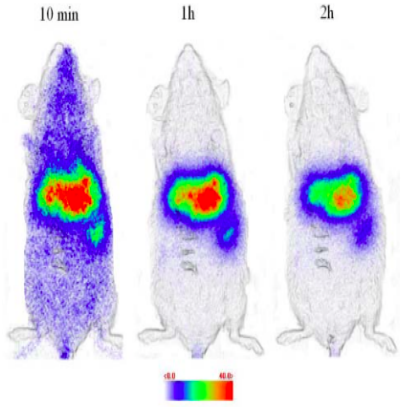

(b)

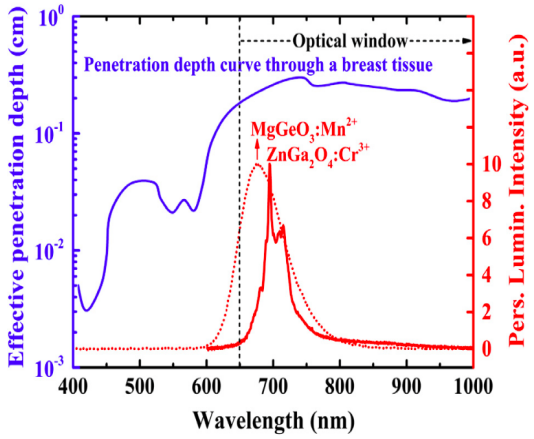

(c)

Figure 1.1: *In vivo* application of the persistent phosphor $ZGO : Cr^{3+}$ (Fig. taken from [7]). In (a) the substance is excited before injection inside the mouse. In (b) the short and long term distribution of the nanoparticles is shown by imaging with the emitted light. Finally (c) shows the penetration depth of light, mostly infrared, in the human tissue accompanied by the emission spectrum of $ZGO : Cr^{3+}$ and magnesium germanium oxide ($MgGe_2O_3$) doped with manganese ($MGO : Mn^{2+}$), where the emission of these two persistent phosphors is ideally located.

phosphors to play an essential role in the trapping process. Identifying the nature of the responsible defects by analytical techniques is often cumbersome. Theoretical and computational input is therefore needed to build a correct defect model.

1.3 Mechanism of persistent luminescence

The reason persistent phosphors emit such a long time when the excitation source is shut off is due to capture of excitation energy in traps [10, 14, 15, 5, 16]. These traps store excitation energy in the persistent phosphor and release it due to thermal fluctuation. Multiple trapping mechanisms and the stored energy jumps from one trap to another due to the thermal fluctuation

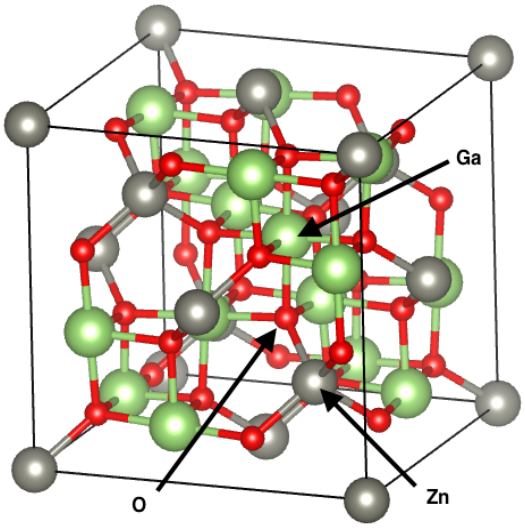

Figure 1.2: Spinel structure of $ZnGa_2O_4$

lead to long afterglow when the excitation source is been shut off.

1.4 Persistent luminescent of $ZGO : Cr^{3+}$

The storage of the energy in defects in $ZGO : Cr^{3+}$ is caused by an antisite defect site in the vicinity of the doped chromium atom on a gallium site [17, 18] (cf. Fig. 1.3). This model is well developed and generally accepted.

An antisite defect is a defect where two atoms of the host material are exchanged: a gallium atoms and a zinc atom. These two sites are noted as Zn_{Ga}^{-} for a zinc atom on a gallium site and Ga_{Zn}^{+} for a gallium atom on a zinc site. The plus and minus indicate the charge of such a defect. The Zn_{Ga} site becomes negative as the Zn^{2+} is located on a +III position and for the Ga_{Zn} site it is the other way around. If an antisite defect surrounds a chromium atom it creates a local electrical field inducing charge separation.

With charge separation we mean that when exciting a chromium atom an electron-hole pair is created that, because of the local electric field from the antisite defect site, will separate and stored in the two oppositely charged antisite defect sites. This energy can subsequently be released by thermal fluctuation, but this process is slow and is the reason of the long lasting character of the emission [5, 4]. In optical spectroscopy experiments labels are assigned to each of the subsequent states of Fig. 1.3. These labels represent symmetry states and different symmetry states represent different energies.

1.5 Aim

Combining theory and experiment may result in the rational design of luminescent materials with improved functionalities, in which the materials are first modeled before they are synthesized and tested. However, many challenges still need to be overcome before this is possible. This master thesis points out some of the main challenges, and where possible, solutions are sought to increase the accuracy and reliability of the simulations and bring theoretical and experimental

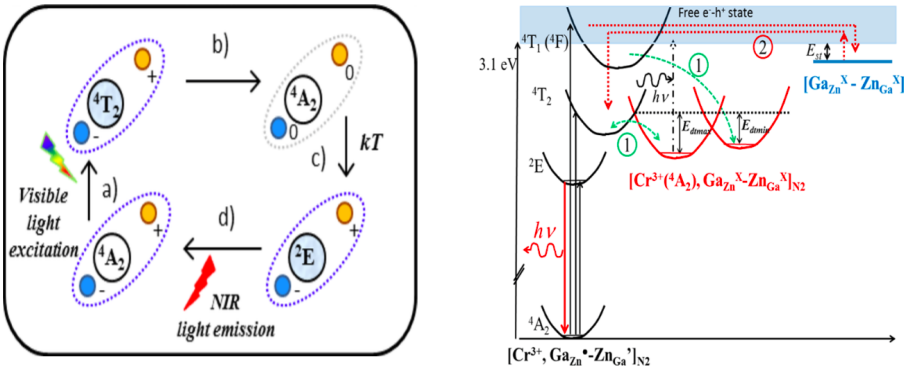

(a) (b)

Figure 1.3: In (a) the process of how the excitation energy of a chromium atom surrounded by an antisite defect site is trapped. The stored energy in the neutralized antisite defect sites is transferred back to the chromium atom due to thermal fluctuations (Fig. taken from [4]). Subsequently the chromium atom emits this energy. At (b) we see the different energy levels of the chromium atom and their place in the band gap. The black levels correspond to energy levels of chromium without antisite defect site in its neighborhood in contrast to the red lines.

results closer together.

A first objective of this thesis is to construct reliable energy diagrams of the solid hosts and obtain a clear understanding of their band structure. In addition to the parent materials, the chromium-doped host is also investigated with respect to the dopant stability and band structure.

A second objective is to examine to what extent defects affect the electronic properties of the doped material. Here, besides the dopant, an antisite defect is introduced. Different antisite defect configurations exist in $ZGO : Cr^{3+}$ and by examining their stability, predictions on how an antisite defect site surrounds the chromium dopant should be possible. These defects also change the band structure of the persistent phosphor. Because the interaction between states of the dopant and the antisite defect can be studied more easily in simulations than in experiments a closer look will be taken at this as well.

A third objective is to combine the theoretical and experimental results in order to obtain a better insight in the subtle interplay between all factors at work in $ZGO : Cr^{3+}$. A key part in the comparison between simulations and experiments is by use of group theory. In optical spectroscopy measurements qualitative information is deduced from symmetry groups and quantitative by the measurements. In this way we want to combine both symmetry group theory and the simulation where the simulations know lead to quantitative information.

1.6 Methodology

Given that the $ZGO : Cr^{3+}$ is experimentally well-studied and characterized, the main focus of this thesis lies on improving the theoretical approach for studying such complex materials and on the careful combination of the theoretical and experimental data. The experimental part of this thesis focuses on synthesizing the material and confirming the desired material has been formed.

Some elementary quantities corresponding to the internal and external quantum efficiency will be measured. Excitation and emission scans will be compared to other experimental results and afterwards used to compare with the quantities obtained from the simulations. All simulations are performed using the Vienna Ab-Initio Simulation Package (VASP)([19]). It is a periodic implementation of density functional theory (DFT) (see section 2.1). The level of theory used for the exchange-correlation term is the 1996 GGA functional of Perdew, Burke and Ernzerhof (PBE) [20]. A key part in the simulation is understanding what quantities are calculated and in what way they are connected with measurable spectroscopic quantities. A strong theoretical basis is therefore important. The theoretical basis will be explained in Chapters 2 and 3. The band structure, which is a key output of the simulations will also be examined and defects will be introduced in the doped material. A supercell (SC) of the host material (ZGO) is required to add a small number of dopants necessary to be compatible with the experimental doping. The SC for the host material is the conventional cell of the face-centered host material and contains 8 zinc, 16 gallium and 32 oxygen atoms. The defects that are introduced in this SC will consist of the interesting antisite defect configurations surrounding the chromium doped ZGO. The stability of these defect configurations will be examined. Also the defect introduces band gap states and the interaction between the different single-particle states as displayed in the density of states will be examined.

Chapter 2

Solving the many body-problem

The band structure and the density of states (DOS) are important ingredients to understand the luminescent behavior of a material. The absorption and emission wavelengths correspond to energy differences between states. How many states are accessible is reflected in the DOS. The interaction of states cannot be seen in the DOS but is shown in the band structure. The most interesting interactions are that of an emitting center with itself and with the conduction and/or valency band. These interactions are more difficult to measure in experiments and contain information that can be fundamental in explaining the luminescent behavior of a material.

In this chapter we want to explain the theories that are needed to obtain these quantities from simulations. In the next chapter we then discuss what a band structure actually represents and what relevant properties can be extracted from it.

2.1 Density Functional Theory (DFT)

The interaction between electrons and nuclei in a solid is a many-body problem, which will be investigated quantum mechanically, via solvation of the following equation:

$$\left[-\frac{1}{2}\sum_i \nabla_i^2 - \sum_{im} \frac{Z_m}{|\overline{r}_i - \overline{R}_m|} + \frac{1}{2}\sum_{i\neq j} \frac{1}{|\overline{r}_i - \overline{r}_j|} \right] \Psi(\overline{r}_i, \overline{R}_m) = E\Psi(\overline{r}_i, \overline{R}_m) \tag{2.1}$$

where Z_m is the atomic number of the nucleus m located at $\overline{R}_m$. The position of the electrons is indicated by $\overline{r}_i$ and the summation is over all electrons of the system.

Nevertheless, solving the many-body problem via conventional quantum mechanics – that is, by trying to find the wavefunction satisfying the Schrödinger equation (2.1) – you are bound to hit an exponential wall. With exponential wall we mean that the number of variables to describe the wavefunction to a certain precision will increase exponentially with the number of particles making the problem hard or even impossible to solve. We conclude that trying to find the wavefunction is not a good approach if you are dealing with many interacting particles.

Here density functional theory (DFT) comes in [21]. DFT provides a simpler way to solve the many-body problem. It exploits the fact that the ground-state density

$$n_0(\overline{r}) = N \int ... \int \Psi_0^*(\overline{r}, \overline{r}_2, ..., \overline{r}_N)\Psi_0(\overline{r}, \overline{r}_2, ..., \overline{r}_N) d\overline{r}_2 ... d\overline{r}_N \tag{2.2}$$

contains as much information as the ground-state wavefunction $\Psi(r_1, r_2, ..., r_N)$. The density is a function of only three spatial variables, which in comparison to the ground-state wavefunction, does not become more complex when increasing the particle number N. The exponential wall is thus avoided.

The bijection between ground-state wavefunction and density is possible because the ground-state wavefunction does not only lead to the ground-state density but also has to minimize the total energy (Rayleigh-Ritz minimal principle):

$$E_0 = min_\Psi(\Psi \widehat{H} \Psi). \tag{2.3}$$

These two conditions are enough to uniquely characterize the ground-state many-body wavefunction as a functional of the ground-state density, as formulated by the Hohenberg-Kohn theorems [22]. Because the ground-state density defines the wavefunction, it also specifies the external potential[1]. The external potential is the potential that is exercised by the nuclei on the electrons and it is called external because it is dependent on the positions of the nuclei and not of the electrons themselves. As the wavefunction is a functional of the ground-state density, all observables in the ground-state are also functionals of the ground-state density

$$\Psi_0(\overline{r}_1, \overline{r}_2, ..., \overline{r}_N) = \Psi_0[n_0(\overline{r})] \tag{2.4}$$

$$O[n_0] = \langle \Psi_0[n_0] | \widehat{O} | \Psi_0[n_0] \rangle. \tag{2.5}$$

DFT is typically applied by writing the energy as a functional of the density:

$$E_0 = E[n_0] = \langle \Psi_0[n_0] | \widehat{T} + \widehat{U} + \widehat{V} | \Psi_0[n_0] \rangle \tag{2.6}$$

and by minimizing this expression. In equation (2.6), $\widehat{U}$ is the coulombic repulsion of electrons, $\widehat{T}$ is the kinetic energy and $\widehat{V}$ the external potential.

We have proven that every quantity is a functional of the ground-state density. However we do not know the explicit form of this functional. The interaction term $\widehat{U}$ and kinetic energy $\widehat{T}$ as a functional of the density are not exactly known. Writing this functional formally down in eq. (2.6) is correct, but for a practical application an approximation for these two terms is needed, leading to an approximated solution.

A possible way to approximate these unknown terms, $\widehat{U}$ and $\widehat{T}$, is by replacing the true unknown kinetic energy by that of a uniform electron gas and the interaction energy by that of the Hartree energy,

$$E_H[n] = \frac{1}{2} \int \frac{n(\overline{r}) n(\overline{r}')}{|\overline{r} - \overline{r}'|} d\overline{r} d\overline{r}'. \tag{2.7}$$

The remaining correction terms are now grouped in an exchange-correlation term E_{xc} [23]:

$$E[n] = T_s[n] + (T[n] - T_s[n]) + V[n] + E_H[n] + (U[n] - E_H[n]) \tag{2.8}$$

$$E[n] = T_s[n] + V[n] + E_H[n] + E_{xc}[n]. \tag{2.9}$$

The reason for this procedure is that the exchange-correlation term can be viewed as a perturbation term for which a rough approximation can already give good results.

[1] As the ground-state density determines the external potential, the Hamiltonian is a functional of the density and thus also excited wavefunctions are a functional of the density.

Until now we have formally solved the many-body problem. In doing so we have transferred the problem to finding a universal functional for the exchange-correlation. Its accuracy will only depend on the used approximation. The most used approximations in solid-state physics are LDA (Local Density Approximation) and GGA (Generalized Gradient Approximation).

2.2 Kohn-Sham equation

The most common way to solve the minimization problem is via the Kohn-Sham scheme (KS). In this method the ground-state density is calculated through single-particle orbitals in an auxiliary potential. This auxiliary potential is found by using the fact that the energy has a minimum for the solution of the ground-state density

$$\delta E[n] = \delta E[n + dn] - \delta[n] = \int dr \frac{\delta E[n]}{\delta n} \delta n \tag{2.10}$$

$$\frac{\delta E[n]}{\delta n} = 0. \tag{2.11}$$

and comparing the solution of DFT for a non-interacting system to that of an interacting one where we know how to find the ground-state density. Using the fact that the interaction and kinetic energy are universal, we see that we can define an auxiliary potential of a non-interacting system which leads to the same density as the interacting one:

$$(-\frac{1}{2} \bigtriangledown^2 + v_{eff}(\overline{r}) - \epsilon_j)\phi_j(\overline{r}) = 0, \tag{2.12}$$

where

$$v_{eff}(\overline{r}) = v(\overline{r}) + v_H(\overline{r}) + v_{xc}(\overline{r}) \tag{2.13}$$

$$v_H = \int \frac{n(\overline{r}^{'})}{|\overline{r} - \overline{r}^{'}|} d\overline{r}^{'} \tag{2.14}$$

$$v_{xc}(\overline{r}) = \frac{\delta}{\delta n(\overline{r})} E_{xc}[n(\overline{r})]. \tag{2.15}$$

This means that the single-particle solutions of the non-interacting system with this external auxiliary potential will lead to the same ground-state density,

$$n_0(\overline{r}) = \sum_{j=1}^{N} |\phi_j(\overline{r})|^2 \tag{2.16}$$

as DFT applied to the interacting one.

It is important to realize that these single-particle wavefunctions have no physical meaning. It is just the density resulting from these single-particle orbitals that has physical meaning. Quite astonishing is that in some situations the orbitals can serve as a first approximation for the many-body wavefunction anyway and can be used for the entire spectrum [24, 25, 26]. This will be further discussed in chapter 3. In summary, DFT actually replaces the very complicated many-body problem by two more simple problems. We have to solve the KS equations and try to find an approximate functional.

The equivalence between the minimization problem and solution of the Kohn-Sham equations simplifies the many-body problem significantly. Solving the Kohn-Sham equation is relatively

simple because it can be solved as an independent-particle model with just three spatial variables. The Kohn-Sham wavefunctions give, in turn, the exact ground state density and every physical property is a functional of this density. Nevertheless, some functionals are not dependent on the total density alone. A functional that also depends on the Kohn-Sham wavefunction is called an implicit density functional. An example of an implicit functional can be obtained for the total energy by rewriting equation (2.9) by

$$E[n] = \sum_i \varepsilon_i - \frac{1}{2}\int\int \frac{n(\overline{r'})n(\overline{r})}{|\overline{r} - \overline{r'}|} d\overline{r} d\overline{r'} - \int v_{xc} n(\overline{r}) d\overline{r} + E_{xc}[n] \tag{2.17}$$

2.2.1 Spin Density Functional Theory (SDFT)

In the previous derivation, the exchange-correlation functional was independent of spin. In practice one can obtain better solutions when spin [27] is included. This means that the exchange-correlation term is now dependent on spin-polarized densities, up and down, instead of the total density, which arises by adding the spin up and down densities. This leads to two Kohn-Sham equations

$$[-\frac{1}{2} \bigtriangledown^2 + v_{s_i}^{eff}(\overline{r})]\varphi_{\sigma_k s_k}(\overline{r}) = \varepsilon_{\sigma_k s_k}(\overline{r}) \tag{2.18}$$

$$v_{s_k}^{eff}(\overline{r}) = v(\overline{r}) + \int \frac{n(\overline{r})}{|\overline{r} - \overline{r}'|} d\overline{r} + v_{s_k}^{xc}(\overline{r}) \tag{2.19}$$

that are coupled due to the total density that is part of the effective potential (both for spin up and down).

An extra advantage of using spin-dependent DFT is that the magnetization of the atoms is obtained in a straightforward way:

$$\widehat{m}_z(\overline{r}) = -\mu_B(\widehat{n}_\uparrow(\overline{r}) - \widehat{n}_\downarrow(\overline{r})) \tag{2.20}$$

A calculation that includes spin is called an unrestricted calculation, in contrast with a spinless calculation, which is called a restricted calculation. The problem with including spin is the practical implementation in the simulation code: because of imperfections in the optimizer, the solution may become dependent on the initial magnetization. When minimizing the spin configurations, the flaws of the optimizer lead us to a local energy minimum instead of the absolute minimum (see also section 4.2.1) [28, 29]. An example are the antiferromagnetic and ferromagnetic states in Cr_2O_3. These states all exist in their own local minimum and the optimizer is unable to go from one minimum to the other as it varies the spin on the atom in a continuous way. Another reason why the optimizer gets stuck in a local minimum is because it preserves the symmetry. A ferromagnetic state has a different symmetry than an antiferromagnetic one and during the simulation the optimizer keeps the symmetry of this ferromagnetic state, making it unable to go to the more stable antiferromagnetic state.

We conclude that in order to find the correct absolute minimum all possible magnetic states should be tested and compared to determine the most stable state. All calculation where preformed with SDFT and as seen the extension of DFT to SDFT is obvious. In the remaining we therefore discuss DFT to keep things as simple as possible.

2.3 Solution of Kohn-Sham equation

The Kohn-Sham equations are solved by proposing – a well chosen – basis set in which the Kohn-Sham Hamiltonian can be diagonalized. This last part is computationally demanding and in order to reduce the computational effort a good basis set is essential. It should be noted that the effective potential depends on the density which is coupled with the Kohn-Sham orbitals. In this way the problem has to be solved self-consistently. In this chapter we discuss a natural basis for a periodic ideal solid and the reductions this basis set induces in solving the self-consistent problem. It will be explained how the form of these Kohn-Sham orbitals lead to the band structure.

2.3.1 Bloch wave functions as solutions for solids

The most important part of solving the Kohn-Sham Hamiltonian is choosing the basis set. In a periodic solid, which is an infinitely extended material, the plane-wave basis set arises naturally through symmetry arguments. Such an ideal crystalline solid is a repetition of a unit cell and extends infinitely in the 3 dimensions. Consequently translational symmetry is present: the crystal is invariant when translated over a vector connecting two equivalent atoms of the crystal (this vector we call $\overline{T}$) (see Fig. 2.1). As the crystal has this translational symmetry, so does

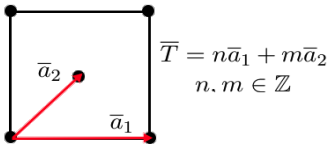

Figure 2.1: Translational symmetry in a 2D lattice where a_1 and a_2 are primitive basis vectors of the lattice.

the density. Because of the symmetry of the external potential and the density dependence of the other terms in the Hamiltonian, the entire Kohn-Sham Hamiltonian is therefore invariant to the same symmetry as well. The symmetry of the Kohn-Sham Hamiltonian corresponds to the lattice of the system and the eigenstates of such a Hamiltonian are so-called Bloch wave functions:

$$\Psi_{\overline{k}}(\overline{r}) = u_{\overline{k}}(r)e^{i\overline{k}\cdot\overline{r}} \tag{2.21}$$

where the function $u_{\overline{k}}(\overline{r})$ contains the translational symmetry of the lattice meaning that

$$u_{\overline{k}}(\overline{r} + \overline{T}) = u_{\overline{k}}(\overline{r}). \tag{2.22}$$

where $\overline{k}$ is a quantum number indicating a orbital for two electrons with opposite spin. The reason that this quantum number is continuous is because we consider an infinitely extended solid in all three dimensions, leading to a many-body problem with infinitely many electrons.

Simplifying the Bloch functions due to the translational symmetry

The primitive reciprocal unit cell or 1^{st} Brillouin zone (1BZ) contains the full symmetry of the solid material [2]. The quantum number $\overline{k}$ that fills the total reciprocal space[3], can be reduced to the 1BZ, by the use of reciprocal lattice vectors $\overline{G}$. The reduction of $\overline{k}$ to the 1BZ induces a new quantum number n with is called the band index. This can be seen as follows:

$$\overline{k} - \overline{G} = \overline{k'} \tag{2.23}$$

with $\overline{k}$ outside the 1BZ and $\overline{k'}$ in the 1BZ. Combining this with (2.21) we get

$$\Psi_{\overline{k}}(\overline{r}) = u_{\overline{k}}(r) e^{i\overline{k'}\cdot\overline{r}} e^{i\overline{G}\cdot\overline{r}}. \tag{2.24}$$

This can be written as a Bloch function because $u_{\overline{k}}(r)e^{i\overline{G}\cdot\overline{r}}$ has the symmetry of the real space lattice.

$$\Psi_{\overline{k}}(\overline{r}) = u'_{\overline{k}}(r) e^{i\overline{k'}\cdot\overline{r}} \tag{2.25}$$

Introducing the band index, which indicates how many times one has to cross a reciprocal cell, gives us a simplified form of the wavefunction.

$$\Psi_{n\overline{k'}}(\overline{r}) = u_{n\overline{k'}}(r) e^{i\overline{k'}\cdot\overline{r}}. \tag{2.26}$$

This simple form of the wavefunctions is characterized by two quantum numbers, i.e. the band index and the wave vector $\overline{k}$ restricted to the 1BZ. These quantum numbers are related to the band structure and are discussed in next chapter.

As the Kohn-Sham wavefunction can be written as

$$\Psi_{n\overline{k}}(\overline{r}) = u_{n\overline{k}}(\overline{r}) e^{i\overline{k}\cdot\overline{r}} \tag{2.27}$$

and $u_{n\overline{k}}(\overline{r})$ is periodic with the translational vector of the lattice, we can write this function as a discrete Fourier series (A.1) given by

$$u_{n\overline{k}}(\overline{r}) = \sum_{\overline{G}} C_n^{\overline{k}}(\overline{G}) e^{i\overline{G}\cdot\overline{r}}. \tag{2.28}$$

This combined with the form of the wavefunction

$$\Psi_{n\overline{k}}(\overline{r}) = \sum_{\overline{G}} C_n^{\overline{k}}(\overline{G}) e^{i(\overline{k}+\overline{G})\cdot\overline{r}} \tag{2.29}$$

indicates that the wavefunction can be written as an expansion in plane-waves from which naturally the choice for a plane wave basis set arises.

[2] Any particular shape of the primitive reciprocal unit cell can be transformed in the 1BZ by use of the reciprocal translation vector $\overline{G}$.

[3] More information on what we mean with reciprocal space can be found in appendix A)

2.3.2 Limitation of plane-wave basis set

Solving the Kohn-Sham equation leads to the best approximation for the ground-state density using one Slater determinant for all electrons[4] within the approximation used for the exchange-correlation term. On the other hand, the core states wavefunctions are very localized, making them difficult to describe with plane waves. These core states are however not that interesting for the chemical binding and luminescent properties and can be avoided in the calculation. As core states are localized they can be treated in a different way than the valence electrons. There are two major methods to do this: via the use of pseudopotentials or the PAW method.

Pseudopotentials

In the pseudopotential (PP) method the core electrons are combined with the ions and described via an effective potential, the pseudopotential. To obtain a valence wavefunction that can be expanded with a few plane waves, the pseudopotential is developed in order to obtain a smooth valence wave function (see Fig. 2.2).

A pseudopotential that has the right valence wavefunction outside the core can, for example, be constructed by the recipe of Troullier Martins [30]:

1. Solve the free atom all-electron (AE) radial Kohn-Sham equation:

$$[\frac{1}{2}\frac{d^2}{dr^2} + \frac{l(l+1)}{2r^2} + v_{KS}^{AE}[n^{AE}(r)]]rR_{nl}^{AE}(r) = \varepsilon_{nl}^{AE} rR_{nl}^{AE}(r) \tag{2.30}$$

   were

$$v_{KS}^{AE}[n^{AE}(r) = -\frac{Z}{r} + v_H[n^{AE}](r) + v_{xc}[n^{AE}](r). \tag{2.31}$$

2. Choose a cut-off radius r_0 larger than any node of the AE wavefunction.

3. Conditions for the ansatz for a norm conserving PP-wavefunctions $R_{nl}^{PP}(r)$:

   - $r > r_0$, then $R_{nl}^{PP}(r) = R_{nl}^{AE}(r)$
   - $r < r_0$, then $\int_0^{r_0} |R_{nl}^{PP}|^2 r^2 dr = \int_0^{r_0} |R_{nl}^{AE}|^2 r^2 dr$

4. The screened pseudopotential can then be obtained from Eq. 2.30:

$$v_{scr,nl}^{PP}(r) = \varepsilon_{nl}^{PP} - \frac{l(l+1)}{2r^2} + \frac{1}{2rR_{nl}^{PP}(r)}\frac{d^2}{dr^2}(rR_{nl}^{PP}(r)) \tag{2.32}$$

5. Remove screening effects

$$v_{nl}^{PP}(r) = v_{scr,nl}^{PP}(r) - v_H[n^{AE}](r) - v_{xc}[n^{AE}](r) \tag{2.33}$$

The screening is system-dependent and is reason it is subtracted. The unscreened potential is then used to represent the effective potential of the nuclei and the core electrons where the screening of the electrons should be added again.

[4] DFT is also called a density optimum solution method in contrast to the Hartree-Fock, which is an energy optimum method. This is because only one (two for SDFT) Slater determinant of single-particle orbitals is used to approximate the density or energy with respectively DFT or Hartree-Fock

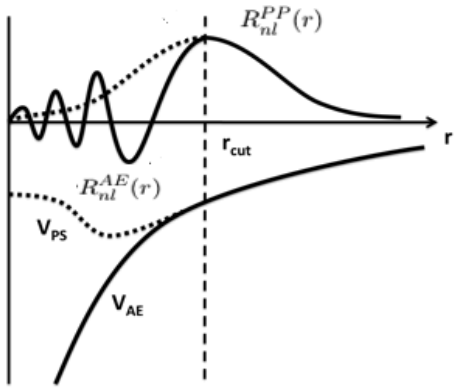

Figure 2.2: Pseudopotentials and pseudo wavefunction, which is a much smoother wavefunction than the all-electron solution. This smooth wavefunction coincides with the all-electron wavefunction at larger distance [31].

Projected-augmented wave (PAW)

The pseudopotential method has features that are non-physical. This is due to the fact that the number of nodes of the valence wavefunction is ill-described due to the smoothing.

To obtain a fast computational method that captures the correct physics, it is sometimes crucial to have a combination of a physically correct solution for the valence electrons while keeping the core electrons fixed. Correspondingly the projected-augmented wave method (PAW) combines these two and in comparison to pseudopotentials the valence wavefunctions have the correct number of nodes [32, 33].

The PAW method obtains the real physical wavefunction from a pseudo wavefunction that is calculated. The real wavefunction can, in contrast to the pseudopotential scheme, be found by a transformation T that maps the pseudo wavefunction on the real physical wavefunction with the correct number of nodes:

$$|\psi\rangle = T|\widehat{\psi}\rangle. \tag{2.34}$$

In this way only the transformation operator has to be found and with it the Kohn-Sham equation can be transformed into an equation for the pseudo wavefunction. This pseudo wavefunction can be described with a few plane waves and a local partial-wave basis set in contrast to the all-electron solution. The scheme is a frozen-core method and the core states are fixed, but compared to the pseudopotential method the final wavefunction has the correct number of nodes and thus contains more physics than just a pseudo wavefunction from the pseudopotential method.

2.4 Irreducible Brillouin Zone

In section 2.3.1 the focus was on the translational symmetry to simplify the form of Kohn-Sham orbitals. In a unit cell there are additional symmetries that give us an extra reduction of the $\overline{k}$ values we need to consider. The part of the reciprocal space that has to be considered is called the irreducible Brillouin Zone (IBZ).

Let us quickly explain how this reduction of the IBZ is obtained. We already know that the solutions of the Kohn-Sham Hamiltonian can be written as a Bloch function with band index

and wave vector as quantum numbers. Applying a Kohn-Sham Hamiltonian to a Bloch function leads to,

$$[\frac{1}{2}(\frac{\overline{\nabla}}{i}+\overline{k})^2+U(\overline{r})]u_{\overline{k},n}(\overline{r})=\varepsilon_{\overline{k},n}u_{\overline{k},n}(\overline{r}), \tag{2.35}$$

with $U(\overline{r})$ an external potential with the symmetry of the unit cell and the translational symmetry.

Representing a symmetry of the unit cell by a matrix R, we can write,

$$\Psi_{R\overline{k},n}(R\overline{r})=u_{R\overline{k},n}(R\overline{r})e^{iR\overline{k}\cdot R\overline{r}}=u_{R\overline{k},n}(R\overline{r})e^{i\overline{k}\cdot\overline{r}} \tag{2.36}$$

where the invariance of the scalar product is used. The above Bloch wavefunctions (Eq. 2.36) have the same $\overline{k}$ value and thereby applying them to the Kohn-Sham Hamiltonian leads to the same Hamiltonian as (2.35) given by:

$$[\frac{1}{2}(\frac{\overline{\nabla}}{i}+\overline{k})^2+U(R\overline{r})]u_{R\overline{k},n}(R\overline{r})=\varepsilon_{R\overline{k},n}u_{R\overline{k},n}(R\overline{r}). \tag{2.37}$$

As the potential $U(\overline{r})$ is invariant for the symmetry represented by R we conclude that (assuming no degeneracy):

$$u_{R\overline{k},n}(R\overline{r})=u_{\overline{k},n}(\overline{r}) \tag{2.38}$$

$$\Psi_{R\overline{k},n}(R\overline{r})=\Psi_{\overline{k},n}(\overline{r}). \tag{2.39}$$

This can be rewritten to see the reduction of the 1BZ to the IBZ by replacing $\overline{k}$ by $R^{-1}\overline{k}$:

$$\Psi_{R^{-1}\overline{k},n}(\overline{r})=\Psi_{\overline{k},n}(R\overline{r}). \tag{2.40}$$

The last equation shows that states (wavefunctions) characterized by a k point in the reciprocal space (and band index n) can be calculated from the wavefunction of a different k point that is connected through a symmetry operator R of the lattice (both wavefunctions also have the same energy). The part of the 1BZ that unfolds to the total 1BZ is called the irreducible BZ (IBZ) and is enough to calculate all wavefunctions.

In summary there are two important symmetries that lead to a reduction of the calculations. The first one is translational symmetry, which gives rise to the quantum number $\overline{k}$ and a reduction of the total reciprocal space to the 1BZ. Second, the other symmetry operations such as rotations in the unit cell lead to an extra reduction of the necessary $\overline{k}$ points corresponding to the reduction of the 1BZ to the IBZ.

2.5 The band index

The explanation of the band index is rather simple when looking back to the Hamiltonian applied to the Bloch wavefunctions (2.35). In this equation the external potential $U(\overline{r})$ represents the effective Kohn-Sham potential. It is clear that for a single k, the band index enumerates the different eigenvalues in order of increasing energy. For all the $\overline{k}$ values, this gives for every band index a surface in reciprocal space, i.e. an energy surface as a function of the $\overline{k}$ values.

In principle there are an infinite number of bands to describe the occupied and excited states. However we do not need to calculate them all, nor are we able to. The expansion of the Bloch

function in plane waves for a given k point in reciprocal space determines how many bands can be calculated. This expansion is given by

$$u_{\overline{k},n}(\overline{r}) = \sum_{\overline{G}} C_n^{\overline{k}}(\overline{G}) e^{i\overline{G}\cdot\overline{r}}. \tag{2.41}$$

The number of basis functions $e^{iG.r}$ depends on the number of reciprocal lattice points, denoted by the $\overline{G}$ vectors, and therefore determines how many eigenvalues (and bands) are calculated for every $\overline{k}$ point.

A related remark is that the number of $\overline{G}$ vectors also determines the precision with which the energy and its corresponding Kohn-Sham orbitals are approximated. In most cases, the number of reciprocal lattice vectors needed for the desired precision is much larger than the number of necessary bands (see section 4.1) .

2.6 Reciprocal grids

In this section it is explained how the wave vector, a continuous quantum number, is discretized because of periodic boundary conditions, and how this can be interpreted in different ways..

2.6.1 Discretization of the wave vector

The wave vector $\overline{k}$ is a real-valued, continuous quantum number that can be restricted to the IBZ. A continuous quantum number is however not convenient to work with. In this section, we show how starting from the application of periodic boundary conditions, we can derive the discretization of the quantum number k in a natural way.

Let us now briefly show how a periodic boundary condition leads to the transformation of continuous to discrete quantum numbers. If a_i are the lattice vectors in real space, then a periodic boundary condition means that there exists a N_i such that

$$\Psi_{\overline{k},n}(\overline{r} + N_i\overline{a}_i) = \Psi_{\overline{k},n}(\overline{r}) \tag{2.42}$$

where N_i is an integer that represents the number of times the unit cell is repeated, in the a_i direction before the periodic boundary condition is applied[5]. It is then instructive to write the wavefunction as a Bloch function:

$$\Psi_{\overline{k},n}(\overline{r} + N_i\overline{a}_i) = u_{\overline{k},n}(r) e^{i\overline{k}\cdot\overline{r}} e^{i\overline{k}\cdot N_i\overline{a}_i}. \tag{2.43}$$

In the basis of the reciprocal space, $\overline{k} = x_1b_1 + x_2b_2 + x_3b_3$ with b_i given by (A.2, A.3, A.4) and x_i a real number between 0 and 1 (restricting it to the 1BZ or a translation of it) Eq. (2.43) can then be simplified to

$$\Psi_{\overline{k},n}(\overline{r} + N_i\overline{a}_i) = u_{\overline{k},n}(\overline{r}) e^{i\overline{k}\cdot\overline{r}} e^{i\overline{k}\cdot N_i\overline{a}_i} = u_{\overline{k},n}(\overline{r}) e^{i\overline{k}\cdot\overline{r}} e^{2\pi x_i N_i i} = \Psi_{\overline{k},n}(\overline{r}) e^{2\pi x_i N_i i}. \tag{2.44}$$

From this expression it is easy to see that

$$\overline{k} = \frac{m_1}{N_1}\overline{b}_1 + \frac{m_2}{N_2}\overline{b}_2 + \frac{m_3}{N_3}\overline{b}_3 \tag{2.45}$$

[5]After repeating the system the only thing that is being calculated is the wavefunction of such a system with the mentioned periodic boundary condition (the atoms are also fixed).

where m_i are integers so, m_i/N_i determine the discrete $\overline{k}$ point in the 1BZ. The number of $\overline{k}$ points in the 1BZ is simply $N_1N_2N_3 = N$ or equal to the number of unit cells V/V_p

As a side note we can see that 1 k points takes a space of

$$(\triangle\overline{k})^3 = \frac{\overline{b_1}\cdot(\overline{b_2}\times\overline{b_3})}{N_1N_2N_3} = \frac{(2\pi)^3}{NV_p} = \frac{(2\pi)^3}{V} \tag{2.46}$$

in the reciprocal space. This will be used to introduce the DOS (see section 3.2.1).

2.6.2 Interpretation of the discretized wave vector.

The band index was straightforward to interpret, but the wave vector has some more facets. In the subsequent paragraphs three different views on this quantum number and its connection with an infinite solid will be handled. The approximation made by not simulating an infinite solid will be briefly discussed.

Repetition of the unit cell

A first interpretation of the discrete $\overline{k}$ points (Eq. 2.45) in the 1BZ reflects the periodic boundary conditions that are set on the boundary created by taking N_i times the unit cell in the direction of $\overline{a}_i$. In the case of a molecule, for example, periodic boundary conditions are unphysical, so one $\overline{k}$ point in all directions is enough. The same is true with a surface where in one direction there is no use to apply periodic boundary conditions over more than one cell making the mesh denser increases the distance over witch the periodic boundary conditions are applied, leading to a less molecule- or surface-like type system.

One has to remember that the periodic boundary conditions are not set by specifying how many times the unit cell is repeated. Instead one states how dense the $\overline{k}$ mesh should be [34].

Phase factor in LCAO

An other view on the meaning of a $\overline{k}$ point arises from a totally different perspective. It is related to the character of the density (see section 3.2.1) around an atom and originates from the use of another basis set. This basis set is called Linear Combination of Atomic Orbitals (LCAO) and approximates the wavefunction by atomic-like orbitals located on the atomic positions.

$$\chi_{\alpha,\overline{k}} = \frac{1}{\sqrt{A}}\sum_{\overline{R}_I}^{M}\gamma_I(\overline{k})\hat{\varphi}_\alpha(\overline{r}-\overline{R}_I), \tag{2.47}$$

where M is the number of atoms and $\hat{\varphi}_\alpha$ are the atomic orbitals, for example, coming from the numerical solution of the atomic Kohn-Sham equations (α = 1s, 2s, 2p, ...).

Again the coefficient, $\gamma_I(\overline{k})$, needs to be chosen in such a way that translational symmetry is incorporated. To make sure that this is the case, the coefficient has to be taken equal to

$$\gamma_I(\overline{k}) = e^{i\overline{k}\cdot\overline{R}_I}. \tag{2.48}$$

The total wavefunction can now be written as a superposition of the basis functions in the following form:

$$\psi_n(\overline{k},\overline{r}) = \sum_\beta c_{n\beta}(\overline{k})\chi_\beta(\overline{k},\overline{r}). \tag{2.49}$$

The idea of this basis set is that you can use a minimal basis set. In that case, the coefficient $\gamma_I(\overline{k}) = e^{i\overline{k}\cdot\overline{R}_I}$ can be seen as a phase factor between orbitals located on different atoms. The phase factor has values +1 when $\overline{k} = 0$ and -1 when $\overline{k} = \frac{1}{2}\overline{G}$ which is the edge of the Brillouin zone. Figure 2.3 shows how such an interpretation can be used to qualitatively discuss the stability of the arrangement of orbitals and draw the band structure.

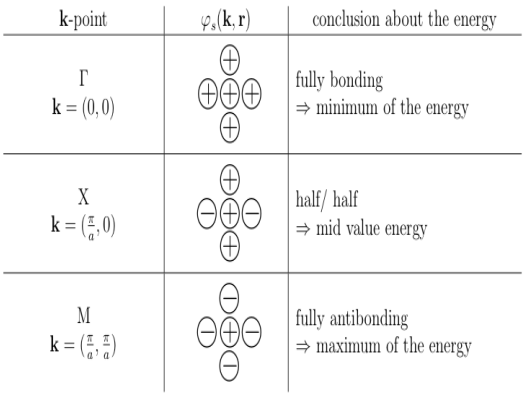

(a) Phase between orbitals

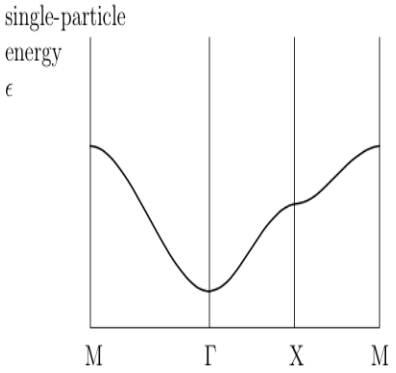

(b) Band structure

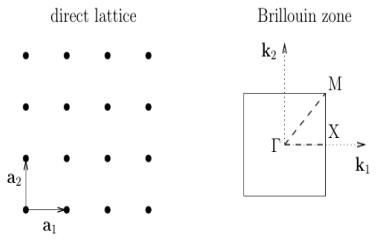

(c) Reciprocal and direct lattice

Figure 2.3: A cubic lattice where the band structure is constructed from tight-binding theory. The minimal basis set, only the s orbitals, is used to construct a qualitative band structure [35].

Numerical consideration

For an infinite solid, k is a continuous quantum number. In that case, computing the wavefunctions for each k-point would be unfeasible. On the other hand, periodic boundary conditions lead to a discretization of the k wave vector. Using such a k-mesh approximates the solution of an ideal, infinite solid, but makes it also possible to obtain numerical results within a finite time. It is therefore important to find a compromise between precision and computational effort. We will check which density of k mesh should be used in section 4.1.

Chapter 3

Band structure

In previous chapters, we explained the fundamental theories which we need to explain the band structure [36]. The quantities and information that can be extracted out of the band structure will be discussed in this chapter.

3.1 What is a band structure?

A band structure is often considered as a convenient way to extract electronic and spectroscopic information. Nevertheless, it is based on an approximate description of the solid under study. The approximation consists in replacing the complicated many body-system by an independent-particle model. This independent-particle model is represented by a single-particle potential and should have the correct symmetry corresponding to the original Hamiltonian.

In DFT it is the Kohn-Sham effective potentials that generate this independent-particle model. In the previous chapter we explained how translational symmetry leads to Bloch single-particle wavefunctions (see section 2.3.1). These quantum numbers and Bloch wavefunctions correspondingly lead to a dispersion relation as function of $\overline{k}$, $\varepsilon_{\overline{k},n}$, see equation (2.35). This dispersion relation represents energy surfaces as a function of k where every surface has a different band index n. For visualization purposes, the dispersion relation is not displayed as surfaces but is shown along border lines of the IBZ (high-symmetry lines). This particular representation is called the band structure.

The idea behind such a band structure is that interacting electrons in a solid create a positive charge around them because interelectronic repulsion gives rise to a local deficiency of electrons. This electron-hole combination can be considered as a quasiparticle that is weakly interacting with the other electrons.

The band structure that is measured in experiments by using Angle-Resolved Photo Electric Spectroscopy (ARPES) [37, 38], has, at first sight, nothing to do with these Kohn-Sham orbitals. Because the density of the quasiparticles is a good approximation of the correct ground state density, we assume that the Kohn-Sham scheme originally proposed for ground-state properties, are a reasonable approximation for these quasiparticles and consequently for the experimentally determined band structure.

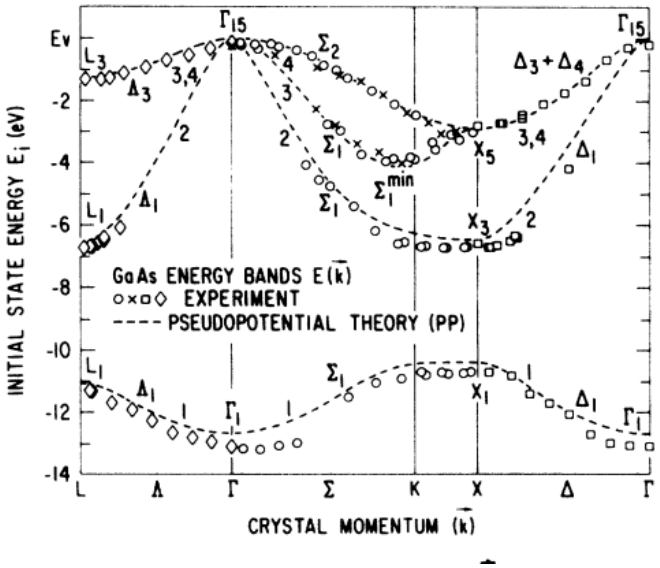

Figure 3.1: Angle-Resolved Photo Electric Spectroscopy (ARPES) [37] used for obtaining the band structure of GaAs compared with a calculated band structure [39] by constructing af a non-local pseudopotential.

3.2 Extracting information from the band structure

The band structure actually represents the possible states (quasiparticles) that can be occupied. The band structure therefore has the ability to assess whether a material is an insulator (large band gap), a semiconductor (a relatively small band gap) or a metal (no band gap). In a band structure, it is also possible to see if a band gap is direct or indirect. In (in)direct band gap materials the maximum of the valence band and minimum of the conduction band correspond to the same (different) wave vector. The density of states (DOS) is a much simpler tool to analyze a material, but the information contained in it is also reduced compared to the band structure because in the DOS the properties of different bands are averaged out.

3.2.1 Density of states and integrated density of states

The density of states (DOS) is the number of states within an energy interval $[E, E + dE]$ per volume of the unit cell. It can be determined from the total number of states with an energy below a certain threshold given by:

$$N(E) = \sum_{\overline{k},n,\sigma} \theta(E - E(\overline{k}, n)). \tag{3.1}$$

This corresponds to the integrated density of state, where n is the band index, $\overline{k}$ the wave vector, σ the spin projection and θ the step function. The DOS is obtained by taking the derivative of the above expression:

$$D(E) = \frac{dN(E)}{dE} = \sum_{\overline{k},n,\sigma} \delta(E - E(\overline{k}, n)) \tag{3.2}$$

Because one $\overline{k}$ point takes a space of $(2\pi)^3/V$ (see Eq. (2.46)), we can rewrite the expression for the DOS as

$$D(E) = \frac{V}{(2\pi)^3} \sum_{n,\sigma} \int d\overline{k}\ \delta(E - E(\overline{k}, n)) \tag{3.3}$$

When the density is expressed per unit cell we get

$$D(E) = \frac{V_p}{V} \frac{V}{(2\pi)^3} \sum_{n,\sigma} \int d\overline{k}\ \delta(E - E(\overline{k}, n)) \tag{3.4}$$

$$D(E) = \frac{V_p}{(2\pi)^3} \sum_{n,\sigma} \int d\overline{k}\ \delta(E - E(\overline{k}, n)) \tag{3.5}$$

3.2.2 Local density of states

The local DOS expresses how many states are accessible in an atom-like orbital centered around an atom. Properties related to atomic orbitals allow for a much easier interpretation of chemical concepts, such as the kind of binding and the character of a band. To obtain the local DOS, we write equation (3.2) in a different form

$$D(E) = \sum_{n,\overline{k},\sigma} \langle \psi_{n,\overline{k}} | \psi_{n,\overline{k}} \rangle \delta(E - E(n, \overline{k})). \tag{3.6}$$

From this we go to the local DOS (LDOS) by inserting a completeness relation

$$D(E) = \sum_{\alpha,\mu} \left[\sum_{n,\overline{k},\sigma} \langle \psi_{n,\overline{k}} | \phi_{\alpha,\mu} \rangle \langle \phi_{\alpha,\mu} | \psi_{n,\overline{k}} \rangle \delta(E - E(n, \overline{k})) \right] \tag{3.7}$$

where the set $|\psi_{\alpha,\mu}\rangle$ are atomic orbitals with quantum numbers $\mu = nl$ localized on the atom α. Eq. (3.7) can be rewritten as a sum of densities corresponding to the projections on $|\psi_{\alpha,\mu}\rangle$,

$$D(E) = \sum_{\alpha,\mu} D_{\alpha,\mu}(E), \tag{3.8}$$

where

$$D_{\alpha,\mu}(E) = \sum_{n,\overline{k},\sigma} |\langle \psi_{n,\overline{k}} | \phi_{\alpha,\mu} \rangle|^2 \delta(E - E(n, \overline{k})). \tag{3.9}$$

In this expression, $\langle \psi_{n,\overline{k}} | \phi_{\alpha,\mu} \rangle$ is the projection of the wavefunction with quantum numbers $\overline{k}$ and n onto the atomic orbital $\phi_{\alpha,\mu}$, and its modulus squared gives a measure of the atom-like character.

The local density of states (LDOS), $D_{\alpha,\mu}(E)$, can be rewritten as:

$$\rho_{\alpha,\mu}(E) = \sum_{n,\overline{k},\sigma} \int \int \overline{\psi}_{n,\overline{k}}(\overline{r}) \phi_{\alpha,\mu}(\overline{r}) \overline{\phi}_{\alpha,\mu}(\overline{r}') \psi_{n,\overline{k}}(\overline{r}') \delta(E - E(n, \overline{k})) d\overline{r} d\overline{r}' \tag{3.10}$$

From this equation it is clear that the LDOS gives us an average character of the states between E and $E + dE$.

3.3 Band structures for a supercell

Generally impurities are of low concentration and should not be close to each other. The primitive cell (PC), by itself, is too small to do this and a supercell (SC) has to be used. In our persistent phosphor the luminescent behavior of the chromium emission center is examined and this is an impurity in the host material leading to the need of a SC.

The disadvantage of using a SC is that its band structure is defined in a smaller BZ compared to the PC. A SC therefore has more bands than the primitive cell (PC) [40, 41, 42, 43, 44]. In our case of ZGO the SC has a volume of 4 times the PC (see also appendix. B). This means that 4 bands in the BZ of the SC correspond to 1 band in the BZ of the PC. The result of the SC calculations can be simplified by unfolding the band structure of the BZ of the SC to the BZ of the PC, hence the name band unfolding.

This folding can be understood by realizing that when increasing the size of the unit cell, in our case four times, the reciprocal lattice vectors, $\overline{G}$, become smaller. The parts of the BZ of the PC that do not fall in the BZ of the SC can be translated to the BZ of the SC over this smaller reciprocal lattice vector of the SC. This is illustrated in Fig. 3.2 where the SC is 2 times the PC. This folding due to the use of a SC is fully equivalent to the folding that gave rise to band indices (see section 2.5).

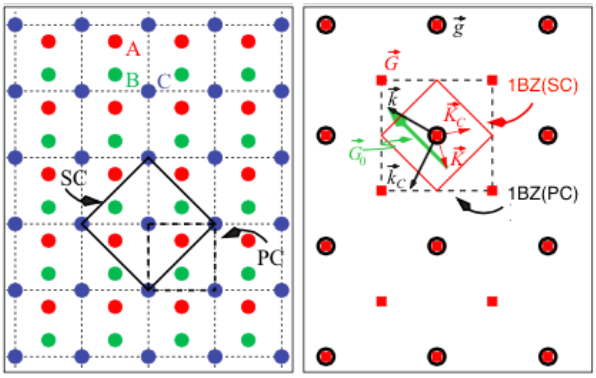

Figure 3.2: Band unfolding in 2 dimensions. The SC is twice as big as the reciprocal PC and points in the PC are folded back by use of the reciprocal lattice vector of the SC [45]. This folding is illustrated by point $\overline{k}$ that is translated by use of a SC reciprocal lattice vector, indicated in green, back to $\overline{K}$ located in the Brillouin zone of the SC, similar the point $\overline{k}_c$ can be translated to $\overline{K}_c$.

3.3.1 The need for band unfolding

Band folding can make a band structure look very complicated: by taking a bigger SC the number of bands increases. Comparing different SC of the same material therefore becomes difficult even though they contain the same physics. In recent years algorithms have been developed to unfold the band structure of a SC. In this thesis, we use the BANDUP algorithm [46, 47, 48]. The scheme of unfolding the band diagram of a SC only relies on the expansion

coefficients of the plane-wave basis.

$$\Psi_{\overline{k},n} = \sum_{\overline{G}} C_n^{\overline{k}}(\overline{G}) e^{i(\overline{k}+\overline{G})\cdot\overline{r}} \tag{3.11}$$

The unfolding is only exact when PC and SC have the same symmetry. Nevertheless nothing prohibits you to use the same scheme when this is not the case, for example when you take a larger cell and dope it with a small percentage of impurities[1]. Due to this small concentration of impurities the symmetry of the SC is almost the same as the undoped host material. Actually the scheme for unfolding the band structure takes this difference into account by averaging over different symmetry directions. On the other hand, this is also the disadvantage of the scheme because more wavefunctions have to be calculated than in an ordinary band structure (along high symmetry directions) and more memory is needed.

The big advantage of unfolding the band structure is the simplification you get compared to the SC band structure. The unfolded band structure of the doped material can then be compared with the band structure of the undoped material in the PC. The difference between the two band structures is solely due to the dopant. As some spectroscopic models explain luminescence in doped materials by the location of dopant states in the host material, such a scheme is very desirable. The location of these levels can also be determined by experiments by doing an ARPES experiment (see Fig. 3.1). The band unfolding provides a computational way of easily locating these levels in the band structure with the minimum amount of bands.

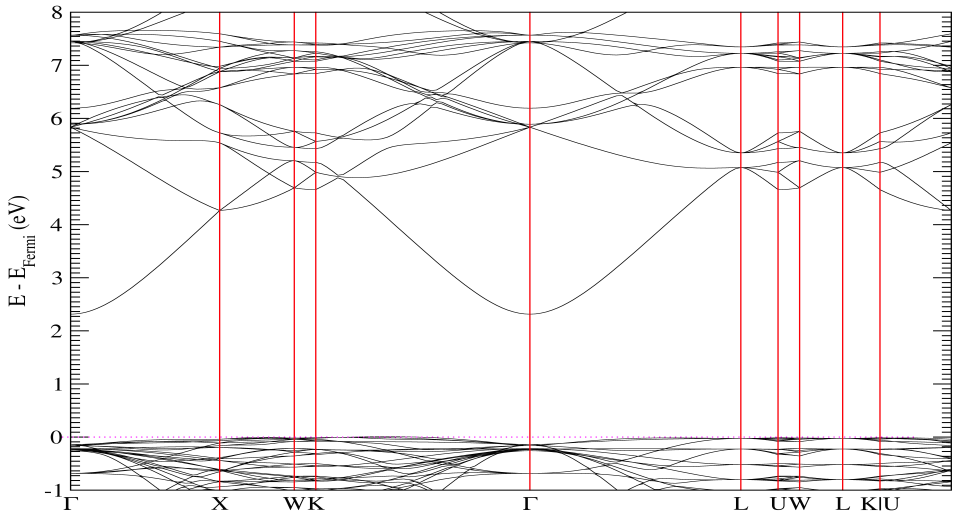

Figure 3.3: Band structure of a conventional ZGO SC. Compared to the unfolded band structure (see Fig. 3.4) we clearly see more bands.

Figure 3.3 and 3.4 illustrate the band unfolding concept for the pure ZGO material. The unfolded band structure (see Fig. 3.4) contains 4 times less band then the band structure in the SC (see Fig. 3.3) as the SC contains four times the volume of the PC. Although this is a relative small number of extra bands and therefore when taking such a small SC the band unfolding is not that necessary, applying this procedure is nevertheless very interesting as it simplifies the

[1]The transformation between the SC and PC reciprocal coordinates, which enables defining the band structure k-path, is explained in appendix B.

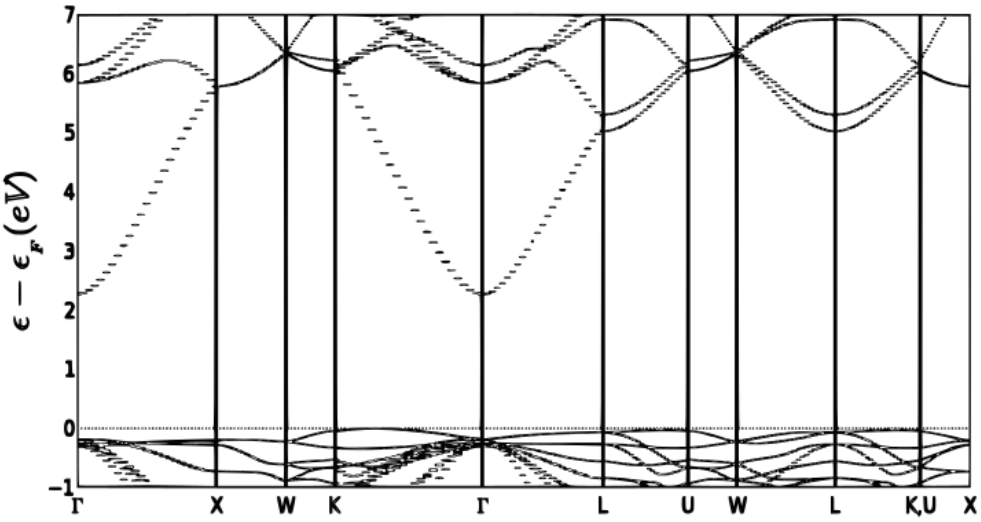

Figure 3.4: An unfolded band structure of a conventional ZGO SC. It perfectly matches the band structure of the primitive cell.

problem of analyzing the band structure. The added value of this approach is even larger when a bigger SC is used and the band structure of this SC becomes to cumbersome to inspect visually.

3.4 The meaning of the Kohn-Sham eigenvalue

In this section the meaning of the Kohn-Sham eigenvalues is discussed. The dispersion relation of these eigenvalues leads to the band structure. In general only the highest eigenvalue has a clear physical meaning and is equal to the ionization energy. Despite this, the subsequent paragraphs explain how we can give a meaning to all eigenvalues by making assumptions and using characteristics of DFT (Slater-Janak transition state).

3.4.1 Quasiparticles

The Kohn-Sham equation leads to wavefunctions of an auxiliary independent-particle system with the same ground state density as the many-body problem, within the approximation of the exchange-correlation term. These wavefunctions can be seen as quasiparticles in the many-body problem and quasiparticles have a clear physical meaning. It is been confirmed that the quasiparticle wavefunction and the Kohn-Sham wavefunction have a large overlap [49]. The Kohn-Sham equation is a single-particle equation and therefore assumes that different quasiparticles have no direct interaction with each other, such as a Coulomb like interaction. The quasiparticles only interact with each other because of the dependence of the effective single-particle potential on the ground-state density. This approximation is corrected in GW and advanced schemes to obtain better quasiparticle wavefunctions. In principle these schemes take more correlation between the quasiparticle into account.

To attribute meaning to the Kohn-Sham wavefunctions and eigenvalues, the link with quasiparticle wavefunctions is fundamental. These quasiparticles move in a potential that is dependent on the ground-state density. No excited-state interaction is thereby incorporated in this

potential. The unoccupied wavefunctions are generated by the same potential, which is determined by the ground-state density. We can now relate an excited state to an excitation of an occupied quasiparticle state to an unoccupied quasiparticle state. If we assume that the excitation changes the ground state density by only a small amount, we can assume that the potential of the occupied quasiparticles is also valid for the excited states. In a solid the excitation of one quasiparticle does not change the density much, as the number of electrons is large. It is therefore often a good approximation to interpret the unoccupied Kohn-Sham states in crystals as excited quasiparticle states.

3.4.2 Slater-Janak transition state

In Hartree-Fock theory, an essential tool in relating the difference in the eigenvalues to the excitation energy is Koopmans' Theorem. In DFT an equivalent theorem can be obtained that resembles Koopmans' Theorem and relates the eigenvalues of the Kohn-Sham equation to excitation levels. The DFT equivalent of Koopmans' theorem is obtained from Janak's theorem [50, 24] which states that when DFT is extended to fractional occupation of the Kohn-Sham orbitals, the derivative of the energy with respect to the fractional occupation is given by

$$\frac{\partial E}{\partial n_k} = \varepsilon_k(n_k) \tag{3.12}$$

with n_k the occupation of the ε_k level. By integrating this equation and assuming a linear dependence of the Kohn-Sham eigenvalue we obtain

$$I_k = E_k^{N-1} - E^N = -\int_0^1 \frac{\partial E_k(n_k)}{\partial n_k} dn_k = -\int_0^1 \varepsilon_k(n_k) dn_k = -\varepsilon_k(1/2) \cong -\varepsilon_k(1) \tag{3.13}$$

where E_k is the energy of a system where the k state is unoccupied and I_k can be seen as the ionization energy when removing the quasiparticle occupying this state (in the strict meaning of the word k should be equal to the highest occupation level). The ionization energy of the k state is equal to the $\varepsilon_k(1/2)$ and this expression is called the Slater-Janak transition state [51, 52]. If we approximate the eigenvalues as a constant, the Kohn-Sham eigenvalues are equal to this ionization energy. This approximation is exact for the occupation of the highest occupied level (HOMO), for which the eigenenergy is then exactly equal to ionization energy. Slater-Janak transition state theorem is equivalent with the Koopmans' Theorem in Hartree Fock but we relate the states to quasiparticle and do not approximate the total wavefunction like in Hartree-Fock Theory. This approximation can be justified because changing the occupation n_k of state k does not have a large impact on the total electron density if the number of electrons is large. A first approximation is therefore to assume that $\varepsilon_k(0) = \varepsilon_k(1/2) = \varepsilon_k(1)$ making it possible the relate the Kohn-Sham eigenvalues to I_k. Through these assumptions the excitation energy can now be calculated from the difference between two Kohn-Sham levels as the energies of the levels represent the energy that is needed to extract the quasiparticle[2].

[2]No extra electron-hole interaction has to be taken into account as we neglect interaction between the quasiparticles upon excitation

3.4.3 The band gap

An important property of a solid is its band gap. The band gap is defined by

$$E_g = I - A = (E(N-1) - E(N)) - (E(N) - E(N+1)). \tag{3.14}$$

using energy of the $N-1$, $N+1$ and N particle system. The band gap is related to the Kohn-Sham eigenvalues by the fact that the true ground state energy for fractional occupation is a linear interpolation of the energy at the adjacent integer occupations. We can therefore rewrite Eq. (3.14) as

$$E_g^{integer} = \frac{\partial E(N)}{\partial N}_{N+\delta} - \frac{\partial E(N)}{\partial N}_{N-\delta} \tag{3.15}$$

These derivatives can be calculated from the DFT expression for fractional occupation (Eq. 3.12) with the addition of an extra term, as proposed by Perdew et al. and Sham and Schlüter [53, 54]

$$E_g^{deriv} = \varepsilon_{LUMO}^{KS} - \varepsilon_{HOMO}^{KS} + \left(\frac{\partial E_{xc}}{\partial N}_{N+\delta} - \frac{\partial E_{xc}(N)}{\partial N}_{N-\delta} \right) = \varepsilon_{LUMO}^{KS} - \varepsilon_{HOMO}^{KS} + \Delta_{xc} \tag{3.16}$$

The difference between minimum of the conduction band ε_{LUMO}^{KS} and the maximum of the valence band ε_{HOMO}^{KS} can be seen in the band structure. The term Δ_{xc}, on the other hand arises from the discontinuity of the exact exchange-correlation term [55, 56, 54]. When using a PBE level of theory, which is not dependent on the occupation number of the Kohn-Sham orbitals, this term is zero. However the the band gap is then affected by systematic errors because semilocal functionals predict an incorrect behavior for fractional occupation. For these functionals, the energy does not take the form a straight line between integer occupation numbers, but a convex or concave behavior for fractional occupation and caused by the self interaction error. In this thesis a PBE functional is used for which a convex behavior is know leading to delocalization.

Another way the band gap can be calculated is by using the Slater-Janak transition state. We can write the ionization and the electron affinity as

$$I = \epsilon_{VB}(N - 1/2) \tag{3.17}$$

$$A = \epsilon_{CB}(N + 1/2) \tag{3.18}$$

and with these two relations we can write the band gap as

$$E_g = \epsilon_{CB}(N + 1/2) - \epsilon_{VB}(N - 1/2) = \epsilon_{CB}(N) - \epsilon_{VB}(N) + \Delta_{xc}. \tag{3.19}$$

Again by neglecting the variation of the eigenvalue when the HOMO or LUMO is filled with half an electron cause the error, this is equal to putting Δ_{xc} equal to zero.[3].

3.4.4 Improving the band structure

From the previous discussion we conclude that within DFT there is still much room for improvement [57]. There are several ways of improving this scheme.

[3]This discontinuity is also neglected in the discussion of the previous section where we assumed the eigenvalues as a function of the occupation remains approximately constant.

One way of improving the DFT band structure is by making the wavefunctions more localized. This is done by introducing an extra repulsive potential which is orbital-dependent. This scheme is called DFT+U where U is a parameter controlling the extra repulsion term [58]. Overall, the parameter U causes the electrons to be more localized, which is especially important for the d orbitals, although smaller orbitals such as s and p that can become even too localized [59]. The method gives significantly better band structure and band gaps. The big disadvantage of this procedure is the fitting process to find U and the inability to predict band gaps without the knowledge of U.

Another way of improving the band structure is by replacing the exchange-correlation term, which can be seen as the effective potential for the quasiparticles, by a potential developed for describing quasiparticles [60]. In essence, these methods use the idea of a screened Coulomb potential instead of an unscreened Coulomb potential. Popular methods are, for example, HSE (Heyd-Scuseria-Ernzerhof) [61, 62], GW (perturbation theory of the screened potential W) and more recently QSGW (quasiparticle self-consistent GW) [57]. The difference between these methods is the way how this screened potential is incorporated. In HSE this is done within the DFT formalism by using a fitted non-local potential term in the exchange-correlation functional. GW is a fully *ab initio* theory based on Green's functions and it is extended in the recently developed QSGW, which is quite promising.

In that case, the quasiparticle Hamiltonian is given by:

$$(-\frac{\nabla^2}{2} + V_{ext}(\overline{r}) + V_H(\overline{r}))\psi(\overline{r}) + \int \Sigma(\overline{r}, \overline{r'}, E_i)\psi_i(\overline{r'})d\overline{r'} = E_i\psi(\overline{r}) \tag{3.20}$$

In this equation the non-local potential, i.e. the potential the quasiparticle feel, is given by Σ and is called the self energy. In GW this potential is approximated using the DFT eigenvalues, while this is done self-consistently in the QSGW method. A disadvantage of these methods is that they are computationally demanding. It is sometimes more convenient to use the results from different methods that are not *ab initio* but have the same properties, for example DFT+U.

Chapter 4

Ab initio study of $ZGO : Cr^{3+}$

In this chapter the theoretical results for the persistent phosphor $ZGO : Cr^{3+}$ are discussed. Before the actual calculations of interest can be performed, some pre-calculations need to be carried out. These consist of setting the specified input parameters in order to have the desired precision (section 4.1). Afterwards the most stable configuration of the dopant, the chromium atom, in ZGO is examined (section 4.3). As antisite defect are key to particular models for persistent luminescent, different antisite defect configurations are introduced in $ZGO : Cr^{3+}$. Related quantities such as formation and defect energy are extracted to excess their relative stabilities. Subsequently, the band structure and DOS are calculated to extract electronic properties.

4.1 Convergence

To obtain good computational results, the result should have a precision which is suited for the problem. As the precision varies with these two input parameters some convergence criteria have to be set. The two input parameters that set the accuracy and thus the convergence of the results are the cut-off energy and the k point density. These two input parameters are discussed in detail, see chapter 2, where the cut-off energy arises because of the truncation of the expansion for the Kohn-Sham wavefunction

$$u_{n\overline{k}}(\overline{r}) = \sum_{\overline{G}} C_n^{\overline{k}}(\overline{G}) exp(i\overline{G} \cdot \overline{r}) \tag{4.1}$$

$$E_{cut-off} = \frac{\hbar^2 G_{max}^2}{2m_e}. \tag{4.2}$$

The k point density originating from making a dense quantum number discrete (see section 2.3.1) or equivalent by approximating a sum in the reciprocal space by an integral.

To determine an appropriate $\overline{k}$ mesh and cut-off energy the difference in total energy or force are compared when varying one parameter while keeping the second fixed. Such a procedure is done for Ga_2O_3 and ZnO from which the results (force, energy) determine the input parameters are to obtain the desired precision. Afterwards these settings, cut-off energy an k point density, are set for Cr_2O_3 and compared with a higher setting to confirm if the desired accuracy is also here obtained. Instead of doing a convergence test on the more computational demanding ZGO the obtained settings of the basic material (ZnO, Ga_2O_3, Cr_2O_3), that make up ZGO, are used.

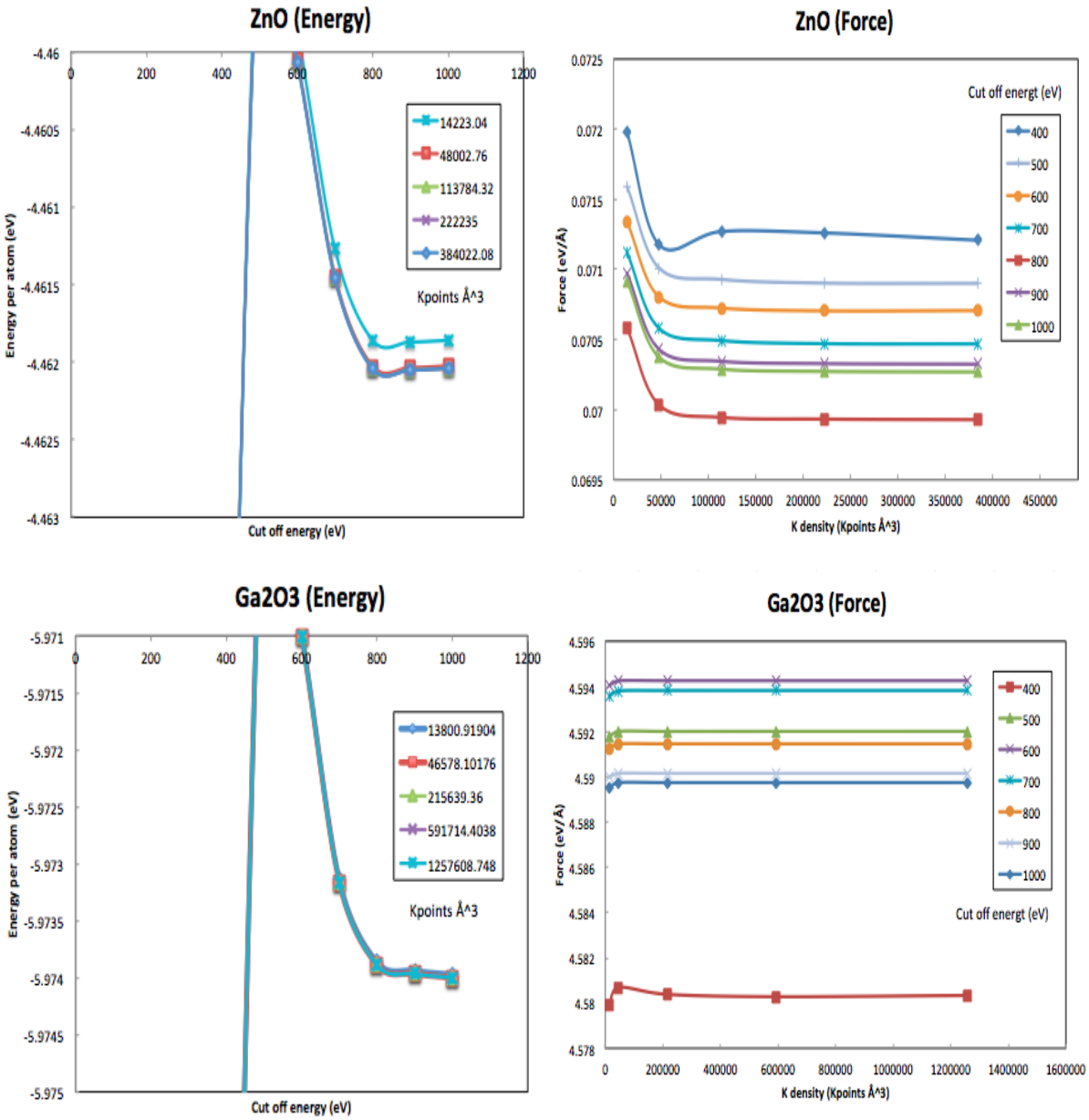

Figure 4.1: Convergence of the average total force (see equation 4.3) and the energy respectively as a function of the k-mesh density (points$\mathring{A}^3$) or cut-off energy (eV).

To determine the $\overline{k}$ mesh, the total average force per atom as a function of the k-mesh density is plotted

$$\overline{\triangle F} = \sqrt{\frac{1}{N}\sum F_x^2 + F_y^2 + F_z^2} \tag{4.3}$$

with N the number of atoms in a unit cell. The force is plotted because the convergence of the $\overline{k}$ point density as a function of the energy per atom does not show much variation. From the curves of the total average force per atom it is seen that there is just a minor dependence of the force on the $\overline{k}$ mesh. We conclude that a density[1] of 70000 $points\mathring{A}^3$ is sufficient to have an error on the total force of less than 1 $meV/\mathring{A}$ (equivalent with less than 1 meV on the total

[1]This is actually the density multiplied by $(2\pi)^3$.

energy) (see Fig. 4.1).

From the energy per atom as a function of the cut-off energy (see Fig. 4.1) a cut-off energy equal to 800 eV is chosen leading to an error of less than 1 $meV/atom$ (equivalent with less than 1 meV on the total energy of the unit cell). The reason we want such a high accuracy is that we will put impurities in our SC. This will be a very low concentration and the effect of it on the pure structure are small. To see these effect a high accuracy per atom is needed. Also the states of the impurities will be very localized and are poorly described by plane waves a high cut-off energy helps to describe these states.

4.2 Structure optimization

The next step is to optimized our materials. This is done by first letting VASP optimize the structure and afterwards a fixed volume optimization is done with a deviation of 96%-104% in steps of 1%. This is done because when VASP is optimizing the volume (and ions, ...) it prefers smaller volumes. This originate from the fact that when reducing the volume in real space, the reciprocal cell increases in volume and during the VASP optimization it hold its basis set. With a smaller volume corresponds a bigger brillouin zone, it therefore appears that a bigger cut-off energy is taken for smaller cells leading to a smaller energy. The opposite happens for increasing the volume of the cell. By doing an optimization with fixed volume this difficulty is avoided. By now fitting an equation of state on the 9 points, the optimized structure of our materials can be deduced (see Fig. 4.2). The final results are summarized in appendix C where we also did a temperature correction.

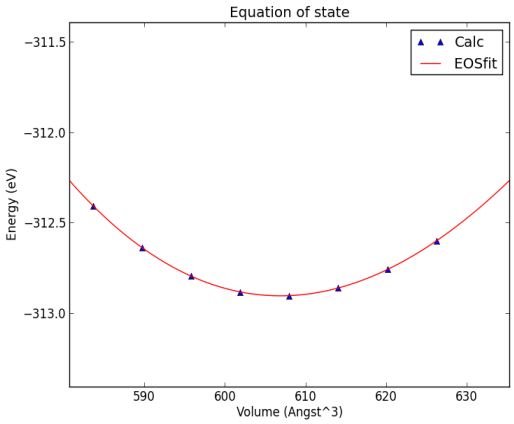

Figure 4.2: Equation of state of $ZnGa_2O_4$ clearly indicating the minimum volume where the structure of the compound is most stable.

4.2.1 Spin optimization

As discussed in the section about SDFT (2.2.1) different spin configuration have to be taken into account when the material can be magnetic. This is the case for the doped materials where the chromium atom, due to its surrounding atoms, can become magnetic, also the case in Cr_2O_3. As there is only one chromium atom replaced in our ZGO unit cell, the problem of different

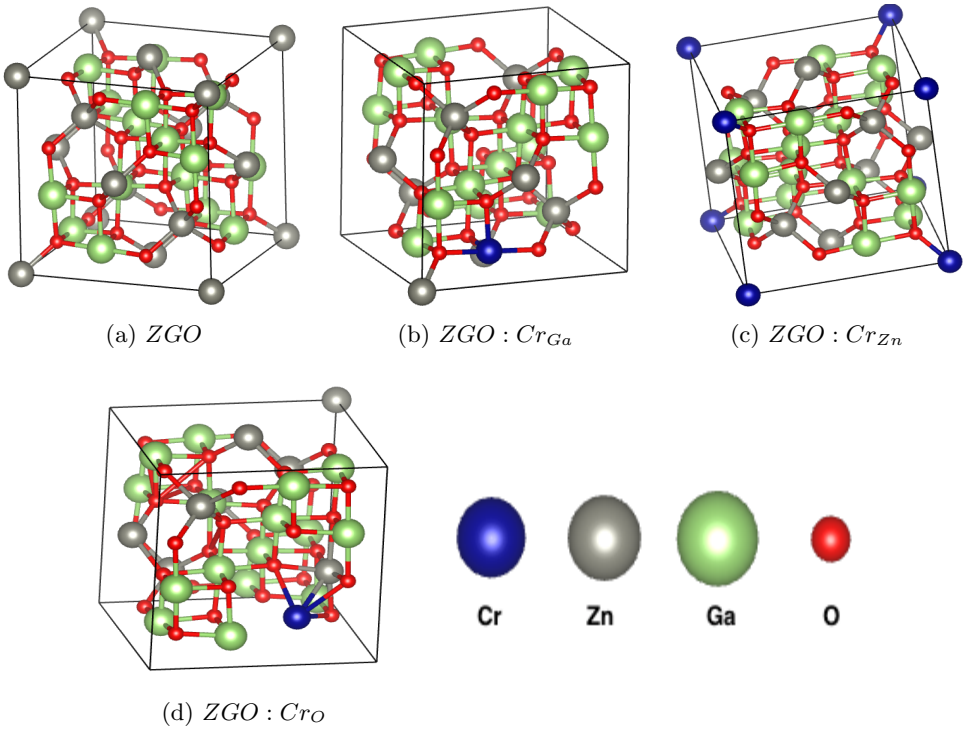

(a) *ZGO* (b) $ZGO : Cr_{Ga}$ (c) $ZGO : Cr_{Zn}$

(d) $ZGO : Cr_O$

Figure 4.3: The optimized structures for host and doped materials.

spin directions on different chromium atom does not occur, this in contrast to the 4 chromium atoms in Cr_2O_3.

In the doped material, different spin configurations on one chromium atom have to checked. Here spin configuration are the numbers of spin up and spin down electrons on the chromium atom. The final energy determines which spin configuration is the most stable. When knowing the most stable spin configuration the procedure of section 4.2 is preformed.

If ZGO is doped with a chromium atom substituted on a gallium site there are 3 electrons of the chromium atom used to make a binding with the surrounding atoms (as gallium is a +III element). As the chromium has the electronic configuration of $[Ar]3d^5 4s^1$. This means that the s orbital will be empty and the chromium atom obtains the $3d^3$ electronic configuration. The possible spin configurations are therefore +-+, +++[2]. When ZGO is doped with a chromium on a zinc site there are only two electrons used in binding with the surrounding atoms (as zinc is a +II element). This means that now the s-orbital is again empty and the d-orbital has a $3d^4$ configurations leading to ++–, +++- and ++++ as possible spin configurations. Finally when ZGO is doped with a chromium atom on an oxygen site there are only two electrons used in binding with the surrounding atoms (as oxygen is a -II element). This means that the s-orbital is fully occupied and therefore the chromium atom has a $3d^6$ configurations leading to the same possible spin configuration as when the chromium is doped on a zinc site ($3d^6$). The different spin configurations for the different dopings is summarized in Table 4.1. From this table we

[2]The default of VASP if MAGMON is not set is putting the electrons in the same spin directions (if possible) on the chromium atom. The optimization of this default is most likely to arise in the +++ configuration on the chromium atom (due to symmetry arguments). The default of VASP can therefore be used to check the electronic configuration of the chromium atom.

conclude that the most stable configuration for all doping configuration is that in which all electrons of the chromium atom are aligned.

		s	p	d	tot (mag.)	energy (eV)
Cr_{Ga}	+ - +	0.017	0.011	1.075	1.102	-318.119
	+ + +	0.023	0.026	2.794	2.842	-319.773
	+ + - -	0	0	0	0	-318.341
Cr_{Zn}	+ + + -	0.016	0.028	2.439	2.483	-318.943
	+ + + +	0.025	0.045	3.412	3.342	-319.909
	+ + - -	0.009	-0.011	0.167	0.165	-306.709
Cr_O	+ + + -	0.043	-0.006	2.340	2.378	-307.487
	+ + + +	0.067	0.035	3.940	4.042	-308.692

Table 4.1: Magnetization of $ZGO : Cr^{3+}$ where the chromium atom is doped on different doping sites as a function of the spin configuration on the chromium atom. The minus and plus symbol represent the number of spin down and spin up electrons on the chromium atom.

In the Cr_2O_3 different chromium atoms are present in its unit cell and it is needed to check the different spin configurations on the four chromium atoms (see Fig. 4.4). These spin configuration consist of three anti ferromagnetic and one ferromagnetic state, saying noting about the spin configuration on one chromium atom but only there direction compared to each other. Again only an optimization of VASP is done for determining which configuration is the most stable. This has to be done for the different spin configuration on one atom but because the magnetic moment on the chromium atom matches the experimental a further optimization on different spin configuration on the chromium atom, by setting the number of spin up and spin down electrons, is not needed[3].

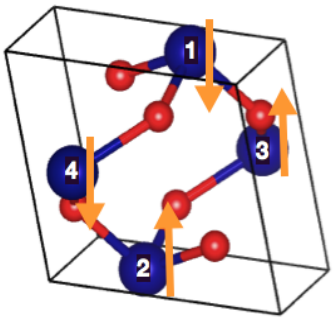

Figure 4.4: Definition of the magnetization of the chromium atoms in Cr_2O_3. The number represents the sequence of plus an minus taken in Table 4.2. The spin configuration that is illustrated is the most stable spin configuration.

[3]VASP maybe has a different spin configuration that has an even lower energy and is thus the most stable configuration, however as this configuration is not the experimental observed this is a fault of the exchange-correlation term and one should stay with the configuration that is experimental observed (not checked). A well known example of this fenomena is Wolfram were the most stable configuration is a $[Xe]4f^{14}5d^46s^2$ and VASP predicts the $[Xe]4f^{14}5d^56s^1$ configurations as most stable.

As there are four chromium atoms in Cr_2O_3 there are four different configurations that need to be checked, the –++, -+-+, -++-, and ++++ summarizes in Table 4.2.

	s	p	d	tot (mag.)	energy (eV)
- - + +	0.017	0.019	2.589	2.626	-86.9912
- + - +	0.017	0.025	2.598	2.640	-87.2741
- + + -	0.017	0.027	2.587	2.631	-87.4930
+ + + +	0.029	0.032	2.841	2.902	-87.0191

Table 4.2: Magnetisation of Cr_2O_3 for one chromium atom. All chromium atoms have the same magnetization. This is in agreement with previous work [28, 29] where the magnetization is equal to 2.76 μ_B. The minus and plus symbol represent the relative orientation of the spin in the different chromium atoms (see Figure 4.4).

4.3 Determining the most stable doped material

In our host material, ZGO, all atoms of the same kind (Zn, O, Ga) are equivalent and therefore doping our unit cell with one chromium atom only leads to 3 different kind of doped ZGO. In this section the most stable dopant position is determined by calculating the formation and defect energy.

4.3.1 Formation energy

In this section the formation energy is calculated for the host and doped materials. The doped materials are ZGO where one atom is replaced by a chromium atom. As all same atoms are equivalent the number of different doped materials is equal to three. The formation energies of these doped solids determine which material is the most stable. E.g. the host unit cell contains 8 units of $ZnGa_2O_4$, the replacement of one atom (Zn, Ga, O) by a chromium atom corresponds to a $Cr_{1/8}$ in $ZnGa_2O_4$ noted as $Cr_xZnGa_{2-x}O_4$ where $x = 1/8$. Compared to experiment this is a relative high doping, however the clustering that happens in experiments due to high doping of chromium atoms is not included in our simulations. The three different doped materials can be written as:

1. For Cr substituted an a Zn atom, Cr_{Zn}: $Cr_xZn_{1-x}Ga_2O_4$
2. For Cr substituted an a Ga atom, Cr_{Ga}: $Cr_xZnGa_{2-x}O_4$
3. For Cr substituted an a O atom, Cr_O: $Cr_xGa_2O_{4-x}$

For calculating the formation energy of these doped material, one can choose two paths. The above structure formulas can be written as a function of the basic material–ZnO, Cr_2O_3 and Ga_2O_3–leading to a formation energy relative them.

$$(1-x)\mathrm{ZnO}+\mathrm{Ga_2O_3}+\frac{1}{2}x\mathrm{Cr_2O_3}-\frac{1}{2}x\mathrm{O} \longrightarrow \mathrm{Cr_xZn_{1-x}Ga_2O_4}$$

$$\mathrm{ZnO}+\left(1-\frac{1}{2}x\right)\mathrm{Ga_2O_3}+\frac{1}{2}x\mathrm{Cr_2O_3} \longrightarrow \mathrm{Cr_xZnGa_{2-x}O_4}$$

$$\mathrm{ZnO}+\mathrm{Ga_2O_3}+\frac{1}{2}x\mathrm{Cr_2O_3}-\frac{5}{2}x\mathrm{O} \longrightarrow \mathrm{Cr_xZnGa_2O_{4-x}}$$

$$\mathrm{ZnO}+\mathrm{Ga_2O_3} \longrightarrow \mathrm{ZnGa_2O_4}.$$

The structural formulas can also be written as a function of the pure solid materials (Cr, Zn, Ga, O). These two paths will give a different results and tell us something about the stability of the pure and basic material relative to the compounds they form[4] . The formation energy out of basic ($\triangle F^b$) and pure ($\triangle F^p$) materials is summarized in Table 4.3. From the formation energy ($\triangle F^b$) it is seen that the host material is the most stable configuration. The second most stable configuration is when the chromium atom is substituted on a gallium site. The difference between the host material and the chromium doped on a gallium site is very small, realizing that this is an energy difference for 7 atoms, the energy difference per atom is smaller than 25meV (the energy available at room temperature). The chromium doped ZGO on a zinc and oxygen site have positive formation energy. On zinc the positive energy is equal to +15 meV/atom which means that even at room temperature it can be formed and a chromium doped ZGO on an oxygen site has a formation energy equal to +198 meV/atom. This lead to the conclusion that the doped material on gallium and zinc site are possible in contrast to the doping on an oxygen site, which is as expected. The formation energy relative to the pure materials ($\triangle F^p$) is

	$\triangle F^b(eV)$	$\triangle F^b(eV)$
ZGO	-0.328	-12.358
$ZGO : Cr^{3+}_{Ga}$	-0.316	-12.389
$ZGO : Cr^{3+}_{Zn}$	0.106	-12.182
$ZGO : Cr^{3+}_{O}$	1.385	-11.260

Table 4.3: Formation energy relative to the experimental used materials (Cr_2O_3, Ga_2O_3, ZnO) given by $\triangle F^b$ and relative to the pure materials (Zn, Ga, Cr) given by $\triangle F^p$. The formation energies $\triangle F^b$ and $\triangle F^p$ are expressed for one chemical unit equivalent to the formation energy of 1/8 of the conventional cell.

seen in Table 4.3. In the case of $\triangle F^p$ all values are negative and there absolute magnitude clearly indicates that the basic materials are more stable than the pure solids. The difference between the two formation energy is that for the formation energy relative to the pure solid materials, both host and chromium doped material are stable. In contrast to the formation energy $\triangle F^b$ where the chromium doped ZGO on the gallium site is the most stable. The difference between host and chromium doped ZGO on the gallium and zinc site is, however, smaller than the energy available at room temperature. Again the doped material on the oxygen site is so high that it is not expected to form. The conclusion from Table 4.3 is that doping on an oxygen site will not be stable and the doping on a zinc and gallium atom are possible.

[4]The accuracy of the formation energy for chromium doped on zinc and oxygen is dependent on the calculated energy of an oxygen solid. This energy is however known to be bad represented by DFT. The accuracy of these formation energies is therefore lower than spoken of in section 4.1.

4.3.2 Dopant energy

The formation energy calculated in section 4.3.1 expresses the amount of energy needed to divide the compound in the basic or pure materials. This quantity does not express how stable a defect is in the host material. In this section this defect is the dopant in ZGO and two quantities are introduced whom are more suited to describe the stability of it. These two quantities are called dopant energy with respect to Cr or Cr_2O_3 and are calculated for the three different dopant positions[5] . The three situation are illustrated in Fig. 4.5. As the chromium atom replaces a bigger atom also the binding distances decreases, however the decrease in band length for the doping on gallium and zinc are respectively 0.45% and 3.43% which is for the first negligible where a small reduction for the second is observed. The doping on the oxygen atom however changes completely and is not worth mentioning as it is already confirmed to be unstable

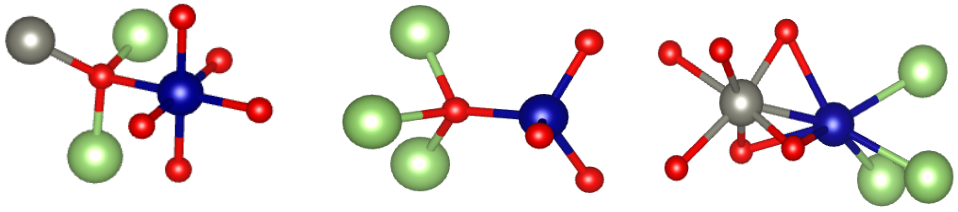

(a) Cr_{Ga} (b) Cr_{Zn} (c) Cr_O

Figure 4.5: Surroundings of chromium on a gallium, zinc or oxygen site.

Cr dopant energy

The dopant energy with respect to clustering of Cr expresses how stable the dopant, the chromium atom is, with respect to clustering of solid chromium around it. This can be calculated by following formulas:

$$E_{Cr}[ZGO : Cr^{3+}_{Zn}] = 8(E[Cr_xZn_{1-x}Ga_2O_4] - E[ZnGa_2O_4] - x(E[Cr] - E[Zn]))$$
$$= 8(\triangle F^p_{Cr_xZn_{1-x}Ga_2O_4} - \triangle F^p_{ZnGa_2O_4}) \quad (4.4)$$
$$E_{Cr}[ZGO : Cr^{3+}_{Ga}] = 8(E[Cr_xZnGa_{2-x}O_4] - E[ZnGa_2O_4] - x(E[Cr] - E[Ga]))$$
$$= 8(\triangle F^p_{Cr_xZnGa_{2-x}O_4} - \triangle F^p_{ZnGa_2O_4}) \quad (4.5)$$
$$E_{Cr}[ZGO : Cr^{3+}_{O}] = 8(E[Cr_xZnGa_2O_{4-x}] - E[ZnGa_2O_4] - x(E[Cr] - E[O]))$$
$$= 8(\triangle F^p_{Cr_xZnGa_2O_{4-x}} - \triangle F^p_{ZnGa_2O_4}) \quad (4.6)$$

and the energies are expressed per dopant or equivalent per 56 atoms in the unit cell[6] of the host material where one dopant is introduced. This dopant energy is equal to the difference between the formation energy out of the pure materials $\triangle F^p$. The dopant energies arising from these formulas is summarized in Table 4.4 where the chromium doped ZGO on the gallium site

[5]The accuracy of the dopant energy for chromium doped on zinc and oxygen is dependent on the calculated energy of an oxygen solid. This energy is however known to be bad represented by DFT. The accuracy of these dopant energy is therefore lower than spoken of in section 4.1.

[6]The multiplication with 8 is because there are 8 units of ZGO in one unit cell where the dopant is introduced.

is stable with respect to chromium clustering. This is in correspondence with Table 4.3 where the chromium doped ZGO on the gallium site is the most stable.

	$E_{Cr}(eV)$	$E_{Cr_2O_3}(eV)$
ZGO	N.A.	N.A.
$ZGO : Cr^{3+}_{Ga}$	-0.248	0.096
$ZGO : Cr^{3+}_{Zn}$	1.408	3.463
$ZGO : Cr^{3+}_{O}$	8.780	13.700

Table 4.4: Cr and Cr_2O_3 dopant energy for doped ZGO with one chromium atom on respectively the zinc, oxygen and gallium site.

Cr_2O_3 dopant energy

The dopant energy with respect to clustering of Cr_2O_3 on the other hand express how stable the dopant, the chromium atom, is to clustering of solid Cr_2O_3 around it. This is calculated by following formulas

$$E_{Cr_2O_3}[ZGO : Cr^{3+}_{Zn}] = 8(E[Cr_xZn_{1-x}Ga_2O_4] - E[ZnGa_2O_4] - x(\frac{1}{2}E[Cr_2O_3] - E[ZnO]) + \frac{x}{2}E[O])$$

$$= 8(\triangle F^b_{Cr_xZn_{1-x}Ga_2O_4} - \triangle F^b_{ZnGa_2O_4}) = 8(\triangle F^p_{Cr_xZn_{1-x}Ga_2O_4} - \triangle F^p_{ZnGa_2O_4}) + 2.064eV \quad (4.7)$$

$$E_{Cr_2O_3}[ZGO : Cr^{3+}_{Ga}] = 8(E[Cr_xZnGa_{2-x}O_4] - E[ZnGa_2O_4] - \frac{x}{2}(E[Cr_2O_3] - E[Ga_2O_3]))$$

$$= 8(\triangle F^b_{Cr_xZnGa_{2-x}O_4} - \triangle F^b_{ZnGa_2O_4}) = 8(\triangle F^p_{Cr_xZnGa_{2-x}O_4} - \triangle F^p_{ZnGa_2O_4}) + 344meV \quad (4.8)$$

$$E_{Cr_2O_3}[ZGO : Cr^{3+}_{O}] = 8(E[Cr_xZnGa_2O_{4-x}] - E[ZnGa_2O_4] - x(\frac{1}{2}E[Cr_2O_3] - E[O]) + \frac{x}{2}E[O])$$

$$= 8(\triangle F^b_{Cr_xZnGa_2O_{4-x}} - \triangle F^b_{ZnGa_2O_4}) = 8(\triangle F^p_{Cr_xZnGa_2O_{4-x}} - \triangle F^p_{ZnGa_2O_4}) + 4.920eV \quad (4.9)$$

again in these formulas the energy is expressed per dopant and is equal to the different of the formation energy out of the basic material $\triangle F^b$. The difference between the previous dopant energy is only a constant and this constant is also indicated in the above formulas. The dopant energies are summarized in Table 4.4 in contrast to the dopant energy with respect to solid chromium clustering only positive energies are obtained, which is in correspondence with Table 4.3 where the doped material are less stable compared to the host material.

The conclusion from Table 4.4 is that doping on an oxygen site will be unstable in correspondence with our conclusion about the formation energy. In contrast to the formation energy here the dopant energy on the zinc site is much higher than that on the gallium site. We conclude that a dopant on the gallium site is stable in contrast to that on a zinc site.

	$E_{gap}^{theory}(eV)$	$E_{gap}^{exp.}(eV)$
ZnO	1.1	3.4 [63, 64, 65]
Cr_2O_3	1.4	4.8 [66]
Ga_2O_3	1.6	4.7 [67]
ZGO	2.3	4.4-5.0 [15]
$ZGO : Cr_{Ga}^{3+}$	2.4	N.A.
$ZGO : Cr_{Zn}^{3+}$	2.3	N.A.
$ZGO : Cr_{O}^{3+}$	0	N.A.

Table 4.5: Comparison of experimental and theoretically calculated band gap for the basic, host and doped material.

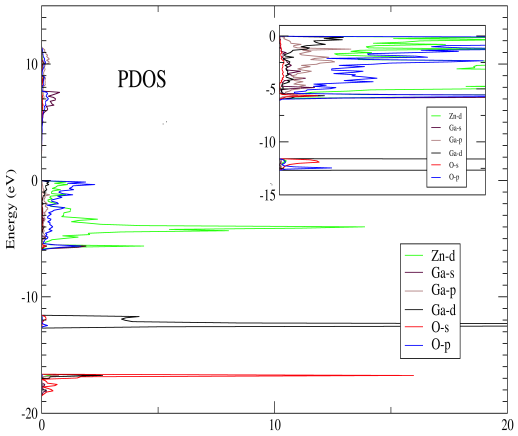

Figure 4.6: The hybridization between Zn-d and O-p is clearly visible and can be linked with the underestimation of the band gap [68].

4.4 Band gap

As discussed in section 3.4.3 the band gap is severely underestimated, using a PBE function, and this is confirmed for the basic and doped material (Table 4.5). The underestimation of the band gap for the host material ZGO is related with the p-d hybridization [68] (see Fig. 4.6) between Zn-d and O-p orbitals. The band gap obtained in [68] for PP1 and PP2 with LDA exchange-correlation term, 2.6eV and 2.82eV, are close to our calculated value. That our band gaps, with a PBE functional, are even lower is because PBE underestimates the bonding length more than LDA, for example 8.4659 (see Table C) compared to 8.2693 [68] for the host material, and therefore a bigger underestimation of the band gaps is derived. However as bad as these band gap are described, energy levels induced by dopant and defects are even more important for persistent luminescent materials as they are used for experimental models to explain there behavior. About these discrete levels no clear under or overestimation is, however known. Relating them to observable experimental quantities will give an idea of their accuracy.

4.5 The host material

In this section the electronic an spectroscopic properties of ZGO are discussed. As the band structure represents surfaces as a function of the reciprocal space, not the entire band structure is displayed. The band structure is therefore displayed along high symmetric lines in the IBZ. The reason that one displays the band structure along these lines is because these lines represent maximums or minimums because there symmetry. The host material has a face-centered cubic (FCC) structure and hence the high symmetry lines corresponds to those in the IBZ of an FCC structure which is a body centered cubic (BCC) weigner cell. These lines are displayed in Fig. 4.7.

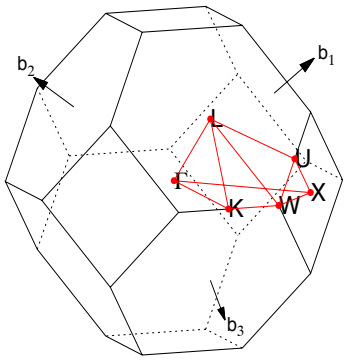

Figure 4.7: Brillouine zone path in a FCC structure [69] along which the band structure is calculated.

The unit cell of ZGO is not a PC; it is the conventional cell and if we calculate the band structure along these lines we obtain the folded band structure[7]. The folded band structure will be a bit more complicated because four times more bands compared to the primitive case are present. To obtain a simpler band structure we make use of an unfolding algorithm (see section 3.3.1). An example of such an unfolded band structure is displayed in Fig. 4.8. Because the host material in the SC has the same symmetry as it in the PC, the unfolded band structure exactly matches the band structure calculated in the PC. The unfolded band structure presented in Fig. 4.8 gives us an idea of the most interesting regions. Because the SC is only four times the primitive the extra bands in the SC band structure are still feasible. The band structure provides more information as the DOS, which can be seen as the average of different bands close to each other. The band structure along the most interesting regions and the corresponding DOS are given in Fig. 4.9. In Fig. 4.10 a band diagram is shown where the band gap, conduction and valence band is indicated and quantified.

4.6 Energy scheme of $ZGO : Cr^{3+}$

After calculating the band structure and DOS of the host material a chromium atom is substituted on a Zn or Ga site and the band structure and DOS are calculated [70][8]. The unfolded

[7] Care has to be taken with the directions (see appendix B).

[8] The doping where the chromium atom is substituted on a oxygen site is a unrealistic case an will therefore be omitted.

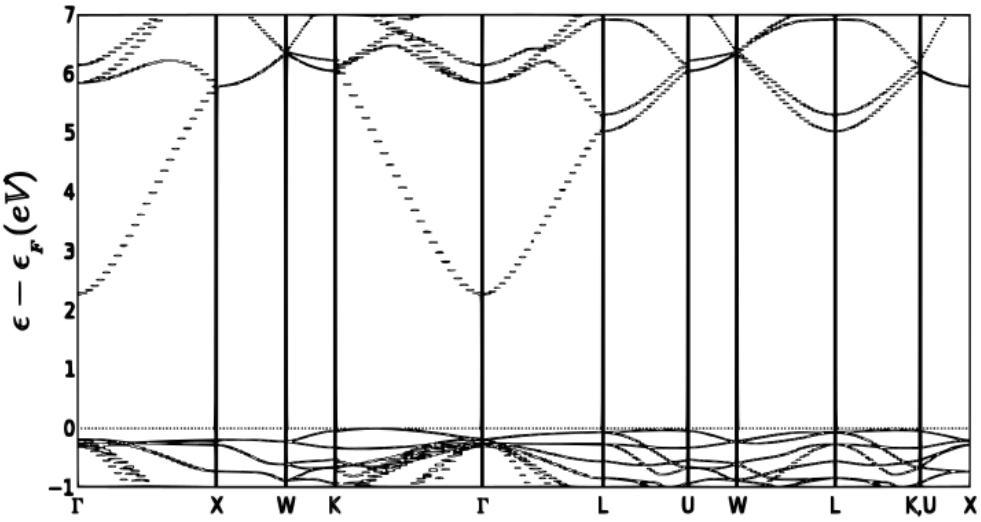

Figure 4.8: Unfolded band structure of a conventional *ZGO* SC. It perfectly matches the band structure of the PC [68].

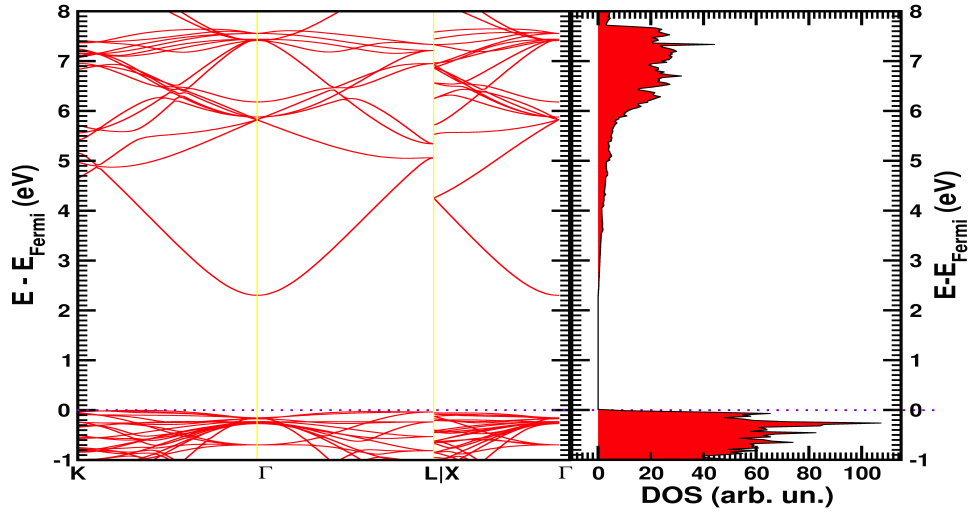

Figure 4.9: Band structure of a conventional *ZGO* SC zoomed in on the interesting regions seen in Fig. 4.8.

band structure is calculated to compare it with the unfolded band structure of the host material. In the DOS and the band structure extra chromium levels will be visible and analyzed.

4.6.1 Chromium levels

The energy states of the chromium atom will look flat in the band structure and this can be explained by the theory of section 2.6.2 where the wave vector can be linked to the phase factor between orbitals centered on different atoms. As the chromium orbitals will be very localized the orbitals will, because of this localization, weakly interact with the orbitals centered on the other atoms. Because of this weak interaction the k value that assigns the phase factor between the orbitals on the chromium atom and the other orbitals will have a small effect on the energy. As the k value does not matter much straight lines are observed in the band structure.

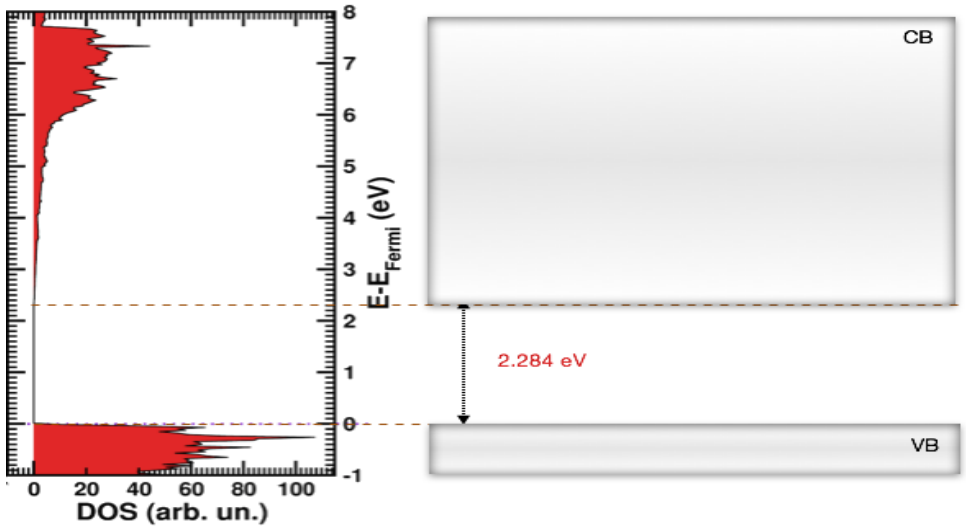

Figure 4.10: Band diagram of *ZGO* SC obtained out of the DOS of ZGO with indication of the band gap.

4.6.2 Splitting of the chromium levels

The wavefunctions calculated by the Kohn-Sham effective potential[9] are calculated out of a single-particle equation and as already explained these single particles can be related to quasi-particles (see section 3.4). The single-particle effective potential is a functional of the density, thereby states that arise from this potential have the splitting related to the symmetry of the density. More particular the d-states of the chromium atom, situated in an octahedral site, will have the splitting of a d^1 configurations for an octahedral field. This because the density will have approximately the octahedral symmetry around the chromium atom an thereby also the effective potential will have this symmetry. The reason the splitting corresponds to a d^1 configuration and not to a d^n configuration is because the states are calculated out of an independent-particle equation, the Kohn-Sham equation[10].

The splitting of d-orbitals are thus determined from an octahedral or tetrahedral like potential dependent on the coordination of the chromium dopant. By only considering the closest neighbors of the chromium atom an approximation up to 4^{th} order, when $|\mathbf{R}_i| \gg \mathbf{r}$, of these potential is given by:

$$V_{O_h} = \sum_{i}^{i=6} \frac{Ze^2}{\mid \mathbf{R}_i - \mathbf{r} \mid} = \frac{6Ze^2}{R} + D(x^4 + y^4 + z^4 - 3/5r^4) \tag{4.10}$$

$$D = \frac{35Ze^2}{4R^5} \tag{4.11}$$

$$V_{T_d} = \sum_{i}^{i=4} \frac{Ze^2}{\mid \mathbf{R}_i - \mathbf{r} \mid} = \frac{4Ze^2}{R} + eTxyz + eD_t(x^4 + y^4 + z^4 - 3/5r^4) \tag{4.12}$$

[9]The effective potential is a functional of the density an thus the single-particle wavefunctions are coupled trough the ground-state density that they generate.

[10]It is dangerous to speak of an independent-particle model because in fact these particles are still coupled to the density.

$$D_t = -\frac{4}{9}D \tag{4.13}$$

$$T = \frac{10\sqrt{3}Ze}{3R^4} \tag{4.14}$$

where $\mathbf{R}_i$ is the position of the i^{th} neighbor of the dopant, $\mathbf{r}$ the position of an electron on the dopant and Z the negative charge of the neighbor (anion surrounding). The value of the splitting is now determined from calculating the expectation values of the d-type orbitals.

The splitting of a d^1 electronic configuration when introduced in a configuration of given symmetry is trivial as there is no need to consider electron repulsion. The d-orbitals have even parity and as the second term in eq. (4.12) has odd parity the expectation value of this term, for the d-orbital, leads to zero. The splitting of octahedral or tetrahedral surrounding can therefore be transformed into each other by replacing D by D_t. We therefore only discuss the octahedral site configuration [11]. The expectation value (first order splitting) of d-states in an octahedral site can now be calculated, given the octahedral perturbation potential (Eq. 4.10), and is given by

$$\langle d_{xy}|V_{Oh}|d_{xy}\rangle = \langle d_{xz}|V_{Oh}|d_{xz}\rangle = \langle d_{yz}|V_{O_h}|d_{yz}\rangle = -4Dq \tag{4.15}$$

called t_{2g} states and

$$\langle d_{x^2-y^2}|V_{Oh}|d_{x^2-y^2}\rangle = \langle d_{z^2}|V_{Oh}|d_{z^2}\rangle = 6Dq \tag{4.16}$$

where

$$q = \frac{2e}{105}\int |R_{3d}|^2 r^4 dr \tag{4.17}$$

are called e_g states. The splitting is understandable when looking at the form of the d-orbitals. The d-orbitals that are raised in energy (when surrounding by anions) are orbitals that are directed towards the (anion) neighbors in contrast to d-orbitals that are lowered in energy (see figure 4.11). It is also seen that this perturbation potential introduces an extra parameter Dq which contains the radial part of the wavefunction that is generally not known[12].

4.6.3 Chromium doped on gallium site

After studying the host material, the host material is doped with one chromium atom. The first doped material is a ZGO host with Ga substituted by the Cr dopant. The electronic properties are calculated in the form of a DOS and band structure. Again, the most simple band structure, by unfolding it to that of the PC, is derived. The doped material has, compared to the host material a reduced symmetry. The algorithm for unfolding takes care of this by averaging out, in order to obtained the same symmetry.

In this doped situation a spin polarized calculations is done and both spin up and spin down unfolded band structures are given in Fig. 4.12 and 4.13. The difference with the host material (see Fig. 4.8) is clearly displayed in the band structure. The extra lines observed in the band structure can only come from the chromium atom situated on the gallium site. The Fermi

[11] The term $(Txyz)$ in the tetrahedral potential can be seen as an perturbation of the octahedral potential. In symmetry groups (see appendix E) the reduction of an irreducible representation of the octahedral symmetry, to the subgroup of a tetrahedral surrounding creates more irreducible representation, but as the expectation value of this extra perturbation term is zero these extra irreducible representation of the tetrahedral complex have the same eigenvalue and stay degenerate. This is an example of accidental degeneracy of irreducible representations.

[12] We already make an approximation by assuming single particle orbitals.

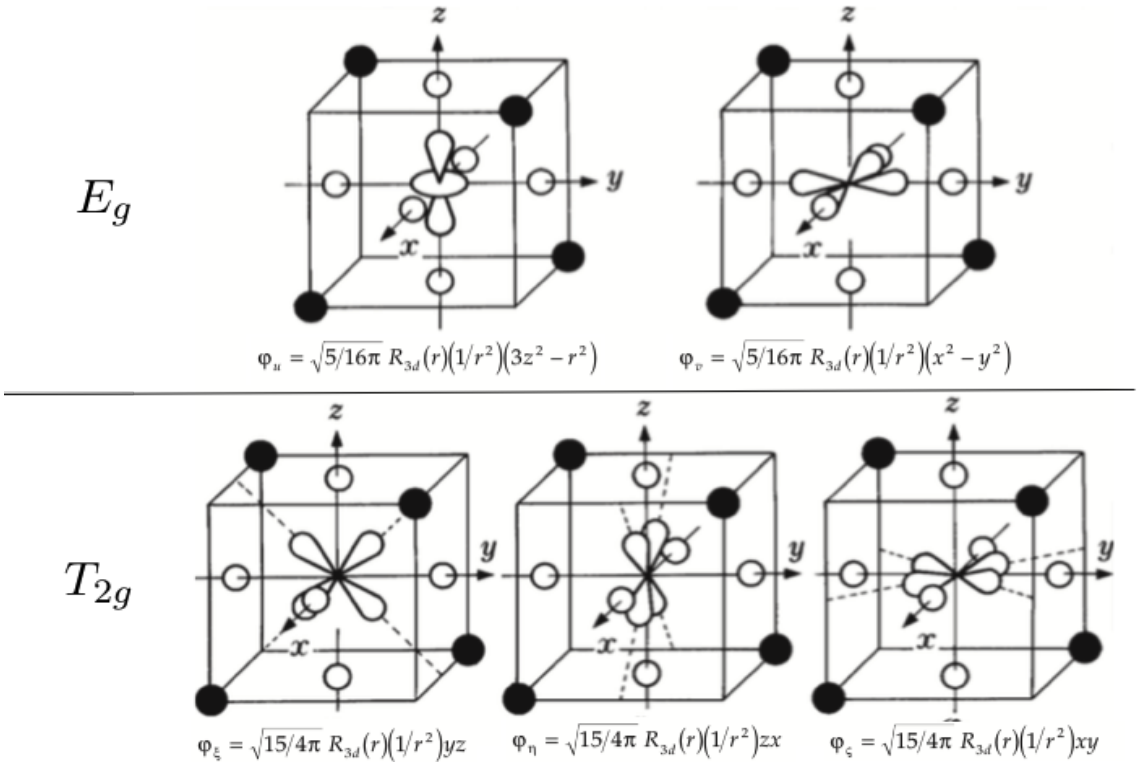

Figure 4.11: The splitting of d-orbital with respect to an octahedral or tetrahedral surrounding. The different splitting of these orbitals is determined by this symmetry and corresponds to a particular irreducible representation (E_g and T_{2g}) see appendixes E for more information about irreducible representation.

level also has shifted to a higher value and is located on a chromium state. The unfolded band structure is used to locate the interesting regions, which afterwards, are shown in the SC band structure (see Fig. 4.14).

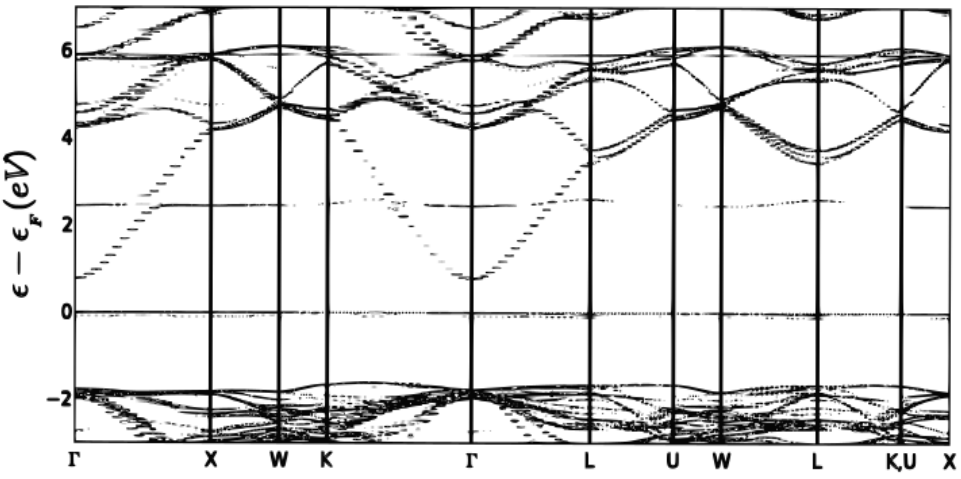

Figure 4.12: Spin down of the unfolded band structure for $ZGO : Cr^{3+}$ in the SC. With the chromium atom on a gallium site.

In Fig. 4.14 a clearly benefit is seen from the band structure compared to the DOS. In the

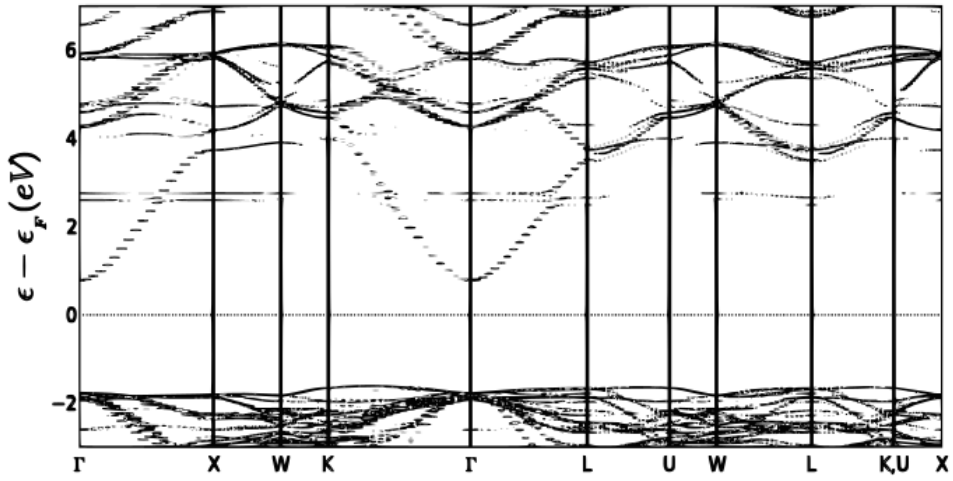

Figure 4.13: Spin up component of the unfolded band structure for $ZGO : Cr^{3+}$ in the SC. With the chromium atom on a gallium site.

band structure the interaction between bands can be seen in contrast to the DOS. In particular, the interaction between conduction band and the chromium levels can be seen. A repulsion between bands indicates that these states have the same symmetry and a crossing of bands means they differ in symmetry.

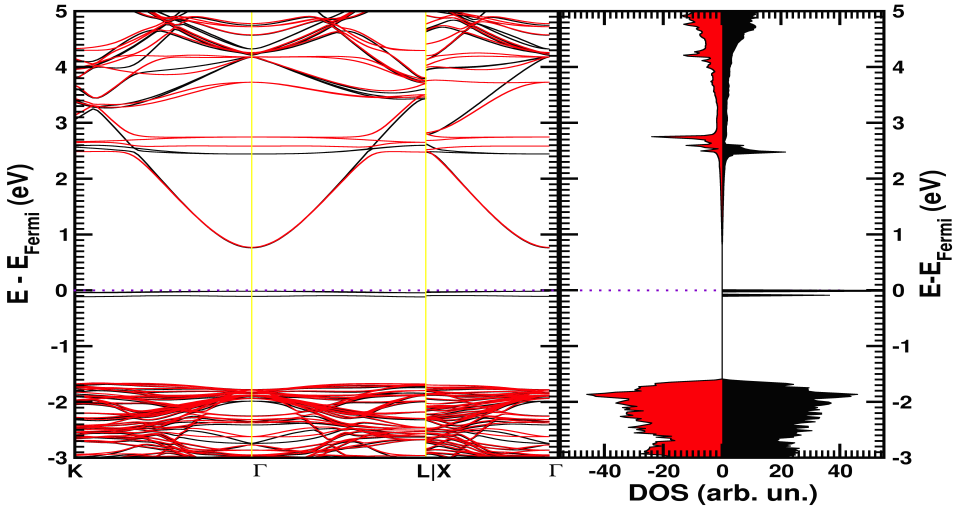

Figure 4.14: Band structure of $ZGO : Cr^{3+}$ in the SC of the interesting parts seen in Fig. 4.12 and 4.13. With the chromium atom on a gallium site.

The peaks in a DOS do not tell us how a band interacts but gives us the discrete levels and their spacing relative to each other. The integrated DOS, that counts the electron, indicates how many electrons can be placed in a peak attributed to a chromium atom. This information is summarized in Figure 4.15 and Table 4.6. As the chromium atom is octahedral coordinated by oxygen atoms the splitting should correspond to the splitting of a d^1 configuration (see section 4.6.2). Indeed it is seen that the DOS contain occupied spin states that has the lower laying t_{2g} states occupied with three electrons and the higher laying e_g states possible to be occupied by

two electrons. The other spin t_{2g} states are located next to the first e_g state and the other spin e_g states are delocalized in the conduction band.

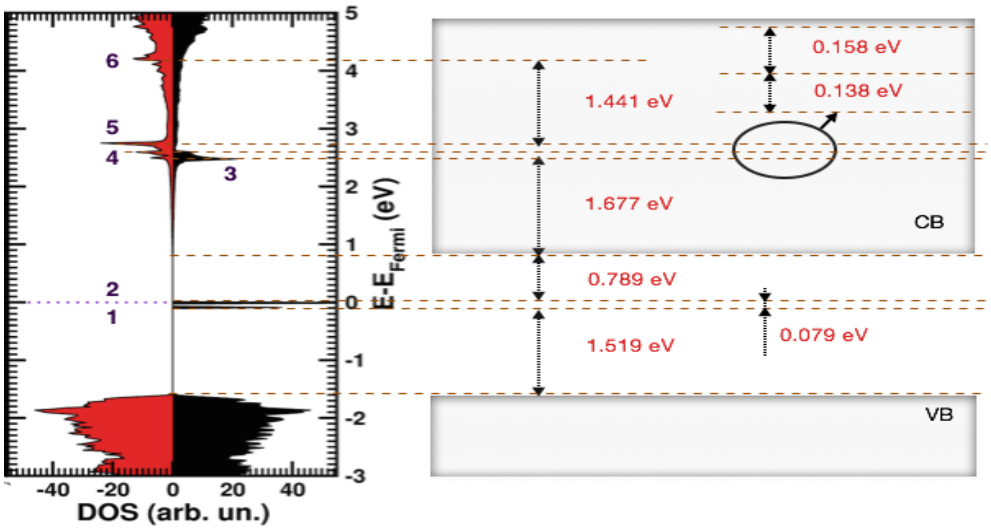

Figure 4.15: Band diagram of $ZGO : Cr^{3+}$. With the chromium atom on a gallium site obtained from the corresponding DOS.

Peak	1	2	3	4	5	6
N_{elec}	1	2	2	1	2	1

Table 4.6: Number of electrons that can be situated in the DOS peaks corresponding to a discrete energy level (see Figure 4.15).

4.6.4 Chromium doped on zinc site

The second most stable chromium doped ZGO is that where the chromium atom is substituted on a zinc site. As before, the unfolded band structure is calculated and displayed for both spin up and down (see Fig. 4.16 and 4.17). Again the chromium levels are clearly visible in the band structure and have a flat band structure. The most interested region are then zoomed in and calculated in the SC (see Fig. 4.18). A clear interaction between the chromium and conduction band is visible in the band structure.

The peaks of chromium states and there relative spacing compared to each other accompanied with the number of electrons than can occupy a peaks in summarized in Fig. 4.19 and Table 4.7. As the chromium atom is tetrahedral coordinated by oxygen atoms the splitting should correspond to the splitting of a d^1 configuration (see section 4.6.2). Indeed it is seen that the DOS indicates a spin state that has the three lower laying e_g states occupied with two electrons and a higher laying t_g state that is occupied by two electrons containing one unoccupied state. The other spin t_{2g} state is located in the conduction band, where also the other e_g states is located with one of its electron delocalized in the conduction band.

From the potential in 4.6.2 it is seen that the ratio of d-orbitals splitting between octahedral an tetrahedral perturbation potential is equal to 4/9 where the ratio obtained out of calculations

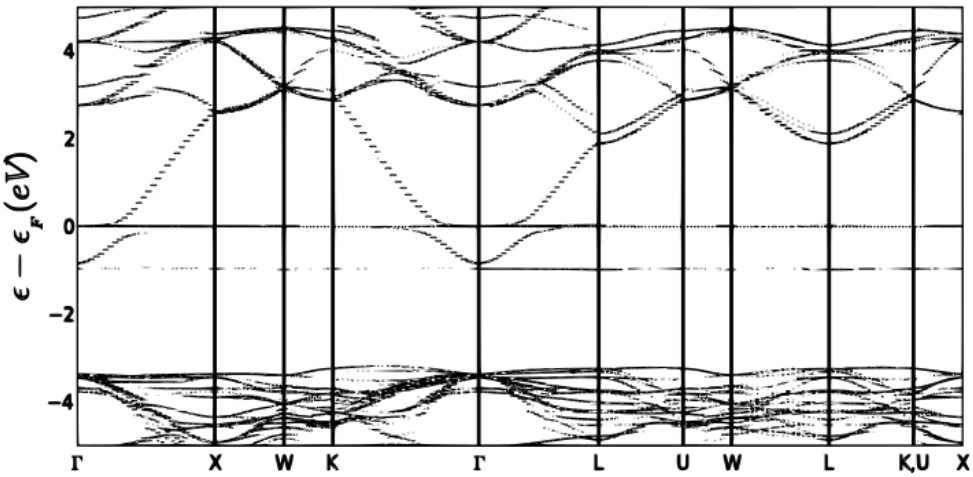

Figure 4.16: Spin up of the unfolded band structure for $ZGO : Cr^{3+}$ in the SC. With the chromium atom on a zinc site.

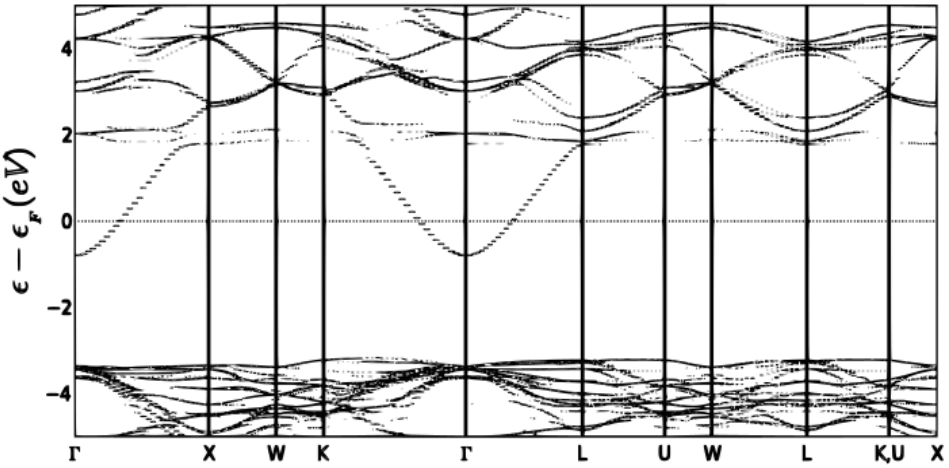

Figure 4.17: Spin down of the unfolded band structure for $ZGO : Cr^{3+}$ in the SC. With the chromium atom on a zinc site.

is equal to $4/9 + 0.057$ indicating the correct splitting, through symmetry arguments, with first neighbors perturbation potential and d-type orbitals as good approximation.

4.7 The doped material with antisite defect

In section 1.4, a well developed model for persistent luminescence was explained that uses the properties of an antisite defect surrounding the chromium atom. An antisite defect is the combination of a gallium on a zinc site noted as Ga^{+}_{Zn} and a zinc on a gallium site noted as Zn^{-}_{Ga}. The minus sign on Zn^{-}_{Ga} site indicates a negative charge because zinc is a +II element located on a +III site. The plus on Ga^{+}_{Zn} indicated a positive charge because a gallium atom is a +III element situated on a +II site. In the section 4.3.2 the chromium defect without antisite defect

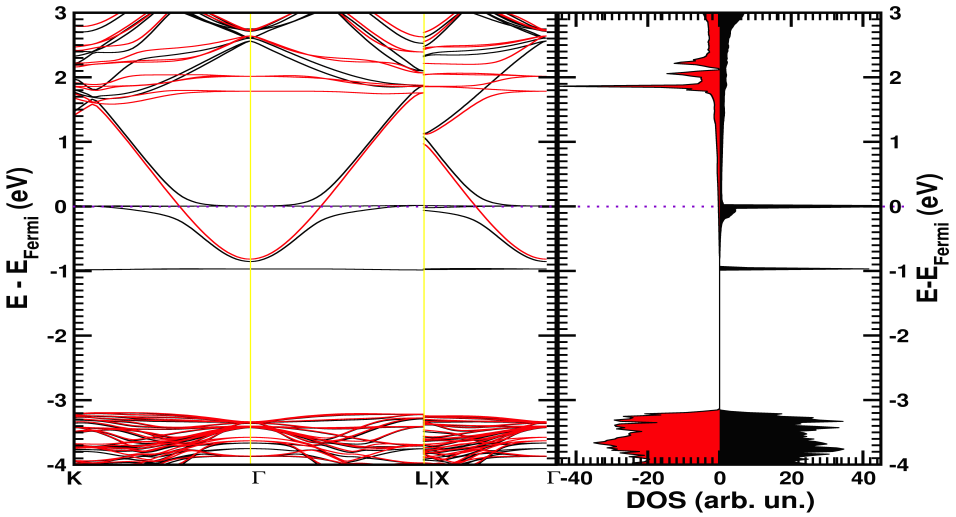

Figure 4.18: Band structure of $ZGO : Cr^{3+}$ in the SC of the interesting parts seen in Fig. 4.16 and 4.17. With the chromium atom on a zinc site.

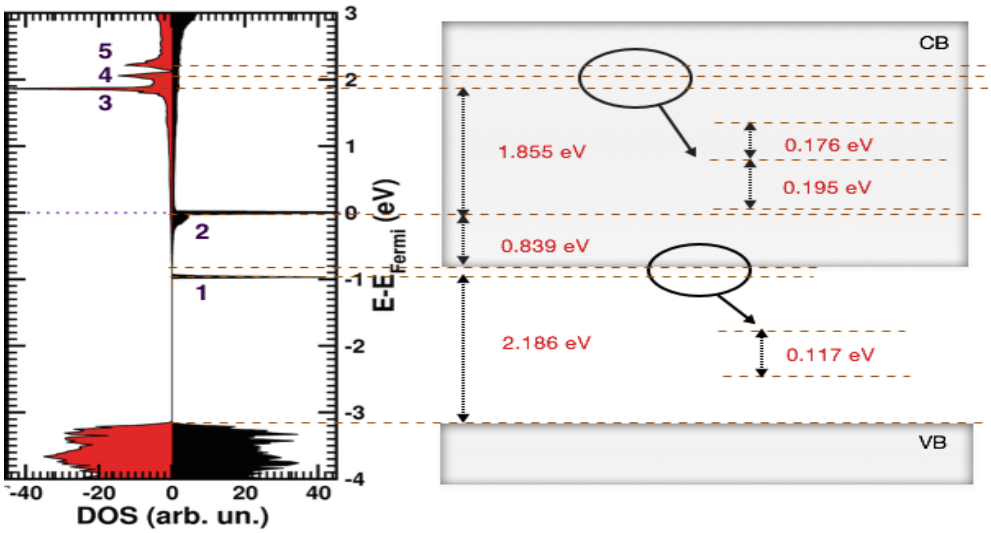

Figure 4.19: Band diagram of the $ZGO : Cr^{3+}$ SC. With the chromium atom on a zinc place obtained from the corresponding DOS.

Peak	1	2	3	4	5
N_{elec}	2	3	2	1	1

Table 4.7: Number of electrons that are situated in the DOS peaks corresponding to a discrete energy level (see Figure 4.19).

was analyzed. Already some relevant properties of the chromium levels where demonstrated in the DOS and band structure. However, how an antisite defect changes these levels need to be further examined. In this section an antisite defect is induced in the two previously discussed doped materials. Introducing an antisite defect will give an idea of the extra levels it induces and its interactions with the chromium atom.

4.7.1 Antisite defect in $ZGO : Cr^{3+}_{Ga}$

The first material where an antisite defect is introduced is the most stable doped material (see 4.3). It is also this doping, a chromium atom on a gallium site, surrounded by a antisite defect that is considered to be the physical observed doped system.

Antisite defect configurations

The possible configuration of an antisite defect is dependent on the shells that the Ga^{+}_{Zn} and Zn^{-}_{Ga} are located, with respect to the chromium, and their distance to each other. The different gallium and zinc shells, where respectively a Zn^{-}_{Ga} and Ga^{-}_{Zn} can be placed, are represented in Fig. 4.20. In this figure the gallium shells are located at distances (before optimization):

- The first shell at a distance of 2.9916$\mathring{A}$
- The second shell at a distance of 5.1831$\mathring{A}$
- The third shell at a distance of 5.9851$\mathring{A}$

here a zinc atom is placed and the zinc shells are at distances

- The first shell at a distance of 3.5038$\mathring{A}$
- The second shell at a distance of 5.4966$\mathring{A}$

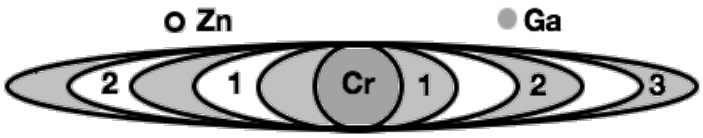

Figure 4.20: Shells of gallium and zinc surrounding the chromium atom where the chromium atom is sitting on a gallium site.

where the gallium atom is placed.

After choosing the shells the distance between the two antisite defect sides is still undetermined. The name of a specific antisite defect configuration is explained in Fig. 4.21. As an example, a 11a antisite defect configuration means that the Ga^{+}_{Zn} antisite defect site is on the first zinc shell and the other antisite defect site, Zn^{-}_{Ga}, is located on the first gallium shell. The letter "a" at the end corresponds to the distance between the two antisite defect sites (alphabetically increasing is a decrease of antisite defect distance)[13].

The different antisite defects are summarized in Table 4.8. The reason why more antisite defect configuration where a Ga^{+}_{Zn} is located on the first shell, is because we expect them to be more stable. This because, by replacing a gallium by a chromium atom a sort of gallium vacancy is created and an extra gallium of the antisite defect in neighborhood of the chromium should be more stable. The structure of the name of an antisite defect configuration also clearly indicates which distances are the same and which changes when comparing two different antisite defect configurations[14].

[13]Note that the "11b" and "11c" are degenerate configuration and all results will be similar.

[14]Care should be taken when comparing the 11 (Ga^{+}_{Zn},Zn^{-}_{Ga}) with configurations (12,13) because in the 11 configuration the Ga^{+}_{Zn} ($\cong 3\mathring{A}$) is situated farther from the chromium atom compared to the Zn^{-}_{Ga}. In all other

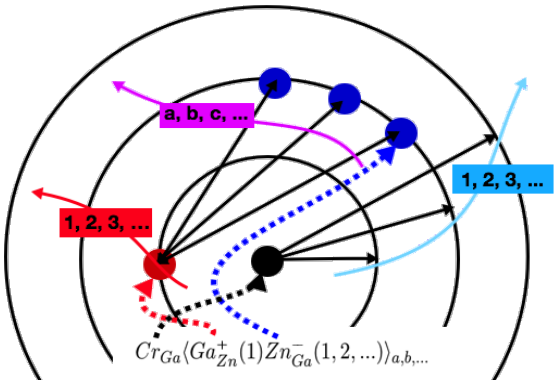

Figure 4.21: Possible configuration of an antisite defect and the explanation its name related to a specific antisite defect configuration.

$Ga_{Zn}Zn_{Ga}$	$d_{Ga_{Zn}-Cr}$	$d_{Zn_{Ga}-Cr}$	$d_{Ga_{Zn}-Zn_{Ga}}$
$11a$	3.50(3.49)	2.99(3.00)	5.49(5.40)
$11b$	3.50(3.48)	2.99(2.96)	3.51(3.55)
$11c$	3.50(3.49)	2.99(3.00)	3.51(3.53)
$12a$	3.50(3.49)	5.18(5.18)	5.50(5.51)
$12b$	3.50(3.51)	5.18(5.19)	3.51(3.54)
$13a$	3.50(3.50)	5.99(5.97)	5.50(5.50)
$13b$	3.50(3.50)	5.99(5.98)	3.51(3.54)
$21a$	5.50(5.49)	2.99(2.99)	5.50(5.51)
$21b$	5.50(5.49)	2.99(2.98)	3.51(3.54)
$23b$	5.50(5.51)	5.99(5.98)	3.51(3.54)

Table 4.8: Different configurations for an antisite defect in a doped ZGO with the chromium atom on the gallium site. Between brackets the optimized distances are given.

Optimized antisite defect configurations

An antisite defect site is optimized by only optimizing the positions of the ions, while keeping the volume fixed. The volume is fixed because when you are working with a low impurity the cell shape and cell volume does not vary a lot and thus are kept constant. In this way you also simulate a lower antisite defect concentration than is introduced in the host SC. The optimized distances are summarized in Table 4.8 and it is seen that the optimized distances are close to the initial distances.

Antisite defect energy

In contrast to the defect energy of section 4.3.2 there are now four different defect energies that are relevant[15]. These four defect energies represent the stability of an antisite defect given by $E_{Anti-Cr}$ in doped ZGO with antisite defect and the stability of the chromium atoms, $E_{Cr-Anti}$ relative to chromium clustering in the doped ZGO with antisite defect. Both defect energies are

configuration the Ga^{+}_{Zn} is located closer than the Zn^{-}_{Ga} ($\cong 3.5\mathring{A}$) antisite defect site.

[15]For the actual values see Appendix D.

calculated through the following equations:

$$E_{Anti-Cr} = 8(E[(CrGaZn)_xZn_{1-x}Ga_{2-2x}O_4] - E[Cr_xZnGa_{2-x}O_4])$$
$$= 8(\triangle F^{p,b}_{(CrGaZn)_xZn_{1-x}Ga_{2-2x}O_4} - \triangle F^{p,b}_{Cr_xZnGa_{2-x}O_4}) \quad (4.18)$$
$$E_{Cr-Anti} = 8(E[(CrGaZn)_xZn_{1-x}Ga_{2-2x}O_4] - (E[(GaZn)_xZn_{1-x}Ga_{2-x}O_4] - E[Ga] + E[Cr]))$$
$$= 8(\triangle F^{p}_{(CrGaZn)_xZn_{1-x}Ga_{2-2x}O_4} - \triangle F^{p}_{(GaZn)_xZn_{1-x}Ga_{2-x}O_4})$$
$$= 8(\triangle F^{b}_{(CrGaZn)_xZn_{1-x}Ga_{2-2x}O_4} - \triangle F^{b}_{(GaZn)_xZn_{1-x}Ga_{2-x}O_4}) - 344meV. \quad (4.19)$$

The defect energy that represent the stability of an antisite defect with respect to the host materials is on the other hand given by

$$E_{Anti} = 8(E[(GaZn)_xZn_{1-x}Ga_{2-x}O_4] - E[ZnGa_2O_4])$$
$$= 8(\triangle F^{p,b}_{(GaZn)_xZn_{1-x}Ga_{2-x}O_4} - \triangle F^{p,b}_{ZnGa_2O_4}). \quad (4.20)$$

The last defect energy is the dopant energy, E_{Cr}, representing the stability against chromium clustering in $ZGO : Cr^{3+}$ (see Eq. 4.5). These four defect energies are related through the following equation

$$E_{Cr-Anti} = E_{Anti-Cr} + E_{Cr} - E_{Anti} \quad (4.21)$$

and are illustrated in Fig. 4.22. As seen from the above formulas all defect energy can be written as a difference of formation energy. Some defect energies have two values because clustering can come from the pure solid chromium metal or form the basic Cr_2O_3. These two kind of defect energies are related through a constant (see also section 4.3.2) and display the same energy trends. The following analyses are thereby only done for defect energy with respect to the pure materials.

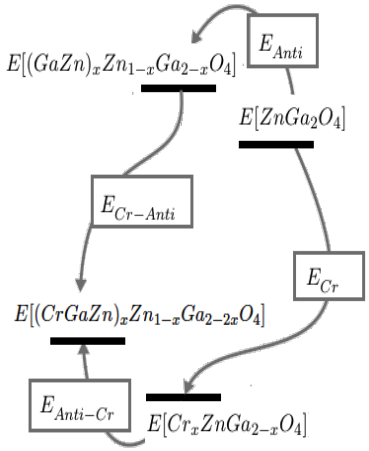

Figure 4.22: Illustrating the defect energies with name and location in a schematic energy diagram. The position of the energy levels illustrates the magnitude and relative orientation compared to the other energy levels (see Eq. (4.5), (4.18), (4.19) and (4.20)) with reference the pure materials.

In Fig. 4.23 (a) the stability of an antisite defect in $ZGO : Cr^{3+}$, $E_{Anti-Cr}$, is shown. The general trend related to the shells is that the antisite defect becomes more stable when it is

moving away from the chromium atom. Related to the distance between the two antisite defect sites it is observed that when it decreases, from $\cong 5.5\mathring{A}$ ("a") to $\cong 3.5\mathring{A}$ ("b"), the antisite defect becomes more stable. In Fig. 4.23 (b), $E_{Cr-Anti}$ illustrates the stability of a chromium atom in $ZGO : Cr^{3+}$ with an antisite defect. The figure shows the same trend related to the shells. The difference with the 4.23 (a) is that the defect energies where only the distance between the antisite defect sites is changed are almost the same, for example the 12a and 12b configurations. The small difference is explained because the energy of antisite defects is almost completely generated from the antisite defect sites configurations and not from the antisite defect orientation relative to the chromium atom. However when calculating $E_{Cr-Anti}$ this energy is subtracted and configurations that only differ in the distance between the antisite defect sites distances have become almost equal in defect energy. A straight line is drawn in Fig. 4.23 (b) for the antisite defect energy, E_{Anti} to clearly indicate this. By drawing this straight line for E_{Anti} it is shown that the antisite defect energy only dependents on the distance between both antisite defect sides, approximately located on the corresponding curves of "a" and "b" configuration. In Fig. 4.23 (b) we also indicated the chromium defect energy, E_{Cr}. It is seen that the stability of the chromium atom is almost completely causing the stability of chromium atom in a ZGO. In both parts of Fig. 4.23 the 21 antisite defect configurations are less stable then the 12 defect configurations. This difference is assigned to the chromium atom with respect to the antisite defect and confirms our reasoning that a Ga^{+}_{Zn} as closest to the chromium atom is more stable than when the Zn^{-}_{Ga} antisite defect site is most closest.

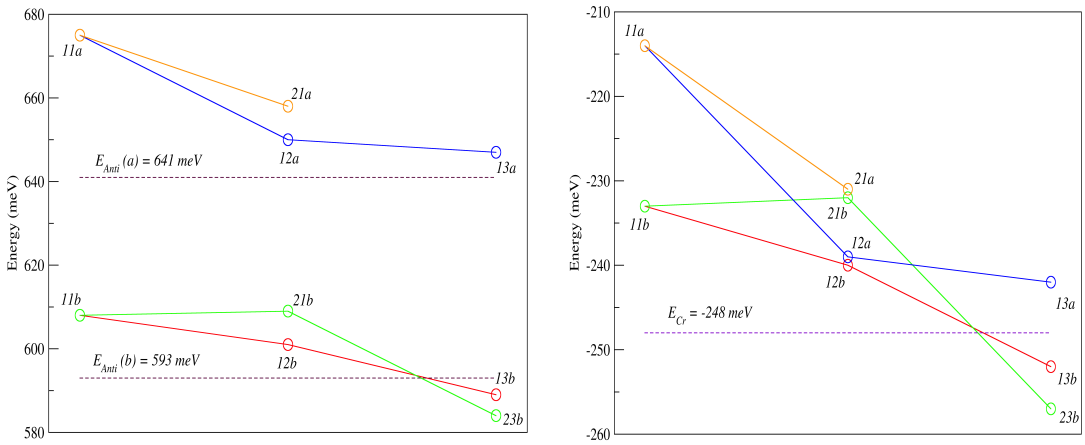

(a) $E_{Anti-Cr}$ (b) $E_{Cr-Anti}$

Figure 4.23: Comparing of $E_{Anti-Cr}$ with $E_{Cr-Anti}$ for different antisite defect configuration in $ZGO : Cr_{Ga}$

To summaries we conclude that the antisite defect is more stable if both antisite defect sites are located far from the chromium atom and the distance between both sites is small. If an antisite defect site is situated in the neighborhood of a chromium atom the configuration where the antisite defect side Ga^{+}_{Zn} is located closest to the chromium atom is more stable. The antisite defect energy, E_{Anti}, is independent on its orientation relative to the chromium atom and is only affected from the distance between both antisite defect sites. This antisite defect energy also causes a energy gap between the "a" and "b" configurations for $E_{Anti-Cr}$. In the same way

the stability of the chromium atom is expressed by $E_{Cr-Anti}$ and is largely determined by the stability of the chromium atom the doped material without antisite defect, E_{Cr}.

Density of states

Next, the DOS of the relevant antisite defect configurations, where the interactions between different states can be seen, are analyzed. The projected DOS (PDOS) is used to confirm from which atoms the peaks in DOS can be assigned to, and the number of electrons that can occupy a peak is indicated below the DOS figures. In all density of states a new band gap compared to $ZGO : Cr$ without antisite defect arises (see Fig. 4.15) that can be assigned to the Zn^{-}_{Ga} antisite defect side.

The first 4 antisite defect configurations that are compared differ in the shell distance of the (Zn^{-}_{Ga}) antisite defect site. This distance is increasing and the antisite defect Ga^{+}_{Zn} is hold fixed where subsequently a large and small distance between the antisite defect is considered (see Fig. 4.24 and 4.25). When the distance between the antisite defect sides is small (see Fig. 4.24): The two figures do not vary a lot, clearly indicating that the distance of the second antisite defect site, Zn^{-}_{Ga}, is not that important if it is increased in the displayed configurations. The chromium states in the middle of the band gap are also not changed compared to the DOS of $ZGO : Cr^{3+}_{Ga}$ and indicate that the interaction between the defect side Ga^{-}_{Zn} is weak. The states in the conduction band displayed in black split compared to the pure doped material (see Fig. 4.15). When the distance between the antisite defect sides is large (see Fig. 4.25): The extra band gap arising from the Zn^{-}_{Ga} are now split in two levels and is attributed to the interaction of the two antisite defect sites. The other features are similar as when the distance between antisite defect sites is large.

In Fig. 4.26 two configurations are shown where, compared to Figure 4.24 and 4.25, the Zn^{-}_{Ga} is placed closest to the chromium atom. The other defect site is also located close to the chromium atom. The difference between the 11a and 11c is that the distance between the antisite defect is decreasing creating the splitting of the band gap state. The chromium state in the middle of the band gap have split in one more state. This splitting can come from the combination of the antisite defect that are located close to the chromium atom or from the interaction of the Zn^{-}_{Ga} with the chromium atom. All other energy levels are also split and every peak has a occupation of one electron (seen in Table 4.11).

To know from witch interaction the mid band chromium states split up the Zn^{-}_{Ga} is located close to the chromium atom and the Ga^{+}_{Zn} is placed on a further distance (see Fig. 4.27). The same splitting is observed and thereby the interaction that causes the mid band chromium levels to split up is caused by the Zn^{-}_{Ga} and that the Ga^{+}_{Zn} antisite defect site thus not induce a strong interaction with the chromium states.

4.7.2 Antisite defect in $ZGO : Cr^{3+}_{Zn}$

The second material where an antisite defect is introduced is the second most stable doping where the chromium atom is substituted on a zinc site. As the instability of this defect, the chromium dopant (see sections 4.3.1), is not that big it can become stabilized when introducing an antisite defect and therefore is interesting to investigate.

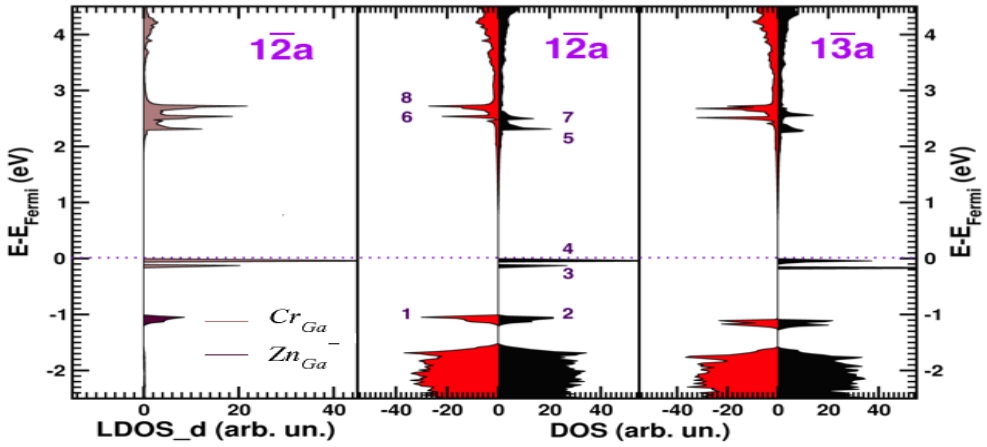

Figure 4.24: The density of state (2 figures at the right) of a chromium doped ZGO on the gallium site for two antisite defect configuration, with large separation between both, where the distance of the Zn_{Ga}^{-} compared to the chromium atom increases. At the left the projected d-orbital density of state is illustrated for the neighboring DOS.

Peak	1	2	3	4	5	6	7	8
N_{elec}	2	2	1	2	1	1	1	2

Table 4.9: Number of electrons that are situated in the DOS peaks corresponding to a discrete energy level (see Fig. 4.24).

Antisite defect configurations

The antisite defect configurations are again determined by the distance to the chromium atom and the distance between the antisite defect sites. The distance of the antisite defect sites to the chromium atom is determined by the possible shells of gallium and zinc where respectively a Zn_{Ga}^{-} and Ga_{Zn}^{+} can be placed are located at distances of[16]

- The first shell at a distance of 3.5400$\mathring{A}$
- The second shell at a distance of 5.5157$\mathring{A}$

for the gallium shell where the Zn_{Ga}^{-} site of the antisite defect is placed and the

- The first shell at a distance of 3.6789$\mathring{A}$
- The second shell at a distance of 5.9966$\mathring{A}$

for the zinc shells where the other part, Ga_{Zn}^{+}, of the antisite defect is situated. These shells are also represented in Fig. 4.28. After choosing a combinations of shells only the distance between two antisite defect sides can be varied. The name of an antisite defect configuration is given in the same way as in section 4.7.1 but now the first number refers to a Zn_{Ga}^{-} antisite defect site, in contrast to section 4.7.1 where the first number corresponds to the Ga_{Zn}^{+} antisite defect site (see Fig. 4.29).

[16] All distance in this section are before optimizing the antisite defect configurations.

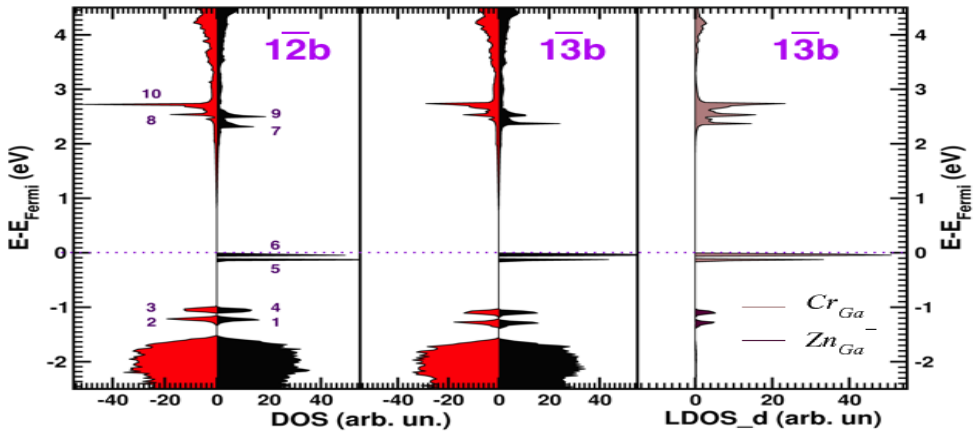

Figure 4.25: The density of state (2 figures at the left) of a chromium doped ZGO on the gallium site for two antisite defect configuration, with small separation between both, where the distance of the Zn_{Ga}^{-} compared to the chromium atom increases. At the right the projected d-orbital density of state per atom is illustrated for the neighboring DOS.

Peak	1	2	3	4	5	6	7	8	9	10
N_{elec}	1	1	1	1	1	2	1	1	1	2

Table 4.10: Number of electrons that are situated in the DOS peaks corresponding to a discrete energy level (see Fig. 4.25).

The big difference between the chromium doped ZGO on a gallium site is that here the chromium atom is placed on a zinc site and thereby a +II zinc atom is replaced by a +III chromium atom. This is the same situation as a zinc replaced by a gallium atom and leads to a positive charge, Cr_{Zn}^{+}, which is also indicated in Fig. 4.29.

The different antisite defect configurations that are chosen are summarized in Table 4.13. It can be seen that more configurations where the first antisite defect site, Zn_{Ga}^{-}, is situating close to the chromium atom are chosen. The reason is that we expect such a configuration to be more stable. The first reason is the same as in section 4.7.1 where by replacing a zinc atom by a chromium atom we have created a kind of zinc vacancy, therefore a close zinc atom is promoted. The second reason is that the chromium has a positive charge (Cr_{Zn}^{+}) and by placing a Zn_{Ga}^{-} antisite defect a compensation of charge is created.

Optimized antisite defect configurations

As in section 4.7.1 only the positions of the atoms are optimized to simulate a lower concentration then that we are actually working with. The distances after optimization are given in Table 4.13 where again it is seen that the distances do not change a lot compared to the initial distances.

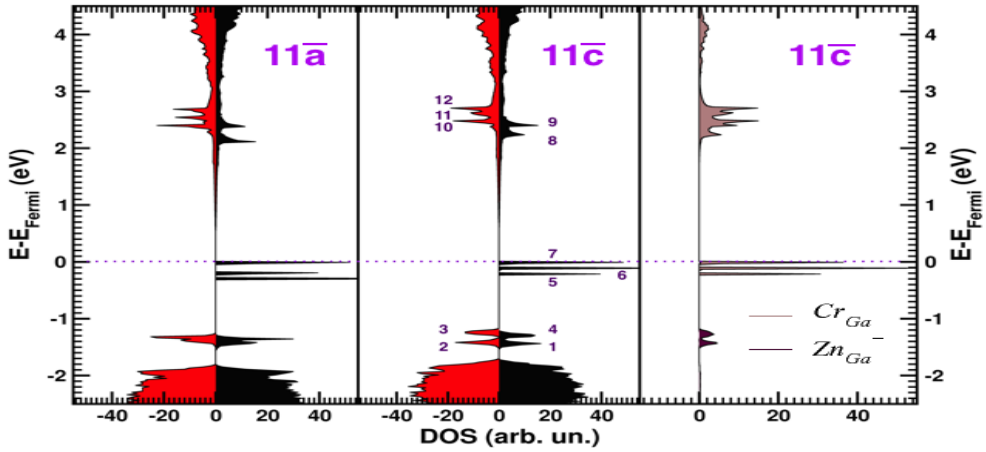

Figure 4.26: The density of state (2 figures at the left) of a chromium doped ZGO on the gallium site for two antisite defect configuration, where both antisite defect are on there first shell surrounding the chromium atom, where only the distance between the antisite defect decreases. At the right the projected d-orbital density of state is illustrated for the neighboring DOS.

Peak	1	2	3	4	5	6	7	8	9	10	11	12
N_{elec}	1	1	1	1	1	1	1	1	1	1	1	1

Table 4.11: Number of electrons that are situated in the DOS peaks corresponding to a discrete energy level (see Fig. 4.26).

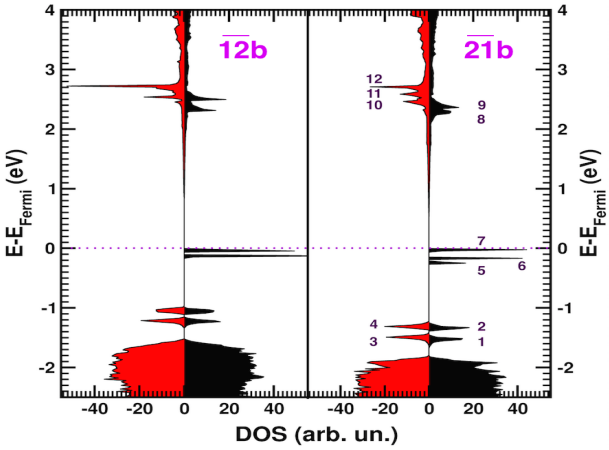

Figure 4.27: The density of state of a chromium doped ZGO on the gallium site for two complementary antisite defect configurations.

Peak	1	2	3	4	5	6	7	8	9	10	11	12
N_{elec}	1	1	1	1	1	1	1	1	1	1	1	1

Table 4.12: Number of electrons that are situated in the DOS peaks corresponding to a discrete energy level (see Fig. 4.27).

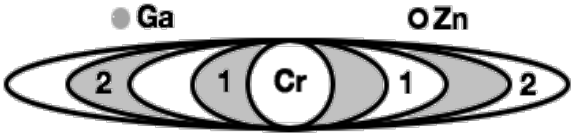

Figure 4.28: Shells of gallium and zinc surrounding the chromium atom where the chromium atom is sitting on a zinc site.

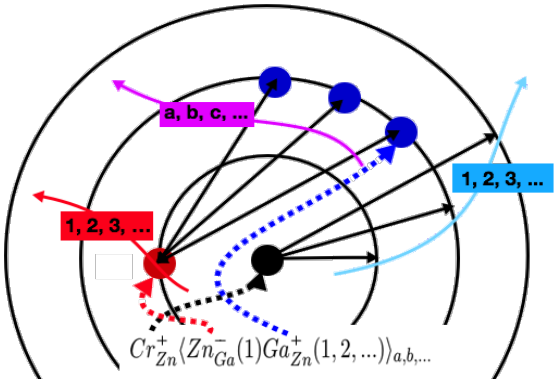

Figure 4.29: Possible configuration of an antisite defect and the explanation its name related to a specific antisite defect configuration.

$Zn_{Ga}Ga_{Zn}$	$d_{Zn_{Ga}-Cr}$	$d_{Ga_{Zn}-Cr}$	$d_{Ga_{Zn}-Zn_{Ga}}$
$11a$	3.54(3.45)	3.68(3.73)	5.50(5.52)
$11b$	3.54(3.44)	3.68(3.68)	3.49(3.54)
$12a$	3.54(3.46)	6.00(5.99)	5.52(5.52)
$12b$	3.54(3.46)	6.00(5.93)	3.51(3.53)
$21a$	5.52(5.52)	3.68(3.65)	5.49(5.51)
$21b$	5.52(5.47)	3.68(3.66)	3.51(3.55)
$22b$	5.52(5.50)	6.00(5.98)	3.51(3.54)

Table 4.13: Different configurations for an antisite defect in a doped ZGO with the chromium atom on the zinc site. Between brackets the optimized distances are given.

Antisite defect Energy

In this section an energy analyze is done with respect to the defect energy[17] for the chromium substituted on a zinc site in the host material. The calculated defect energies are the same as those given in section 4.7.1. The only different defect energies is $E_{Cr-Anti}$ calculated by

$$E_{Cr-Anti} = 8(E[(CrGaZn)_xZn_{1-2x}Ga_{2-x}O_4] - (E[(GaZn)_xZn_{1-x}Ga_{2-x}O_4] - E[Zn] + E[Cr]))$$

$$= 8(\triangle F^{p}_{(CrGaZn)_xZn_{1-2x}Ga_{2-x}O_4} - \triangle F^{p}_{(GaZn)_xZn_{1-x}Ga_{2-x}O_4}) \quad (4.22)$$

$$= 8(\triangle F^{b}_{(CrGaZn)_xZn_{1-2x}Ga_{2-x}O_4} - \triangle F^{b}_{(GaZn)_xZn_{1-x}Ga_{2-x}O_4}) - 2.064eV \quad (4.23)$$

and the dopant energy, E_{Cr}, given by Eq. 4.4. These four defect energies are schematically illustrated in Fig. 4.30. All defect energies are again a difference in formation energy and are

[17] For the actual values see Appendix D.

depended on the reference of pure or basic materials, where both differ by a constant. Further graphs are always of the defect energy with respect to the pure materials.

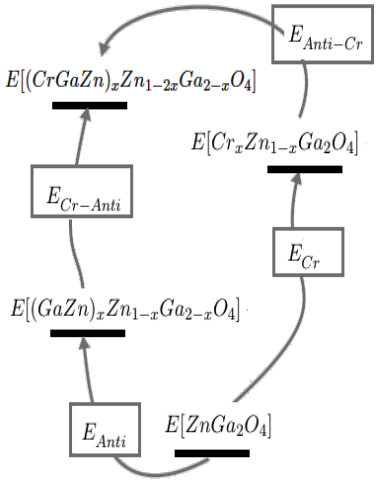

Figure 4.30: Illustrating the defect energies with name and location in a schematic energy diagram. The position of the energy levels is taken such that it illustrate the magnitude and relative orientation compared to the other energy levels (see Eq. (4.4), (4.18), (4.20) and (4.23)) with the pure materials as reference. Eq. (4.21) is also easily deducted from the diagram.

In Fig. 4.31 (a) the stability of an antisite defect in $ZGO : Cr^{3+}$, $E_{Anti-Cr}$, is shown. It looks a little bit uncorrelated but the opposite is true. When the Zn_{Ga}^{-} and Ga_{Zn}^{+} are substituted in different shells (see Fig. 4.28) and the Zn_{Ga}^{-} is located in a closer shell the antisite defect configuration is more stable. The stability analyze as a function of the distance between the antisite defect sites is a bit more subtle. A larger distance between the antisite defect sites is more stable if the configuration corresponds to a Zn_{Ga}^{-} located closer then an, on other shell, Ga_{Zn}^{+} antisite defect site. In other words the most stable configuration as a function of shells (12a configuration compared to the 12b) is more stable when both antisite defect sites are far from each other. A smaller distance between the antisite defect sites is more stable if the configuration corresponds a Ga_{Zn}^{+} located closer, other shell, than the Zn_{Ga}^{-} antisite defect site (21b configuration compared to the 21a). This two phenomena can be explained through charge compensation. When the antisite defect side Zn_{Ga}^{-} is located in a closer shell than the Ga_{Zn}^{-} antisite defect site (most stable shell configuration) the charge of the Cr_{Zn}^{+} is already compensated and to obtain a stable configuration the other antisite defect sites should be located as far as possible. If the shell configuration is reversed (ill placed shell configuration) even more charge around the chromium atom is present and to compensate a Zn_{Ga}^{-} should be located close to the positive antisite defect side (and chromium atom). In contrast to Fig. 4.23 the E_{Anti} is well above the $E_{Anti-Cr}$ indicating a strong stabilization of antisite defect by the chromium atom. In the Fig. 4.23 (b), $E_{Cr-Anti}$ illustrates the stability of a chromium atom in $ZGO : Cr^{3+}$ with an antisite defect. In contrast to the Fig. 4.23 (b) configurations that only differ in distance between the two antisite defect sides are not close to each other. This is related to the strong interaction between chromium atom and the antisite defect. Also the stability of the chromium atom is more stable when the defect is introduced, this is seen because E_{Cr} is higher when no antisite defect is present.

To summarize a prediction about the stability of an antisite defect energy can be made based on 4.31 where we suspect that the Zn_{Ga}^{-} is located closely to the chromium atom to compensate it charge and the other antisite defect site is located farther away. However, because of the extent of the unit cell the number of zinc shells are restricted and our comparison is limited.

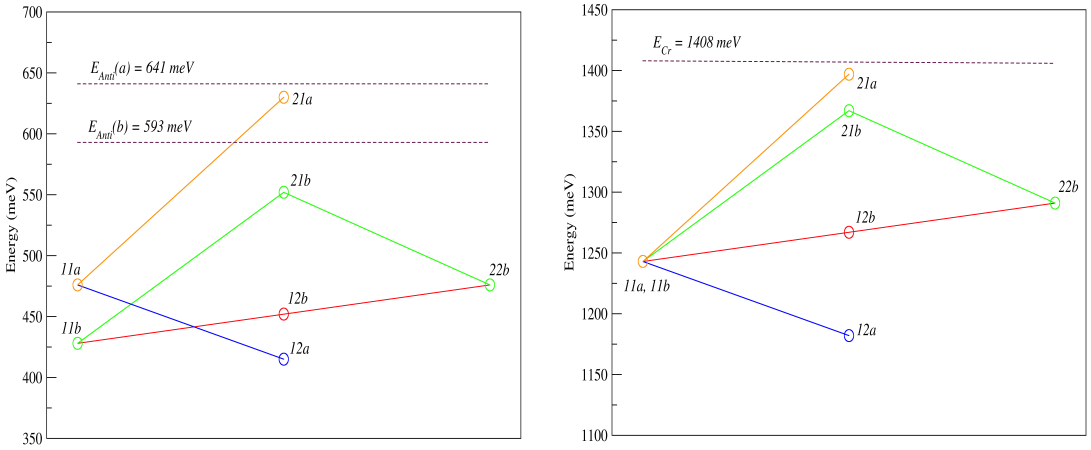

(a) $E_{Anti-Cr}$ (b) $E_{Cr-Anti}$

Figure 4.31: Comparing of $E_{Anti-Cr}$ with $E_{Cr-Anti}$ for different antisite defect configurations in $ZGO : Cr_{Zn}$.

After analyzing the stability of the chromium doped ZGO on a gallium site in section 4.7.1 and the chromium doped ZGO on a zinc site we can compare them as a function of there formation energy. Actually we started this comparison by adding a zinc atom and subtracting a gallium atom where the chromium was doped on a zinc site. This was done to bring it to the same number of gallium and zinc atoms as in a chromium doped ZGO on the gallium site. From this energy we subtracted the energy of a chromium doped ZGO on the gallium site to make it the reference. Summarizing we make it atom like equal as $(CrGaZn)_xZn_{1-x}Ga_{2-2x}O_4$ and subtract $Cr_xZnGa_{2-x}O_4$. This boils down to comparing formation energies as can be seen from the equations below:

$$\begin{aligned} E_{Ga}^{ref} &= E[(CrGaZn)_xZn_{1-x}Ga_{2-2x}O_4] - E[Cr_xZnGa_{2-x}O_4] \\ &= \triangle F^{p,b}_{(CrGaZn)_xZn_{1-x}Ga_{2-2x}O_4} - \triangle F^{p,b}_{Cr_xZnGa_{2-x}O_4} \end{aligned} \tag{4.24}$$

$$\begin{aligned} E_{Zn}^{ref} &= E[(CrGaZn)_xZn_{1-2x}Ga_{2-x}O_4] + E[Zn] - E[Ga] - E[Cr_xZnGa_{2-x}O_4] \\ &= \triangle F^{p}_{(CrGaZn)_xZn_{1-x}Ga_{2-x}O_4} - \triangle F^{p}_{Cr_xZnGa_{2-x}O_4} \end{aligned} \tag{4.25}$$

$$= \triangle F^{b}_{(CrGaZn)_xZn_{1-x}Ga_{2-x}O_4} - \triangle F^{b}_{Cr_xZnGa_{2-x}O_4} - 1.720eV \tag{4.26}$$

where again it makes a difference if the zinc and gallium atoms come from the pure or basic materials. As usual we only give the values if the correcting atoms come from the pure material which only differ with a constant compared to the basic materials.

The comparison between both gives us immediately the formation energy, if the formation energy for a chromium doped ZGO on the gallium site is known, by directly adding this values to the values displayed. The comparison is shown in Fig. 4.32 and displays the same characteristic

as the already discussed defect energies in sections 4.7.1 and 4.7.2. We see that the antisite defect makes both doped material less stable but the difference between different doped material has decreased because the rise in energy of a chromium doped ZGO on the gallium site is larger, $\cong 72meV$, than the rise of a chromium doped ZGO on the zinc site, $\cong 53meV$. Still the chromium doped ZGO on the gallium site is more stable than that of the doping on the zinc site.

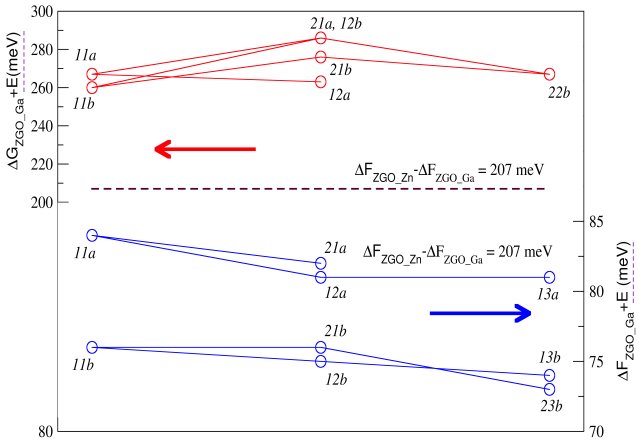

Figure 4.32: Comparing the energy of the chromium doped ZGO with antisite defect on a gallium and zinc site for the different antisite defect configurations and with reference the energy of chromium doped ZGO on the gallium site.

Density of states

Compared to the previous discussed DOS of $ZGO : Cr^{3+}_{Ga}$ in section 4.7.1 the chromium atom, a +III element, replaces a zinc atom, a +II element, thereby induces a charge on the chromium defect noted as Cr^{+}_{Zn} and this induces more interactions. Again band gap states arise from the Zn^{-}_{Ga} antisite defect site just as in 4.7.1. In contrast to the case where the chromium atom is placed on the gallium site, the band gap states are split even if the antisite defect sites are far from each other but where the Zn^{-}_{Ga} is located close to the chromium atom. This can be explained by the different doping where the chromium on a zinc site can be seen as an equivalent gallium on a zinc site. The distance between the two antisite defect sites can be large but the equivalent antisite defect represented by the chromium atom can still be close to the Zn^{-}_{Ga} leading to the splitting.

The first 4 antisite defect configurations that are compared differ in the shell distance of the (Ga^{-}_{Zn}) antisite defect site. This distance is increasing and the antisite defect Zn^{+}_{Ga} is hold fixed, where subsequently a large and small distance between the antisite defect sites is considered (see Fig. 4.33 and 4.34) lead to the same conclusions of section 4.7.1. The only significant difference is the 11b configuration seen in Fig. 4.34 in where the band gap states are split more strongly. This can again be explained by the observation that Cr^{+}_{Zn} behaves as equivalent Ga^{+}_{Zn} defect site. The Cr^{+}_{Zn} and Ga^{+}_{Zn} are now close to the Zn^{-}_{Ga} and cause together the strong splitting.

In Fig. 4.35 we proves again that the interaction between a Zn^{-}_{Ga} and a chromium atom that leads to the splitting of chromium states. As in the 21a configuration there is no negative

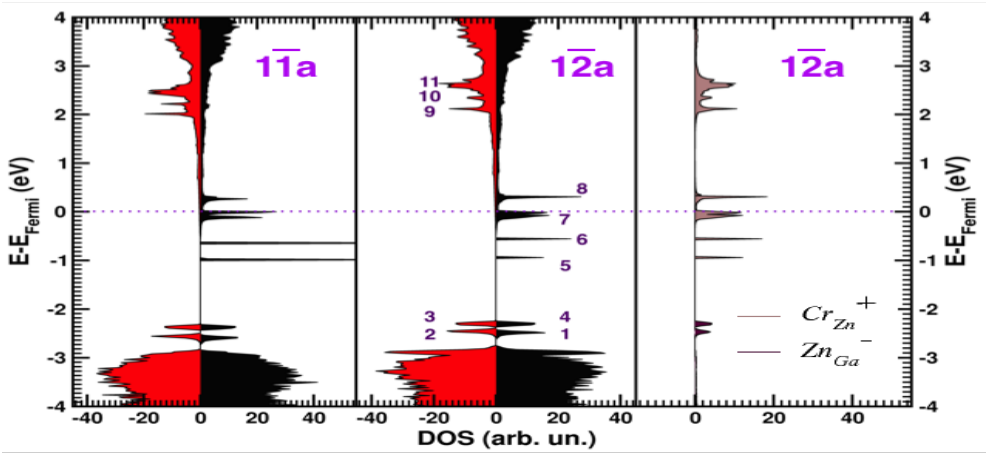

Figure 4.33: The density of state (2 figures at the left) of a chromium doped ZGO on the zinc site for two antisite defect configuration, with large separation between both, and only the distance of the Ga_{Zn}^{+} compared to the chromium atom increases. At the right the projected d-orbital density of state is illustrated for the neighboring DOS.

Peak	1	2	3	4	5	6	7	8	9	10	11
N_{elec}	1	1	1	1	1	1	2	1	1	1	2

Table 4.14: Number of electrons that are situated in the DOS peaks corresponding to a discrete energy level (see Figure 4.33).

charge in the neighborhood of the chromium atom we indeed see that the levels have joined and are more reassemble to the chromium doped ZGO without antisite defect seen in Fig. 4.19.

The density of states of both sections 4.7.1 and 4.7.2 will be used in chapter 6 where we will use it to obtain different excitation band and the influence of an antisite defect on them will be checked.

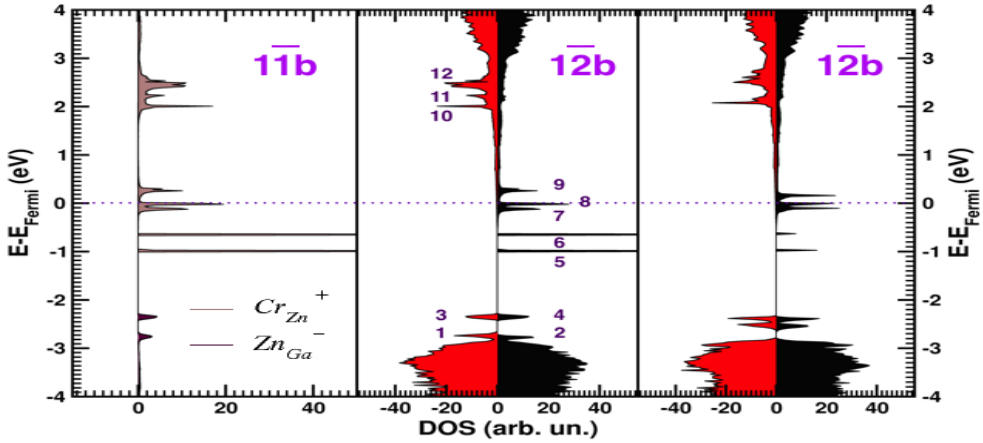

Figure 4.34: The density of state (2 figures at the right) of a chromium doped ZGO on the zinc site for two antisite defect configuration, with small separation between both, where only the distance of the Ga_{Zn}^{+} compared to the chromium atom increases. At the left the projected d-orbital density of state is illustrated for the neighboring DOS.

Peak	1	2	3	4	5	6	7	8	9	10	11	12
N_{elec}	1	1	1	1	1	1	1	1	1	1	1	2

Table 4.15: Number of electrons that are situated in the DOS peaks corresponding to a discrete energy level (see Figure 4.34).

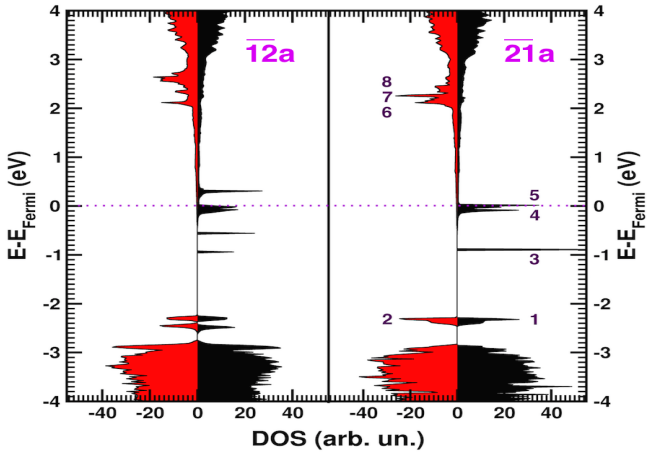

Figure 4.35: The density of state of a chromium doped ZGO on the zinc site for two complementary antisite defect configurations.

Peak	1	2	3	4	5	6	7	8
N_{elec}	2	2	2	1	2	1	1	2

Table 4.16: Number of electrons that are situated in the DOS peaks corresponding to a discrete energy level at the corresponding energy (see Figure 4.35).

Chapter 5

Experiments

In this chapter, the experimental techniques used to analyze the persistent luminescent phosphor, $ZGO : Cr^{3+}$, will be discussed. The persistent phosphor $ZGO : Cr^{3+}$ is synthesized for different dopant concentration. The manufactured samples will be analyzed to confirm that it indeed has the desired composition. The excitation and emission of the doped material will be measured and compared to measurements available from literature. The main underlying thought about these measurements is that we want to be able to use them as comparison for our simulations. The comparison between experimental and theoretical results will be dealt with in chapter 6. It is not the intention of this chapter to fully characterize the synthesized persistent phosphor as already a lot of experimental study is done about this attractive material.

5.1 Materials

In the Fig. 5.1 the materials and their crystal lattice is illustrated. It is from these precursors that the ZGO host material and doped $ZGO : Cr^{3+}$ will be synthesized.

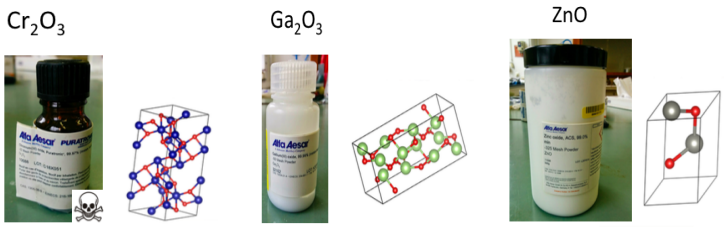

(a) Cr_2O_3 (99.97%) (b) Ga_2O_3 (99.99%) (c) ZnO (99.0%)

Figure 5.1: Precursors for making $ZGO : Cr^{3+}$ with their corresponding purity. All used precursors where supplied by Alfa Aesar.

5.2 Synthesis

Synthesizing the host and doped ZGO is done in four steps [71, 72]. The first step is measuring the different amounts of the precursors. The next step consist of grinding the materials in a mortar to form a homogeneous powder. The grinded powder should be baked in a furnace. The

powder is put in a crucible as illustrated in Figure 5.2 (c) and put in the furnace illustrated in Fig. 5.2 (a,b). The material is then heated to 1400 °C where the temperature is increased linear over 1 hour after which the temperature is sustained over 4 hours. In this way the different species in the powder diffuse and form the end product. This process is called sintering, a process where the material is formed by diffusion. The last step is slight grinding to obtain a homogeneous powder.

(a) Furnace

(b) Cross-section furnace

(c) crucible

Figure 5.2: The furnace where the powder, put in a crucible ,is heated and sintering between the different species appears.

5.3 The samples

Different samples where synthesized following the described method in section 5.2 for different doping concentration of the chromium and zinc. When we speak of doping of chromium and zinc we have to explain how these doping are defined. When we speak of doping of chromium or zinc this is related to the stochiometric formula of $ZGO : Cr^{3+}$[1]

$$\mathrm{Zn_{1+y}(Ga_{1-x}Cr_x)_{2-y}O_4}$$

From this formula the doping of chromium and zinc is defined as:

$$f_{Cr} = \frac{Cr}{Cr + Ga} = x \tag{5.1}$$

$$f_{Zn} = \frac{Zn}{Cr + Ga} = \frac{1+y}{2-y} \tag{5.2}$$

where f_{Cr} is the chromium and f_{Zn} the zinc doping, this last is introduced to create a deficit or a successive amount of zinc atoms in the final $ZGO : Cr^{3+}$. The zinc doping is used to obtain a better stochiometric or to create more defects in the final material [5] this because the unequal sublimation of Ga_2O_3 and ZnO occurs during the synthesis of the material. We denote a material with both doping concentrations as the couple (x%,y%)

In order to calculate the necessary amount of different precursors we us:

$$\mathrm{Zn_{1+y}(Ga_{1-x}Cr_x)_{2-y}O_4} \longrightarrow (1+y)\mathrm{ZnO} + (1-x)\frac{2-y}{2}\mathrm{Ga_2O_3} + x\frac{2-y}{2}\mathrm{Cr_2O_3} + \frac{1}{4}y\mathrm{O_2}.$$

[1] This formula is written as if the chromium would be occupying a gallium site.

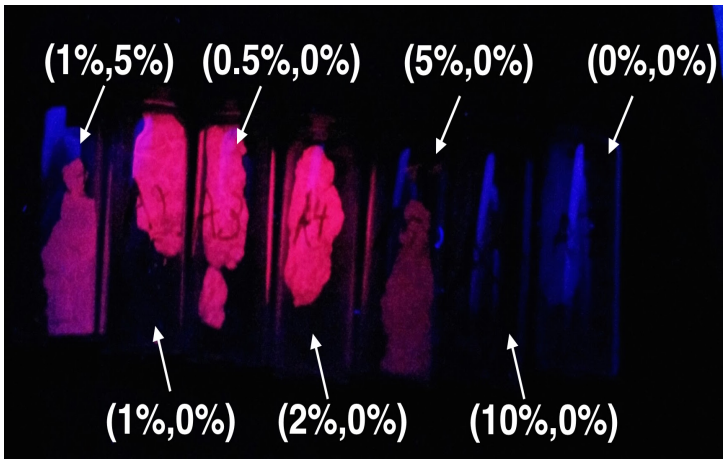

Figure 5.3: Luminescent of the synthesized materials corresponding with there introduced notation.

Firstly, we made a sample with (1%,+5%) as composition. It is said that the excess of zinc leads to more defects. These extra defects are caused by the sublimation of more Ga_2O_3 than ZnO creating more Zn_{Ga}^{-} defects. However because in this thesis we are not concern in making the best persistent phosphor we leave the excess of zinc and further samples are synthesized starting with a stochiometric mixture.

The samples we made have doping concentrations equal to (0%,0%), (0.5%,0%), (1%,0%), (2%,0%), (5%,0%) and (10%,0%) and there luminescent is illustrated in Fig. 5.3. We see that if the doping of chromium is above and equal to 5% no more afterglow is observed.

5.4 X-ray diffraction pattern

An X-ray diffraction pattern (XRD) is measured to check if the sample has the correct crystal structure. XRD is a technique that allows us to see Bragg reflections. These Bragg reflections are measured by scanning along the inclination angle of the X-ray source. By measuring one obtains a graph as function of the inclination angle containing different peaks (see Fig. 5.4). In the case of a powder all crystallographic planes are equally present, the intensities are only dependent on the atomic densities. The ratio of different peaks tells us from which plane the peaks are related and the visible peaks represent the symmetry of the powder.

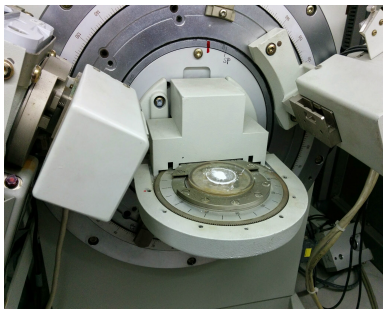

Figure 5.4: Experimental setup for measuring an XRD pattern

5.4.1 XRD pattern in reciprocal space formulation

With the use of reciprocal space (see appendix A) we can give a more mathematical description of an XRD spectrum. The intensities of the peaks in an XRD are proportional to

$$F = \int n(\overline{r}) e^{-i\triangle\overline{k}\cdot\overline{r}} dV. \tag{5.3}$$

This expression reflects that the intensity is proportional to the charge density at $\overline{r}$ multiplied with a phase factor. This phase factor is equal to the path difference, $\triangle\overline{k}$, between a wave scattered at the origin and at a location $\overline{r}$.

We can rewrite this equation by writing the density in reciprocal space, this by using the knowledge that the density is periodic with the real lattice translational vector ($\overline{T}$).

$$F = \int n(\overline{r}) e^{-i\triangle\overline{k}\cdot\overline{r}} dV = \int \sum_{\overline{G}} n_{\overline{r}} e^{i\overline{G}\cdot\overline{r}} e^{-i\triangle\overline{k}\cdot\overline{r}} dV = \sum_{\overline{G}} n_{\overline{G}} \int e^{-i\overline{r}\cdot(\triangle\overline{k}-\overline{G})} \tag{5.4}$$

$$F = \sum_{\overline{G}} (2\pi)^3 n_{\overline{G}} \delta(\triangle\overline{k} - \overline{G}) \tag{5.5}$$

From this equation we see that the peaks arise when the difference between incoming and scattered wave is equal to a reciprocal lattice vector.

The dependence on the inclination angle can be seen when rewriting the condition of where the peaks are situated according to

$$\overline{G} = \triangle\overline{k} = \overline{k'} - \overline{k} \tag{5.6}$$

$$\overline{k'}^2 = (\overline{G} + \overline{k})^2. \tag{5.7}$$

We only look at the elastically scattered electrons, this can be done by making the detector only detect electrons with sufficient energy, for example, when one takes this energy a bit lower than the energy of the incident wave. With elastically scattered waves the total energy remains constant, meaning that $\overline{k'}^2 = \overline{k}^2$. This simplifies equation (5.6) to

$$2\overline{k} \cdot \overline{G} = \overline{G}^2. \tag{5.8}$$

In this last equation we changed $\overline{G}$ to $-\overline{G}$ as it is also a reciprocal lattice vector. This last equations gives us the tools to understand a XRD plot as a function of the scattering angle. In a conventional cell (a cubic cell) the distance between net planes in the crystal is given by $d_{hkl} = 2\pi n/|\overline{G}|$ where (hkl) are the reduced miller indexes of that plane and n is the reducing factor, for example, a (333) planes is equivalent to n=3 and (hkl) = (111). In a conventional cell one can show that the reciprocal lattice vectors $\overline{G}$ are orthogonal to the (hkl) plane ($\overline{G} \perp (hkl)$). These two relations together with equation (5.8) give us (for information about the angle see Fig. 5.5), the so called Braggs law

$$2\overline{k} \cdot \overline{G} = 2|\overline{k}||\overline{G}|sin(\theta) = \overline{G}^2 \tag{5.9}$$

$$2\frac{2\pi}{\lambda} sin(\theta) = \overline{G} = \frac{2\pi n}{d_{hkl}} \tag{5.10}$$

and this equation explains the XRD spectrum.

$$2d_{hkl} sin(\theta) = n\lambda \tag{5.11}$$

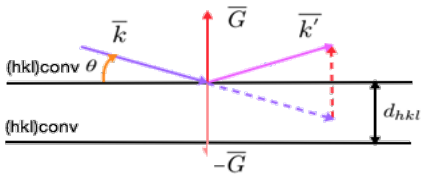

Figure 5.5: Plane waves scattering from crystallographic planes

5.4.2 XRD pattern of the samples

We measured the XRD pattern of our samples to see if the ZGO was indeed formed. In figure 5.6 we see the XRD pattern for two samples. For the sample corresponding to a doping of (1%,0%) (first made) the XRD pattern is the same as found in literature[71, 18, 17, 13], the rest of our samples have a similar XRD pattern. For the second sample (doping (1%,5%)) extra peaks are visible in the XRD pattern. These extra lines are explained by the fact that not all starting material was removed.

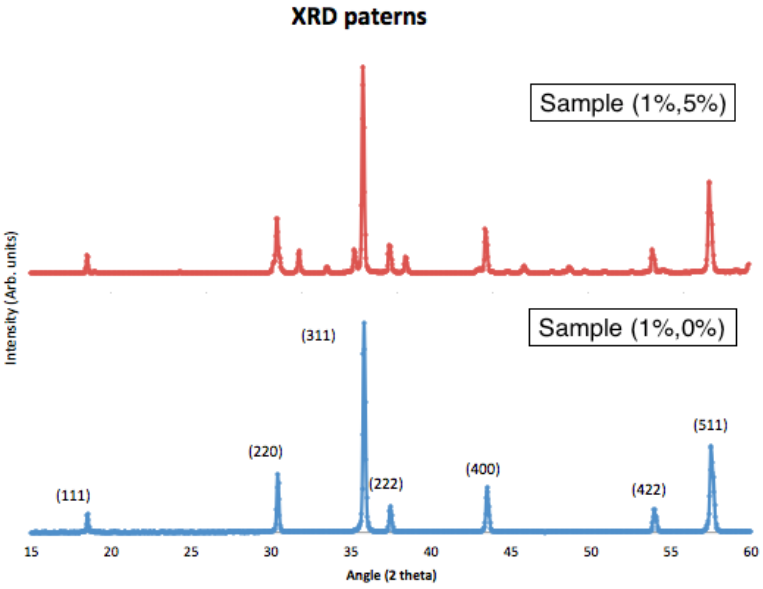

Figure 5.6: XRD patterns

The peaks in the XRD for the (1%,0%) and the other sample signalize a FCC structure compatibel with the structure of ZGO. This can be quickly seen because only peaks of planes with all even or all odd miller indexes appear. This is in correspondance with the extinction rules for an FCC structure (see Eq. (B.9 in appendix B). The ratio of the peaks tells us that the material under study is ZGO.

5.5 Quantum efficiency (QE)

A useful quantity of a luminescent material is its quantum efficiency. There are two quantum efficiency's: internal and external. Internal quantum efficiency is defined as the ratio of photons

that is emitted, the emission, divided by the number of absorbed photons. This can be calculated by first placing a non absorbing and reflecting material in the integrating sphere (152 mm diameter), coated with Spectralon (see [73]) and measuring the total (reflected) intensity (see Fig. 5.8). By now placing our phosphor, that absorbs the photons, in the sphere we can calculated the amount of absorbed photons and with it the internal quantum efficiency (see also Fig. 5.7). The external quantum efficiency compared to the internal gives a measure for how much of the indecent :) photon give rise to emission. The amount of photons that are emitted can be calculated out of the emission of the material (see Fig. 5.7). This number is than divided by the numbers of incident photons leading to the the external quantum efficiency.

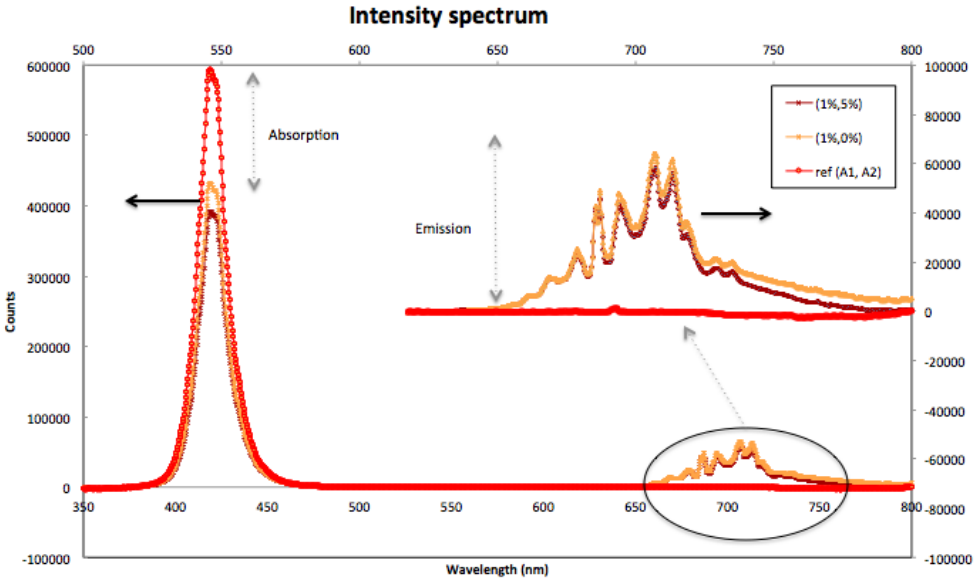

Figure 5.7: Measuring the quantum efficiency of $ZGO : Cr^{3+}$

5.5.1 Measured QE

As already mentioned the intensities are measured inside an integrating sphere (see Fig. 5.8). The measured internal and external quantum are given in Table 5.1. No more luminescence is observed for a higher chromium doping concentration of 5%.

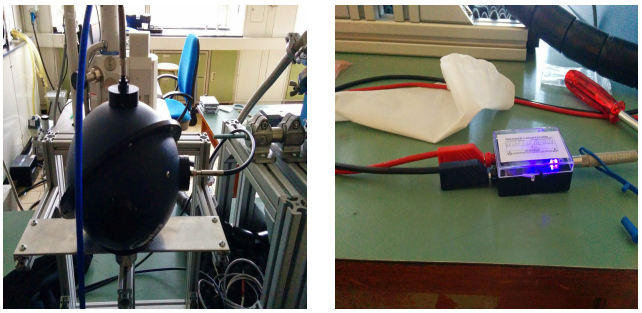

(a) Integrating sphere (b) UV-Led

Figure 5.8: Experimental set-up for measuring $ZGO : Cr^{3+}$

	(1%,5%)	(1%,0%)	(0.5%,0%)	(2%,0%)	(5%,0%)
$QEi = N_{em}/N_{abs}$	0.54	0.78	0.58	0.58	0.053
$QEe = N_{em}/N_{in}$	0.18	0.21	0.17	0.27	0.030

Table 5.1: Quantum efficiency of $ZGO : Cr^{3+}$

5.6 Excitation and Emission

It is well known that chromium dopants in ZGO is substituted on a Ga site [4]. This gallium atom is surrounded by oxygen atoms in a octahedral way. The splitting of a chromium atom can be explained by the use of crystal field theory (see chapter 6, 6.1). The splitting of these levels is depended on the surroundings of the chromium atom (octahedral) and is sensitive to distortions from the surrounding atoms. In reality, in a solid, there are always distortions which reduce the symmetry and thereby split the energy levels of a chromium atom even further.

The energy levels of chromium will be visible by their energy difference, observed in emission and excitation scan (see next section) and compared to literature. Not all transitions are visible in an excitation and emission scan because some levels are not able to decay into each other (forbidden transition). It has to be said however that forbidden transition are only forbidden if they have a specific symmetry and as in a real solid this will always just be an approximated symmetry a lot of forbidden transitions are also visible.

5.6.1 Experimental setup

The experimental setup for measuring an emission or excitation scan is illustrated in Fig. 5.9 (Edinburgh Instruments FS920). Excitation and emission spectra are measured separately. In an emission scan the excitation wavelength is fixed. So you should already have an idea what a good emission is for the material under examination. The excitation wavelength is set with a monochromator and it is responsible for exciting the persistent phosphor. The emission of the persistent phosphor is then measured by scanning all wavelength in a given range with the use of an other monochromator at the detector side. It is important to make sure that the excitation wavelength that is reflected and could harm the detector does not end up in it and therefore a filter should be placed between detector and sample. In an excitation scan the emission wavelength is fixed. The procedure of the emission scan is reversed. As the emission wavelength is now fixed, by a fixed monochromator, you should have an idea of the emission wavelength.

5.6.2 Excitation spectrum

In this section we present such an excitation scan for different emission wavelength (see Fig; 5.10). In this Figure there are three excitation bands visible. These excitation can be related to the excited states of chromium in an octahedral complex. A similar excitation scan is done in [17] and these excitation bands are then related to the excitation of the ground-state of the chromium atom ($^4A_2$) to the excited states $^4T_2$, $^4T_1$ and $^4T_1$, in order of increasing excitation frequency (see chapter 6, section 6.1.3). The last band in Fig. 5.10 is composed by the excitation of chromium from the ground state $^4A_2$ to the excitation state $^1T_1$ and a charge transfer band.

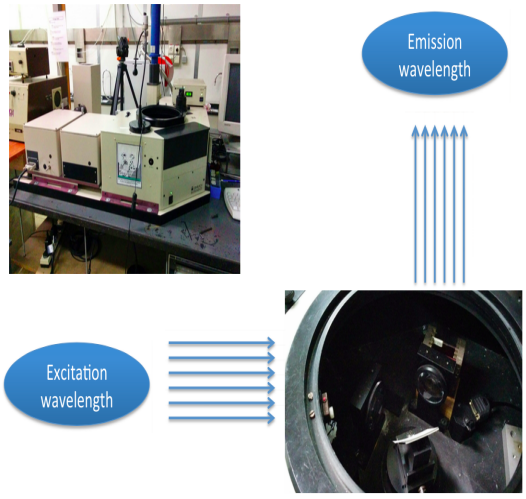

Figure 5.9: Experimental set-up for measuring the excitation and emission spectrum

With charge transfer we mean that an electron is excited from the surrounding anions to an unoccupied excitation level of the chromium emission center (see also 6).

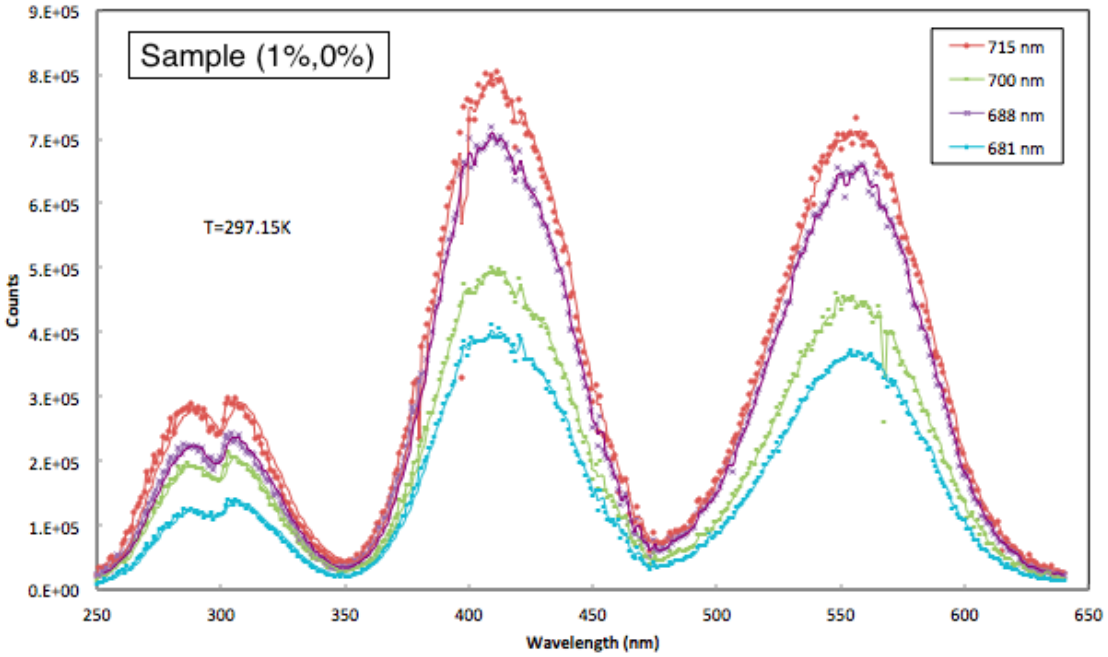

Figure 5.10: Measured excitation scans for different emission wavelength. The excitation spectrum clearly indicating three different excitation bands.

5.6.3 Emission spectrum

The emission scan is done as described and seen in Fig. 5.11. The emission is almost completely similar to the emission pattern obtained in [17]. We have correspondingly labeled the different peaks of the emission spectrum corresponding to this paper. The N2 peak indicates the emission of a chromium atom surrounded by an anti defect. The R peak is that of a pure chromium atom

where the chromium atom is located on a gallium site. The PSB labels mark the beginning of phonon side bands arising from excitation between two electronic state with different vibration an rotational eigenstates.

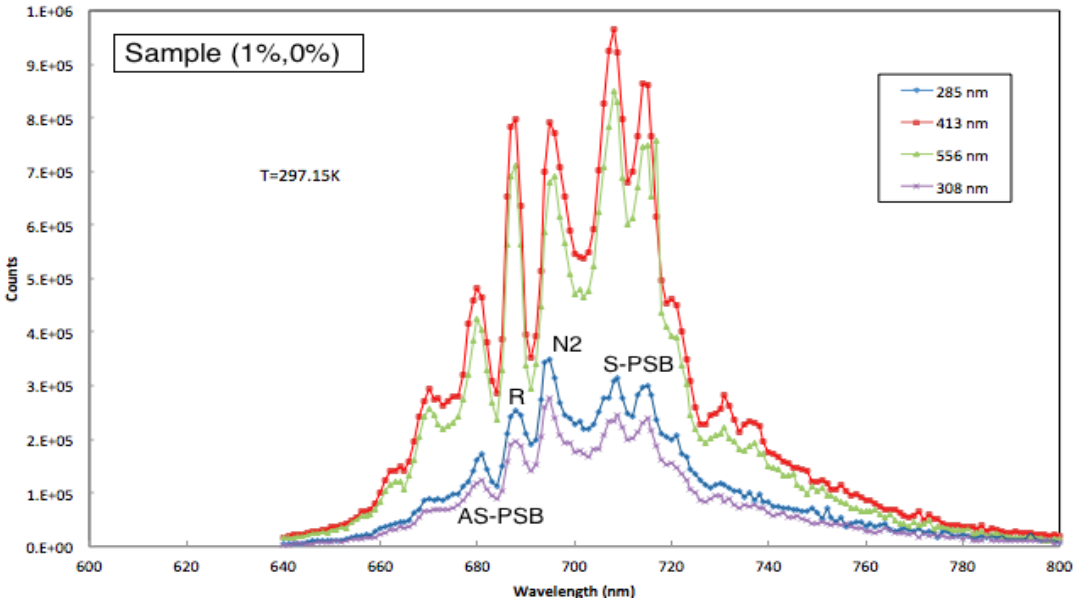

Figure 5.11: Measured emission scans for different excitation wavelengths. We have labeled the different peaks correspondingly with N2 for a chromium atom surrounded by an anti defect and R for a chromium atom that is not surrounded by a anti defect site such as in [17]. The S-PSB and AS-PPS refer to Stokes and anti-Stokes phonon side bands related to emission of excited state between different electronic configurations that are no in the ground-state.

Chapter 6

Combining theory and experiment

This chapter focuses on relating the experimental observed spectroscopic properties with the *ab initio* calculated ones (see chapter 4). Connecting both can be dealt with by the use of crystal field theory. A simple theory that is used to explain the energy levels of an emission center. In our case the emission center is a chromium atom in ZGO and the understanding of such an emission center is thereby fundamental for understanding its optical properties. Crystal field theory is therefore related to the DFT formalism. To give meaning to the Kohn-Sham eigenvalue and eigenfunctions we identify the eigenstates with quasiparticles (see also section 3.4). The predictions of crystal field theory on these particles, that are being studied within the DFT framework, is than compared with the calculations.

6.1 Crystal field theory

Crystal field theory is a simple theory to determine the different energy levels of an emission center [74]. This theory is related with the symmetry of an emission center and its first neighbors. The symmetry of an emission center and its neighbors can give a qualitative picture of the different energy levels of the defect. Crystal field theory is almost always used to explain the optical properties by experimental papers handling emission centers [6] and needs further explanation.

6.1.1 Octahedral and tetrahedral perturbation potential

Crystal field theory approximates an emission center (the chromium atom in ZGO) and it first neighbors (the oxygen atoms) by the emission center and a potential created by its first neighbors on the electrons of the emission center. The relevant potential on the emission site, in this thesis, are created by an octahedral or tetrahedral surroundings given by Eq. (4.10) and (4.12) found in chapter 4.

This extra perturbation potential induces splitting of the energy levels of a free atom. Quantitatively the magnitude of this splitting can be calculated if the wavefunction of the defect is known. In most cases, however, the splitting (expectation value) is calculated by approximating the wavefunction (excited and ground state) by a product of single particle wavefunctions calculated from an inner shell potential caused by the core electrons.

6.1.2 d^1 configuration

The splitting of a d^1 electronic configuration when is trivial as there is no need to consider electron repulsion. The splitting is deduced in chapter 4, section 4.6.2 where it is concluded that for the octahedral surrounding the d_{xy}, d_{yz}, d_{xz} are lowered in energy by $-4Dq$ and the $d_{x^2-y^2}, d_{z^2}$ are raised in energy by $6Dq$. The tetrahedral splitting is here no longer considered because experimentally the chromium atom deduced to be situated on a gallium site [17]. The configuration where a chromium atom is tetrahedral coordinated on a zinc site is thereby of less importance in a chapter comparing experimental and *ab initio* results. In our simulation it was also found that doping ZGO with chromium on the gallium site is more stable than doping it on the zinc site where the formation energy had a small difference, but the defect energy of a chromium substituted on a zinc site was much higher argumentative for why only the octahedral complex is considered (see Tables 4.4 and 4.3).

When there is more than one valence electron the electron repulsion has to be taken into account (Hund rules). Groups theory can give a simplification of the problem and can without calculation explain the splitting of the energy levels from a free atom (see E). Group theory uses the fact that the wavefunctions, which are solutions of the Hamiltonian having the symmetry of the system, are a basis of a representation matrix for the symmetry operations that leave the Hamiltonian invariant. The eigenvalue of the Hamiltonian can then be characterized by the reduced representations. As the symmetry is lowered irreducible representations become reducible and splitting of the levels can be seen from a group theoretical picture. For example when we have a d^1 configuration the d-type single-particle wavefunctions are a basis of the irreducible representation ^2D of the rotation group, which is the symmetry of the free atom and this representation reduces in an octahedral field to the irreducible representation E_g (dim=2) and T_{2g} (dim=3)[1]. This corresponds to the Fig. (4.11) in chapter 4 where the three d orbitals d_{xy} d_{xz} d_{yz} corresponds to the T_{2g} (dim=3) irreducible representation and the d_{z^2} $d_{x^2-y^2}$ corresponds to the E_g (dim=2) irreducible representation of 0_h.

Calculating the splitting of the energy levels, when more than one electron is considered, is now done in function of the strength of the crystal field. This because the strength of the crystal field determines witch potential should be viewed as a perturbation. The calculations are significantly reduced when using a group theoretical approach (see appendix E and F).

6.1.3 Tanabe-Sugano diagram

If the orbitals of the valence electrons are assumed to be d-type the energy of the irreducible configurations, corresponding to the different eigenvalues of the excited wavefunction, can be expressed in 3 parameters, called Racah parameters (A, B, C)[2] [75, 76] and the crystal field strength $\triangle = Dq^3$ [77, 78, 79]. As parameter A is a constant contributions to all energy levels

[1]The number of states is of course equal before and after splitting. The spin is unchanged when reducing the ^2D leading to two irreducible representations corresponding to 4 (^2E_g) and 6 ($^2T_{2g}$) degenerate wavefunctions. In total 10 configurations equal to the number of configurations we started from.

[2]The B and C parameter give a measure of the electron repulsion in d-orbitals.

[3]The energy of the irreducible representation consists of the unperturbed energy and a perturbation. The electron repulsion and the crystal field perturbation can be expressed as a function of Racah parameter and the crystal field strength.

and only energy differences are interesting for spectroscopy, two Racah parameters (B and C) and the crystal field strength (Dq) are enough to describe the perturbed excitation energies. The ratio of B/C is observed to be close to the free ion [80] value and the energy of irreducible representations is only little dependent on it. A graph, given the energy of the irreducible representation of a given electronic configuration in octahedral crystal field, as a function of the crystal field strength in units of parameter B ($\triangle/B$) is called a Tanabe-Sugano diagram. The Tanabe-Sugano diagram is very important in experiments to explain the different excitation bands where the $\triangle/B$ is determined from experiments and from this value all other excitation bands can be deduced as the intersection of this lines with the Tanabe-Sugano diagram. The Tanabe-Sugano diagram relevant for this thesis, is that of a d^3 configuration given in Fig. 6.1. where also the limit of a weak, medium and strong crystal field are shown.

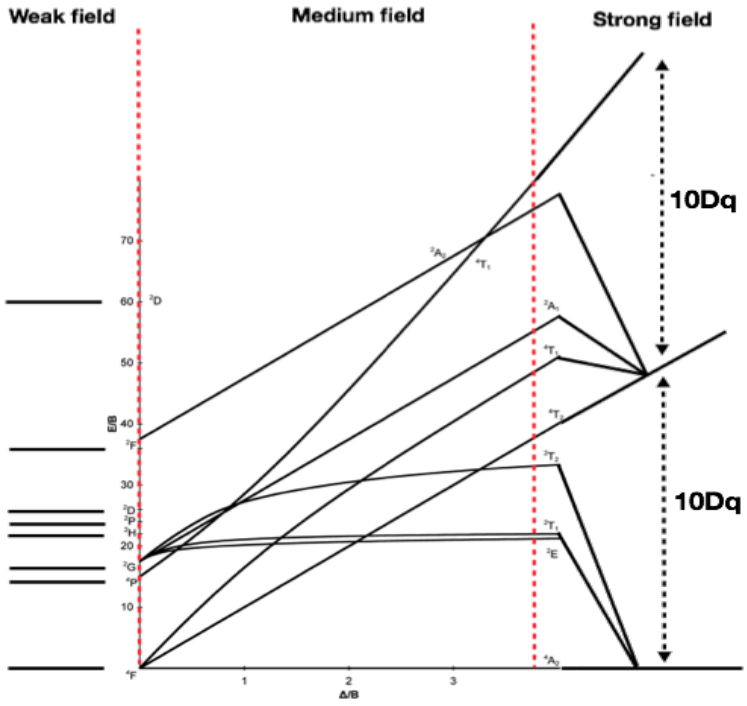

Figure 6.1: Tanabe-Sugano diagram indicating the energy of the possible irreducible representations. The strong, medium and weak field areas are indicated. In the weak field we have the regular LS term symbols. In the medium field also the configuration interaction has to be considered causing bending of the lines. Finally, for the strong field the electron repulsion can be considered as zero and only the discrete levels spaced by the crystal field splitting for a d^1 configuration are observed (for more information see appendix F) [81].

6.2 Crystal field theory in DFT

In the DFT simulations, the Kohn-Sham method invoke one-particle states leading to the correct ground-state density within the used level of theory (PBE). These states are clearly visible in the DOS where also discrete levels of the chromium atom can be seen. In this section the discrete energy levels of the chromium atom will be related to excitation wavelengths. The band

structure and the DOS can be viewed as states that represent the interaction of one electron or hole with the entire system. They also represent non-interacting quasiparticle that make up the correct density. These two statements relate the DOS to measurable values and are used to relate the single-particle energies to full excitation states.

6.2.1 Crystal field for quasiparticles

In chapter 4, section 4.6.2 and also in section 6.1.2 we discussed the splitting of the chromium atom corresponds to a d^1 configuration and not to a d^n configuration because the states are calculated from an independent-particle equation[4] creating the correct ground-state density.

The splitting of the chromium states in the DOS (see section 4.6.2) indeed corresponded to an octahedral crystal field when chromium is situated on a gallium site and to a tetrahedral crystal field when it is situated on a zinc site. The discrete levels of the chromium visible in the DOS are thus the d^1 configuration of the quasiparticles that split in a t_{2g} and e_g state where the t_{2g} is the lower and e_g the higher laying level (see Fig. 4.11). The splitting of these one-particle states of chromium, seen and quantified in the DOS, must be related to full excitation states. Realizing that the unoccupied states in the DOS represents states available to add an electron (see Eq. (3.13)) and occupied states can give an idea of the energy to extract an electron, the splitting between t_{2g} and e_g of the one-particle states can be seen as the energy needed to add an electron and thereby gives us the strength of the crystal field. The splitting of a d^1 configuration (seen in 4.6.2) is given by $10Dq$ and the difference between the t_{2g} and e_g states in the DOS, thereby gives us the strength of the crystal field.

In contrast to the energy between the e_g and t_{2g} chromium levels other energy differences are relevant for this thesis. These relevant energy differences are given in Figure 6.2. Because the energy splitting between the e_g and t_{2g} ($10Dq$) can be linked with the Tanabe-Sugano diagram and through it with the possible excitation we begin by examining this energy difference.

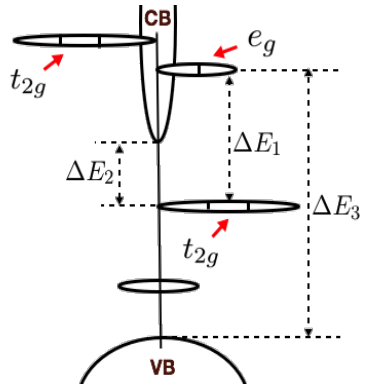

Figure 6.2: The different energies that are quantified and examined for the doped ZGO with and without an antisite defect. The chromium state are indicated by e_g and t_{2g} states.

[4]It is dangerous to speak of an independent particle model because in fact these particles are still coupled to the density.

6.2.2 Tanage-Sugano diagram and density of states

Realizing that the splitting of the e_g and t_{2g} can be seen as the strength of the crystal field exerted on the chromium d-type electrons and this can be used for the parameter $\triangle$ in the Tanabe-Sugano diagram. The extra parameter of this graph, the Racah B parameter, is taken equal to that of a free chromium atom ($B = 918cm^{-1}$ [80])[5]. These two values give us a line in the Tababe-Sugano diagram indicating the different exited states.

As we have introduced different antisite defect configurations in the chromium doped ZGO and the crystal field strength will change when a different antisite defect configuration is introduced around the chromium atom we get multiple lines. In Fig. 6.3 the strength of the crystal field for different configurations is represented. The horizontal line at $2.466eV$ indicates the crystal field strength for the doped host material. From the figure it is evident that the crystal field is being reduced when we introduce an antisite defect. This reduction is the most when the two antisite defect sites are close to the chromium atom.

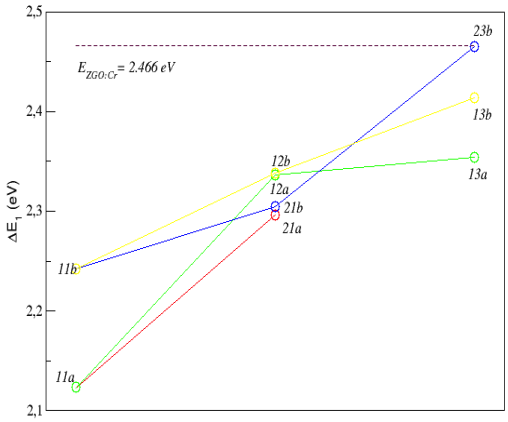

Figure 6.3: The energy between the t_{2g} and e_g chromium levels in the DOS for different antisite configurations introduced in the chromium doped ZGO with the chromium atom on a gallium site. The horizontal line indicates the chromium doped ZGO without an antisite defect site.

The intersection of the lines drawn in the Tanabe-Sugano diagram, related to different crystal field strengths, give us the possible excited states of a chromium atom that is octahedral coordinated on the gallium site. As spin forbidden states will only weakly lead to excitation of the chromium atom they are left out of the Tanabe-Sugano diagram (see Figure 6.4) leading to three possible excitation wavelengths given by

- ${}^4A_2 \rightarrow {}^4T_2$ corresponding with $\lambda_1 = 495 - 583nm$
- ${}^4A_2 \rightarrow {}^4T_1$ corresponding with $\lambda_2 = 339 - 380nm$
- ${}^4A_2 \rightarrow {}^4T_1$ corresponding with $\lambda_3 = 219 - 246nm$

The Tanabe-Sugano diagram seen in Figure 6.4 also shows an artifact of DFT. As single-particle orbital are calculated no full state of the system are achieved. Without the Tanabe-Sugano diagram the state ${}^4T_1$ and other, for example, those having the same rico in the strong

[5] As the electrons of the oxygen atom reduce the effective potential of the chromium atom this parameter will be an overestimation of the repulsion in the one-particle d-type orbitals.

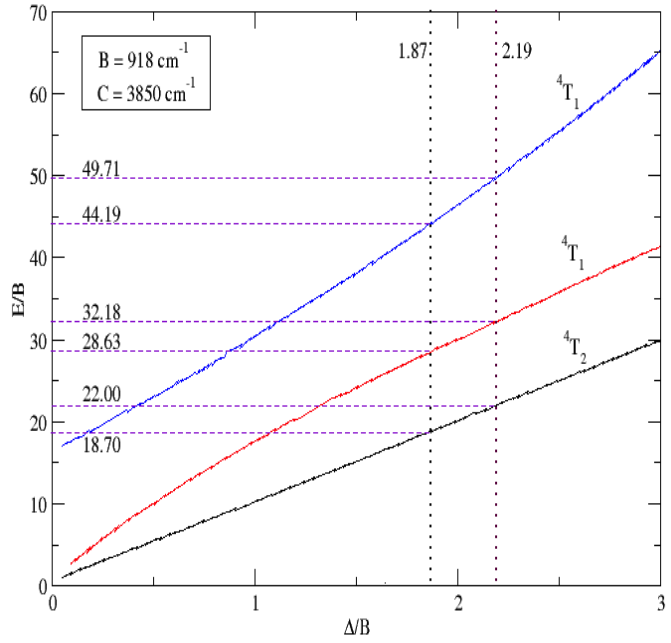

Figure 6.4: Tababe-Sugano diagram [79] where the energy of the irreducible representation is given as a function of three parameters. Parameter B is taken equal to the free ion value just as the ratio B/C, determining the value of parameter C. The energy of the irreducible representation is then plotted against the strength of the crystal field (Δ/B where $\Delta = qD$). All energies are in unit of B and we have left out the spin forbidden excited states.

field limit, are not visible in our simulations. These states can only be calculated when a full state of the system is calculated and out of a single-particle pictures this is impossible. We solve this problem by using the Tanabe-Sugano diagram with DFT (crystal field strength) and experimental values (B, B/C of a free ion) as input.

Already 3 excitation bands are deduced out of the link between DFT, group theory and the Tanabe-Sugano diagram corresponding to our observation in the measured excitation scan (see Figure 5.10). An other excitation band that can be deduced is related to a charge transfer band and is explained and obtained in next section.

6.2.3 Charge transfer

By charge transfer we mean that an electron from the neighbors of the chromium atom is exited to an unoccupied chromium state. The excitation energy for this process is also obtained out of the DOS and is approximated as the energy needed to put an extra electron from the valence band on the chromium. This quantity can not be obtained from crystal field theory as it needs a valence band which is not incorporated in crystal field theory. Quiet simple because in crystal field theory only first neighbors are considered. In order to describe a band we need a lot of atoms and electrons conform with the periodic boundary condition we apply. In the DOS this energy can be deduced as the difference between the valence band and the first unoccupied chromium state. This energy difference is illustrate in Figure 6.5 for the different antisite defect configurations.

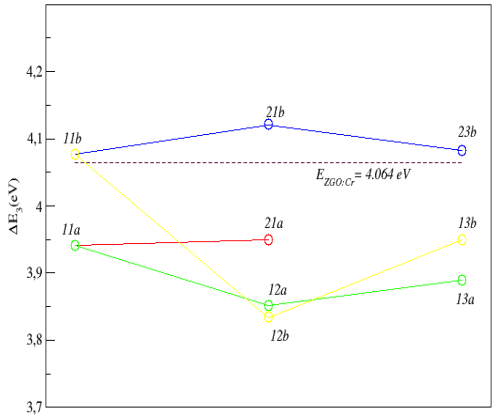

Figure 6.5: In this figure the energy difference between the valency band and the first single-particle state (e_g) can be seen as an approximation of a charge transfer excitation band and is given for all different antisite defect configurations. The horizontal line indicates this difference for a chromium doped ZGO without an antisite defect.

From the above figure it is seen that the difference between the valence band and the first single particle state (e_g) can be considered as constant of around 4 eV. This lead to a extra excitation band with a wavelength around $310nm$.

6.2.4 The excitation bands and emission

Four different excitation bands are found and can be compared to the measured excitation bands. This comparison is done in Table 6.1. The results are in line with what is experimentally

	λ_1 (nm)	λ_2 (nm)	λ_3 (nm)	λ_{CT} (nm)
Theory	583-495	380-339	246-219	317-300
Exp	575-525	425-375	325-275	

Table 6.1: The comparison between experimental and the theoretically excitation bands.

observed. The lowest band is a combination of a charge transfer band and a chromium excitation from ground ($^4A_2$) to excited $^4T_1$ state. From the calculation we could conclude that the band arising from charge transfer corresponds closer to this lowest experimentally observed excitation band than the excitation of the chromium to the $^4T_1$ state that has a smaller wavelength. To test this an excitation scan for smaller wavelength should be preformed to confirm that there is not an extra excitation band from the chromium emission center. Also a more advanced theory such as GW should be used to confirm that the valance band and chromium state do not shift much. This however is something for further research.

Explaining the emission peaks of Fig. 5.11 is however still a bridge to far as in an excited state the wavefunctions changes. This lead to a different overlap and therefore a different inter atomic distances. The change of this distance has a large effect on the crystal field as seen in Eq. (4.10), (4.12). This is the reason why we do not try to explain the emission peaks because the used potential is not suited for it.

6.3 Model for persistent luminescent

In this section a possible model used to explain persistent luminescent given in [5] is briefly compared with results from our DFT calculations. The electrical field created by the antisite defect site surrounding the chromium atom is used to explain why charge separation is accomplished at even large excitation wavelength (visible light). The generated charges then neutralize the charges on the antisite defect site and leads to trapping of energy that can then subsequently be released due to thermal energy causing long emitting luminescence (persistent luminescence).

This electric field surrounding the chromium atom causes the conduction band to be affected and bend. The conduction and is thereby reshaped as illustrated in Fig. 6.6 where a site with and without antisite defect site is compared.

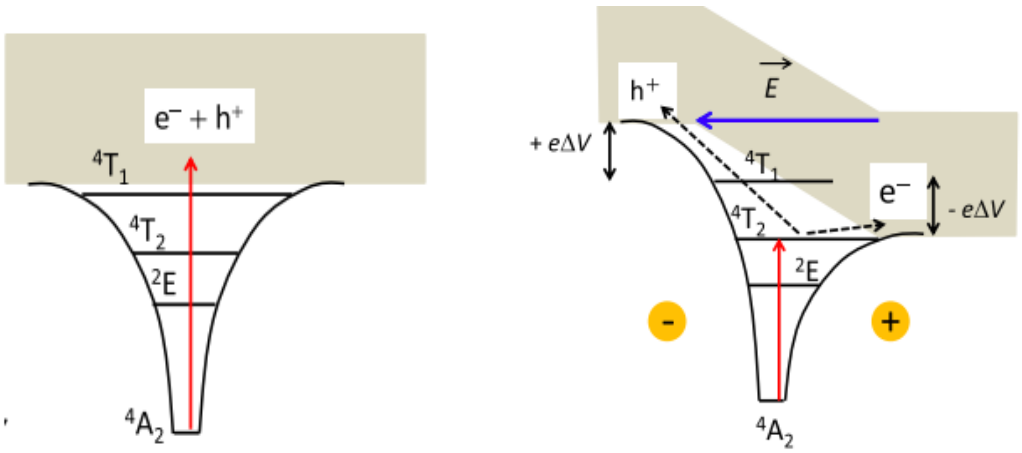

(a) Without antisite defect

(b) With antisite defect

Figure 6.6: Effect of the electric field created by an antisite defect site surrounding the chromium atom [5]. In (a) no antisite defect is present an consequently no electrical field compared to (b) where the antisite defect site creates an electric field that effects the conduction band.

There are a lot problems in testing this proposed model. The most fundamental is that it is a figure with both full excitation states of the chromium emission center and a conduction band created by the total solid. As in the conduction band the electrons and hole are weakly interacting they can be approximately represented by quasiparticles. These are thereby reasonably approximated with the used DFT model. However, the combination of full excited states that are not modeled with the conduction band that is approximated is not within reach of the model used. What we can do is see how the conduction band is situated compared to the occupied t_{2g} level. This energy difference is illustrated in Fig. 6.2 by the energy ΔE_2. This energy difference is plotted for different antisite defect site configurations given in Figure 6.7.

The proposed model suggest that the conduction band should go down in energy. Figure 6.7 confirms a decrease in energy difference between the t_{2g} state and the conduction band. We also see that when the Zn_{Ga}^{-} is farther from the chromium atom than the first shell, the distance between the conduction band and the t_{2g} state is almost identically to the chromium doped ZGO where no antisite defect site, indicated by the horizontal line, is introduced. We conclude that DFT certainly doesn't exclude this model but to have more confirmation more antisite

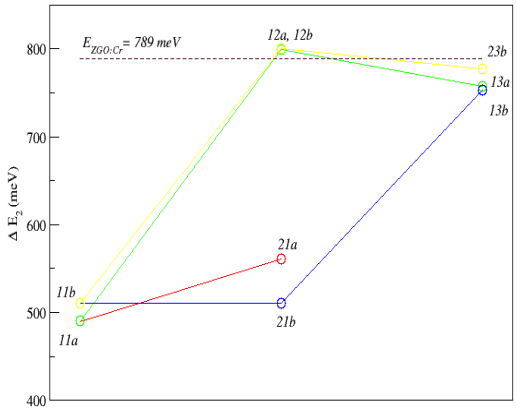

Figure 6.7: The energy difference between the t_{2g} and the conduction band for the different antisite defect configurations (see Fig. 6.2).

defect configurations should be calculated which is impossible in the used unit cell of this thesis. Putting the Zn^{-}_{Ga} close to the chromium atom and increasing the $Ga^{+}_{Zn} - Cr_{Ga}$ distance should give a horizontal line to confirm that the most important antisite defect site is the Zn^{+}_{Ga} site as also was the most important antisite defect site for interaction with the chromium state in chapter 4, section 4.7.

Chapter 7

Conclusions and outlook

Persistent luminescent materials form an fascinating group of materials with a variety of applications. To date, many questions however remain on the precise physical processes responsible for their luminescent behavior. A combination of theory and experiment can yield a deeper understanding. In this thesis, the highly attractive chromium doped zinc gallate phosphor was investigated. It is an interesting persistent phosphor which is–although experimentally intensively studied and characterized–still very challenging from a theoretical perspective.

Firstly, the host material, zinc gallate, was studied with the exchange-correlation term is the 1996 GGA functional of Perdew, Burke and Ernzerhof (PBE). The band structure of the host material provided insights in the relation between different bands. These were calculated in the supercell (SC), in which the band structure is complicated by band folding compared to that of the primitive cell (PC). The band structure was hence unfolded and the unfolded band structure identically matched the PC band structure.

Secondly, the host material was doped with one substitutional chromium atom per unit cell. As all different atoms featured only one nonequivalent lattice site, the three possible dopings where preformed. In line with experiment, the formation energy confirmed chromium situated on a gallium site to be the most stable doping. The difference in formation energy between a chromium substituted on a gallium compared to a zinc site was however relatively small, in contrast to the non-physical case where chromium was doped on an oxygen site. To analyze how stable the dopant is with respect to its surroundings, a dopant energy was calculated. In contrast to the formation energy, the dopant energy suggests that the chromium on a zinc site is highly unstable compared to that on a gallium site. We therefore concluded that the chromium is situated on a gallium site where it is octahedrally surrounded by oxygen atoms. Both dopings on a zinc and a gallium site were, however, further investigated with respect to their electronic structure. This was done to see how a different environment of oxygen atoms, octahedral for a gallium site and tetrahedral for a zinc site, affected the electronic structure of the chromium atom. All band structures were unfolded and clear flat bands of the chromium were visible. The splittings of these levels were in accordance with the octahedral or tetrahedral perturbation potentials acting on the chromium d-states. Also the character of these states was in line with the predictions made by crystal field theory where the t_{2g} states correspond to the d_{xy}, d_{xz} and d_{yz} orbitals and the e_g states correspond to $d_{x^2-y^2}$ and d_{z^2} orbitals.

Lastly an antisite defect–a defect created by the exchange of a zinc and gallium atom–was introduced in the two most stable doped materials. A stability analysis was preformed based on defect energies. These defect energies express the stability of the chromium or antisite. The antisite defect energy in the host material was observed to be only dependent on the distance between both antisite defect sites. When the chromium was substituted on a gallium site, both chromium and antisite defects became more stable when the antisite defect sites were further from the chromium atom and were close to each other. When one antisite defect site was close to the chromium atom, the most stable configuration was that where the gallium antisite defect site, Ga_{Zn}, was located close to the chromium atom. If the chromium atom was substituted on a zinc site the most stable configuration for both chromium and antisite defect was that where the zinc antisite defect site, Zn_{Ga}, was located closely to the chromium and the gallium antisite defect site was as far as possible from the chromium and the other antisite defect site. If, on the contrary, the gallium antisite defect site was located close to the chromium atom, which is a less stable configuration, the other antisite defect site should be as close as possible to both.

The simulations allowed to rationalize the stable configurations based on charge compensation. When the chromium atom is substituted on the gallium site only the antisite defect sites carry charge. The most stable configuration is therefore achieved when they are close to each other. If the chromium atom is doped on a zinc site it contains a positive charge itself. Placing a zinc antisite defect site close to the chromium atom compensates this charge, leading to a more stable configuration. The other antisite defect site should now be placed as far as possible from both dopant and antisite defect site. If the gallium antisite defect site is located close to the chromium atom even more charge instability is created and therefore the other antisite defect site, with opposite charge, should be located close to both.

Comparing the most stable antisite defect configuration of both dopings, chromium doped on a gallium site was still more stable compared to that on a zinc site. However the stabilities of both dopings came closer to each other. The chromium atom substituted on a zinc site was indeed found to become more stable. The antisite defect site is therefore stabilizing the chromium atom doped on the zinc site (from $1.4eV$ to $1.2eV$), but is still much higher in energy than the stable chromium substituted on a gallium site (stays almost constant $\cong -0.248eV$).

After analyzing the stability, the electronic influence of the antisite defect on the properties of both dopings was evaluated. In both dopings the antisite defect introduced band gap states causes by the zinc antisite defect site containing 4 electrons. Interaction between the antisite defect and the chromium atom was assigned to the zinc antisite defect site and was only observed when both where close to each other ($\cong 3\mathring{A}$). Also the band gap states consisted of 2 two-particle states when the antisite defect sites were far from each other. When the antisite defect sites were located close to each other these states split in 4 one-electron states. The chromium atom located on a gallium site had no influence on the band gap states, in contrast to doping on the zinc site where the chromium atom behaved similarly to a second gallium antisite defect site. In that case no further splitting was observed when both chromium and antisite defect were located far from each other.

In the experiments, different doped zinc gallate samples were made. An excitation and emission scan was compared to literature and the same spectra were observed. In the measured

wavelength region of the excitation scan three absorption band were present. These excitation peaks could be explained by crystal field theory when assuming that the chromium is situated on a gallium site. For the derivation, the Tanabe-Sugano diagram of the d^3 configuration of chromium was used. In the emission scan two peaks corresponding to a chromium atom were observed. One was a chromium atom substituted on a gallium site in the neighborhood of an antisite defect, and the other corresponded to a pure chromium on the gallium site without this antisite defect in its surroundings. Both peaks were accompanied by their corresponding Stokes and anti-Stokes side bands.

In density-functional theory the splitting of the chromium states corresponded to the splitting of a d^1 configuration and no full excitation energies were calculated. Instead the Kohn-Sham orbitals could be seen as quasiparticle states leading to the correct ground-state density. However, the crystal field, used in the Tanabe-Sugano diagram, could be approximated from DFT calculations, assuming that the energy needed to add an electron was approximately equal to the splitting of the d^1 configuration. The use of this energy difference for the strength of the crystal field, in combination with the Tanabe-Sugano diagram, determined the the position of the excitation bands without using experimental results.

The calculated bands are in good agreement with the observed experimental excitation bands. In addition an extra charge transfer band was obtained that can not be determined from the Tanabe-Sugano diagram.

Finally, a quite developed experimental model was tested where the electrical field of an antisite defect in the surroundings on the chromium atom was used to explain the efficient creation of excitons upon excitation with visible light. The exciton then compensate the charge on the antisite defect sites, causing energy to be trapped and leading to persistent luminescence. Fundamental in this model is the lowering of the conduction band caused by the electrical field of the antisite defect. The evolution of the conduction band as a function of the different antisite defect configurations was tested with DFT and a small lowering of the conduction band with respect to the chromium states could be observed. To test this model, more configurations that were not possible in the used SC, should be looked at in further research.

A straightforward extension of this research is the use of a more sophisticated first-principles model, term such as HSE or GW, to obtain a better band structure. However, this will not necessarily improve the splitting of the chromium atom energy levels to represent the strength of the crystal field nor enable the calculation of full excitation states of the chromium atom as done in a complete active space calculation (CAS). However, the theoretical approximations of electronic properties dealing with an interaction of a hole or electron with the entire solid will improve. In those cases, it is possible that the relative position of the chromium states to the band gap changes.

The combinations between complete active space (or even full configuration interaction) for the emission center and density-functional theory for the solid is also interesting to examine. This would require a sort of theoretical embedding method, which is presently a fast evolving field.

The correlations of the defect energies of chromium doped zinc gallate with an antisite

defect site as a function of its configuration could be further tested in a larger SC where more configurations are possible. A larger SC necessitates band unfolding as the SC band structure becomes more cumbersome when the supercell is increased in size.

The assignment of the charge transfer excitation band deduced from an energy difference of Kohn-Sham eigenvalues can be further evaluated for other systems by looking at the correspondence with experiments.

It would also be interesting to compensate the induced charge with other kinds of defects as these defects can lead to a more stable configuration. Such research is for example needed to elucidate the valence state of the chromium atom when placed on a zinc site as now the simulations point to a d^4 electronic configuration, which is not observed experimentally. An oxygen vacancy close to the chromium atom could possibly change the electronic configuration to the experimentally observed d^3 state. Many challenges remain and much insight can still be gained, leading to a better knowledge on how to apply DFT for luminescent centers and defects in solid-state materials.

Appendix A

Reciprocal space

Reciprocal space arises from the translational symmetry of the unit cell. Because the density ($n(\overline{r})$ has this symmetry a discrete Fourier transform can be applied to it.

$$n(\overline{r}) = \sum_{\overline{G}} n_{\overline{G}} e^{i\overline{r}\cdot\overline{G}} \tag{A.1}$$

The coefficient, $n_{\overline{G}}$, are different from zero for discrete points, these possible points make up the reciprocal lattice and with it reciprocal space is defined. The vector $\overline{G}$ is the equivalent of the real space translational vector $\overline{T}$, in the same way reciprocal space can be seen as the dual space of real space. The basis vectors of $\overline{G}$ can be obtained out of the primitive basis vectors:

$$\overline{b_1} = 2\pi \frac{\overline{a_2} \times \overline{a_3}}{\overline{a_1} \cdot (\overline{a_2} \times \overline{a_3})} \tag{A.2}$$

$$\overline{b_2} = 2\pi \frac{\overline{a_3} \times \overline{a_1}}{\overline{a_1} \cdot (\overline{a_2} \times \overline{a_3})} \tag{A.3}$$

$$\overline{b_3} = 2\pi \frac{\overline{a_1} \times \overline{a_2}}{\overline{a_1} \cdot (\overline{a_2} \times \overline{a_3})}. \tag{A.4}$$

These three equations are equivalent to

$$\overline{T} \cdot \overline{G} = 2\pi \tag{A.5}$$

and makes the direct connection between the real and reciprocal space as clearly originating from the discrete Fourier transform where the symmetry of the real lattice is the period (see Figure. A.1). The vector $\overline{G}$ can now be written with the help of the reciprocal primitive lattice vectors (A.2), (A.3) and (A.4)

$$\overline{G} = i\overline{b_1} + j\overline{b_2} + k\overline{b_3} \tag{A.6}$$

with i, j, k integers.

Appendix B

Supercell band structure for the primitive reciprocal directions

If one wants to display the folded band structure of the supercell (SC) along the same lines as the primitive cell (PC) a problem arises if the SC is not just a repetition of the PC, for example when SC is a conventional cell of a face-centered cubic (FCC) lattice. In a repetition of the PC the same k path, expressed in fractional coordinates, can be taken in the SC. If however this is not the case one should convert the directions of the high symmetry lines in the BZ of the primitive cell to directions in the SC.

The case considered here is that of a FCC cell where the SC is a conventional cell with conventional lattice vectors. The goal is to find a relationship between the reciprocal lattice vector of the primitive cell and the SC, here the conventional cell. The relationship between the convention and primitive lattice vectors is given by

$$\overline{a}_{p1} = \frac{1}{2}\overline{a}_{c1} + \frac{1}{2}\overline{a}_{c3} \tag{B.1}$$

$$\overline{a}_{p2} = \frac{1}{2}\overline{a}_{c1} + \frac{1}{2}\overline{a}_{c2} \tag{B.2}$$

$$\overline{a}_{p3} = \frac{1}{2}\overline{a}_{c2} + \frac{1}{2}\overline{a}_{c3}. \tag{B.3}$$

and are used to find this relation. Eq. (B.1), (B.2) and (B.3) can also seen from Figure. B.1.

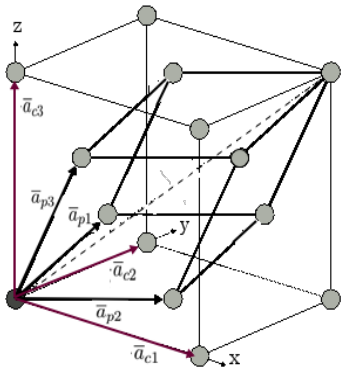

Figure B.1: Relation between the conventional cell (SC) and the primitive cell.

Using Eq. (B.1), (B.2) and (B.3) the relationships between the reciprocal lattice vector of the conventional and primitive lattice can be found, where the primitive and convectional reciprocal lattice vectors are derived by Eq. (A.2), (A.3), (A.4) substituting respectively the primitive and convectional lattice vectors,

$$\overline{b}_{p1} = \overline{b}_{c3} - \overline{b}_{c2} + \overline{b}_{c1} \tag{B.4}$$

$$\overline{b}_{p2} = -\overline{b}_{c3} + \overline{b}_{c3} + \overline{b}_{c1} \tag{B.5}$$

$$\overline{b}_{p2} = \overline{b}_{c2} + \overline{b}_{c3} - \overline{b}_{c1} \tag{B.6}$$

or in matrix representation

$$\begin{pmatrix} \overline{b}_{p1} \\ \overline{b}_{p2} \\ \overline{b}_{p3} \end{pmatrix} = \begin{pmatrix} 1 & -1 & 1 \\ 1 & 1 & -1 \\ -1 & 1 & 1 \end{pmatrix} \begin{pmatrix} \overline{b}_{c1} \\ \overline{b}_{c2} \\ \overline{b}_{c3} \end{pmatrix} \tag{B.7}$$

These equations are enough to determine the k path in the SC corresponding to that in the PC.

The derivation of equations (B.4), (B.5) and (B.6) also give us the tools to explain the extinction rule occurring in an XRD pattern (see section 5.4). The peaks in a XRD pattern are indicated with the Miller indices, in the conventional cell, indicating that the peak is assigned to Bragg reflection on the (hkl) planes. When expressing the reciprocal lattice vector in the conventional reciprocal lattice vectors $\overline{G} = h\overline{b}_{c1} + k\overline{b}_{c2} + l\overline{b}_{c3}$ is related to a Bragg reflection on planes with Miller indices (hkl). However by writing the reciprocal lattice vector in conventional lattice vectors extra points in the reciprocal space are introduced. It is known that only $\overline{G}$ vectors that are in the primitive reciprocal lattice will lead to Bragg reflections therfore (hkl) Miller exist that will have no peaks. This Miller indices are related to points of the reciprocal conventional lattice, expressed by $\overline{G} = h\overline{b}_{c1}+k\overline{b}_{c2}+l\overline{b}_{c3}$, that are not in the primitive reciprocal lattice[1]. To see witch points lead to zero we only have to express the conventional reciprocal lattice vector with factors (hkl) as a function of the primitive reciprocal lattice where only integer values before the primitive reciprocal lattice basis will cause Bragg reflections. The combinations of (hkl) values that will not lead to integer values are the extra points in the reciprocal conventional lattice compared to the primitive reciprocal lattice and will have zero peaks in the XRD pattern. As example in an FCC lattice it follows that

$$\overline{G} = h\overline{b}_{c1} + k\overline{b}_{c2} + l\overline{b}_{c3} \tag{B.8}$$

$$\overline{G} = \frac{h+l}{2}\overline{b}_{p1} + \frac{h+k}{2}\overline{b}_{p2} + \frac{l+k}{2}\overline{b}_{p3}. \tag{B.9}$$

and the (hkl) Miller indices that lead to integer values before the primitive reciprocal lattice are those where the sum of the indices are even all other (hkl) planes will not lead to Bragg reflections. This is called an extinction rule of FCC and similar extinction rule exist for other crystal symmetries.

[1]Some points that are present in the primitive reciprocal lattice can still be zero because of the structure factor (see section 5.4), however this related to the electronic symmetry and not on the symmetry of the crystal

Appendix C

Structure parameters

In this appendix we summarize in tables C.1 and C.3 the structural information of the basic materials calculated in this thesis.

	B_0 (Mbar)		Volume (angst.)	
	Theory	Exp	Theory	Exp
O	0.0118	0.0297[82]	77.1190	69.4454[82]
Ga	0.4700(0.4503)	0.569[83]	162.7992(164.3435)	156.76[84]
Zn	0.7230(0.6359)	0.598[83]	30.3380(31.0611)	30.659[85]
Cr	1.8706(1.7696)	1.901[83]	23.5003(23.7900)	24[86]
$Zn0$	1.2852(1.2620)	1.81[63]	49.7040(49.9488)	47.6150[63]
Ga_2O_3	1.5296(1.5035)	2.28[87]	220.2025(221.2496)	208.85[87]
Cr_20_3	2.0370(2.162)	2.31[29]	97.4427(97.7334)	96.433[29]
ZGO	1.6730(1.4809)	2.33[72]	606.8772(609.7325)	580.1[72]
$ZGO : Cr^{3+}_{Ga}$	1.6777(1.6441)	N.A.	606.3868(609.1501)	N.A.
$ZGO : Cr^{3+}_{Zn}$	1.6610(1.6284)	N.A.	609.9036(612.6546)	N.A.
$ZGO : Cr^{3+}_{O}$	1.5286(1.4981)	N.A.	619.0968(621.9245)	N.A.

Table C.1: Basic optimization properties compared to experiment. Between brackets the corrected value for room temperature (298.15K) is given with the use of [88] and Table. C.4 where the necessary values are given.

	Calculated Lattice Parameters					
	a	b	c	a^b	b^c	a^c
O	4.2483	4.2483	4.6902	90	90	65.9431
Ga	4.5778(4.5922)	7.7546(7.7790)	4.5860(4.6005)	90	90	90
Zn	2.6669(2.6879)	2.6669((2.6879)	4.9255(4.9643)	60	90	90
Cr	2.8643(2.8760)	2.8643(2.8760)	2.8643(2.8760)	90	90	90
ZnO	3.2883(3.2937)	3.2883(3.2937)	5.3080(5.3167)	120	90	90
Cr_2O_3	4.9396(4.9445)	4.9396(4.9445)	5.4220(5.4274)	60	62.9017	62.9017
Ga_2O_3	12.4740(12.4937)	3.0877(3.0926)	5.8834(5.8927)	90	90	103.6748
ZGO	8.4659(8.4792)	8.4659(8.4792)	8.4659(8.4792)	90	90	90
$ZGO : Cr^{3+}_{Zn}$	8.4805(8.4932)	8.4805(8.4932)	8.4805(8.4932)	90	90	90
$ZGO : Cr^{3+}_{Ga}$	8.4641(8.4769)	8.4641(8.4769)	8.4641(8.4769)	90.0054	90.0054	89.9946
$ZGO : Cr^{3+}_{O}$	8.5232(8.5362)	8.5232(8.5362)	8.5232(8.5362)	89.4849	90.5151	90.5151

Table C.2: Calculated lattice parameters with VASP using a level of theory of PBE combined with PAW. Cutoff energy of 800 eV and k-mesh density 11140 kpoints/ Å. Between brackets the corrected value for room temperature (298.15K) is given with the use of [88] and Table. C.4 where the necessary values are given.

	Experimental values of the lattice parameters					
	a	b	c	a^b	b^c	a^c
O	3.75[82]	3.43[82]	5.38[82]	90[82]	90[82]	117.76[82]
Ga	4.52[84]	7.66[84]	4.52[84]	90[84]	90[84]	90[84]
Zn	2.67[85]	2.67[85]	4.97[85]	90[85]	90[85]	90[85]
Cr	2.88[86]	2.88[86]	2.88[86]	90[86]	90 [86]	90[86]
ZnO	3.2495[63]	3.2495[63]	5.2069[63]	120[63]	90[63]	90[63]
Cr_2O_3	5.3619[28]	5.3619[28]	5.3619[28]	55.12[28]	55.12[28]	55.12[28]
Ga_2O_3	12.214[87]	3.0371[87]	5.7981[87]	90[87]	90[87]	103.83[87]
ZGO	8.33[89]	8.33[89]	8.33[89]	90[89]	90[89]	90[89]
$ZGO : Cr^{3+}_{Zn}$	N.A.					
$ZGO : Cr^{3+}_{Ga}$	N.A.					
$ZGO : Cr^{3+}_{O}$	N.A.					

Table C.3: Experimental values at room temperature (except for oxygen which is only a solid at a temperature close to zero Kelvin)

	$\theta_D(K)$	$\triangle E_{mol}(eV)$	$\alpha_{V,rt}\ mK^{-1}$	B_1	$(B_0B_2)^{BM}$	$\triangle V^{(1)}(\mathring{A}^3)$	$\triangle V^{(2)}(\mathring{A}^3)$	$\triangle B^{(1)}(Mbar)$	$\triangle B^{(2)}(kbar)$
Ga	325[83]	2.6339	0.0548	4.9920	-5.8650	1.3300	0.2143	-0.0192	-0.4633
Cr	630[83]	4.0442	0.0357	7.2944	-18.0364	0.1251	0.1646	-0.0726	-28.3873
Zn	327[83]	1.1021	0.1310	4.7169	-5.1197	0.5925	0.1306	-0.0668	-2.032
ZnO	303[90]	5.6087	0.0257	4.5392	-4.7188	0.1904	0.0544	-0.0223	-0.8519
Cr_2O_3	370[91]	8.4088	0.0172	3.8895	-3.7906	0.2499	0.0408	-0.0203	-0.4859
Ga_2O_3	872[92]	5.1970	0.0278	4.0370	-3.9273	0.9126	0.1345	-0.0256	-0.5184
ZGO	591[93]	4.7385	0.0305	4.4988	-4.6365	2.7593	0.0960	-0.0342	-0.1579
$ZGO : Cr^{3+}_{Ga}$	591[a]	4.8818	0.0295	4.5315	-4.7029	2.6667	0.0966	-0.0334	-0.1614
$ZGO : Cr^{3+}_{Zn}$	591[a]	4.9412	0.0292	4.4782	-4.5958	2.6549	0.0961	-0.0324	-0.1551
$ZGO : Cr^{3+}_{O}$	591[a]	4.8920	0.0295	4.5009	-4.6407	2.7226	0.1051	-0.0303	-0.1550

Table C.4: Necessary values needed to calculate the correction to bring the results to room temperature [88].

[a] The Debye temperature for the doped material is taken equal to the Debye temperature of the pure ZGO material given in [93] .

Appendix D

Antisite defect energy

In this appendix the different defect energies are summarized in Table. D.1, D.2 and D.3.

$Ga_{Zn}Zn_{Ga}$	$E^{1def}_{Anti-Cr}$ (meV/def)	E^{1def}_{Anti} (meV/def)	$E^{1def}_{Cr-Anti}$ (meV/def)
11a	675	641	-214
11b	608	593	-233
11c	609	593	-232
12a	650	641	-239
12b	601	593	-240
13a	647	641	-242
13b	589	593	-252
21a	658	641	-231
21b	609	593	-232
23b	584	593	-257

Table D.1: Defect energies of chromium doped ZGO on the gallium site for different antisite defect configurations (see section 4.7.1).

$Ga_{Zn}Zn_{Ga}$	$E^{1def}_{Anti-Cr}$ (meV/def)	E^{1def}_{Anti} (meV/def)	$E^{1def}_{Cr-Anti}$ (meV/def)
11a	476	641	1243
11b	427	593	1243
12a	414	641	1182
12b	451	593	1267
21a	629	641	1397
21b	553	593	1369
22b	476	593	1291

Table D.2: Defect energies of chromium doped ZGO on the zinc site for different antisite defect configurations (see section 4.7.2).

	$E_{Anti-Cr}$ (meV/ZGO)	$E_{Anti-ZGO\_Ga}$ (meV/ZGO)
11a	84	267
11b	76	260
11c	76	N.A.
12a	81	263
12b	75	286
13a	81	N.A.
13b	74	N.A.
21a	82	286
21b	76	276
23b	73	N.A.
22b	N.A.	267

Table D.3: Comparison of energy with as reference a chromium doped ZGO on the gallium site without an antisite defect where each compound is corrected to have an equal amount of zinc and gallium atoms as chromium doped ZGO on the gallium site (see section 4.7.2).

Appendix E

Group theory

If a material or defect has a specific symmetry, a corresponding set of symmetry operators exist that leave the system unchanged. Symmetry theory focuses on the representations of the symmetry group and more particular on irreducible representations of the symmetry group. A representation of a symmetry group is a group of square matrices where subsequent symmetry operations corresponds to matrix multiplication. In this way an injective relation can be constructed between every symmetry element and a square matrix called a homomorphisme. A representation is called an irreducible representations[1] if the matrix can not be transformed in a block matrix by a similarity transformation. For example, a free atom has the irreducible representation of the rotation group.

The symmetry of a system is of course a symmetry group of the Hamiltonian describing the system. Group theory shows that every irreducible representation corresponds to an eigenspace[2]. The dimension of this eigenspace is equal to the dimension of the matrix of the irreducible representation. In the quantum mechanical picture this eigenspace consist of degenerate wavefunctions with eigenvalue the energy. It thereby becomes possible to label the states, ground and excited, by irreducible representations.

As one reduces the order of the corresponding symmetry group for which one has an irreducible representation, for example when introducing a free atom in a solid or introducing a defect in a solid, these irreducible representation becomes, because less constrictions by less symmetry elements, reducible (see Figure. E.1). Meaning that in this reduced symmetry group it is possible to block diagonalize the previous irreducible representation in 2 or more irreducible representation by use of a similarity transformation. These two representation irreducible representation again label the corresponding eigenvalue and eigenspace. In doing the reduction to the irreducible representations we see which levels will split due to the reduction of symmetry.

It can be seen that reducing the symmetry is equal to a perturbation of the system (see Figure. E.1) where the total Hamiltonian is being reduced in symmetry by this perturbation. A perturbation can be seen as an extra potential with a lower symmetry of the unperturbed Hamiltonian thereby reducing the symmetry of the total system.

Quantitative the splitting of energy levels is obtained by calculating the expectation value of

[1] For a finite symmetry group their are finite number, for an infinite symmetry group, for example the group of all rotations there are infinite number of irreducible representations.

[2] We actually mean that the (degenerate) eigenfunctions with energy as eigenvalue transform as an irreducible representation when applying a symmetry element to it.

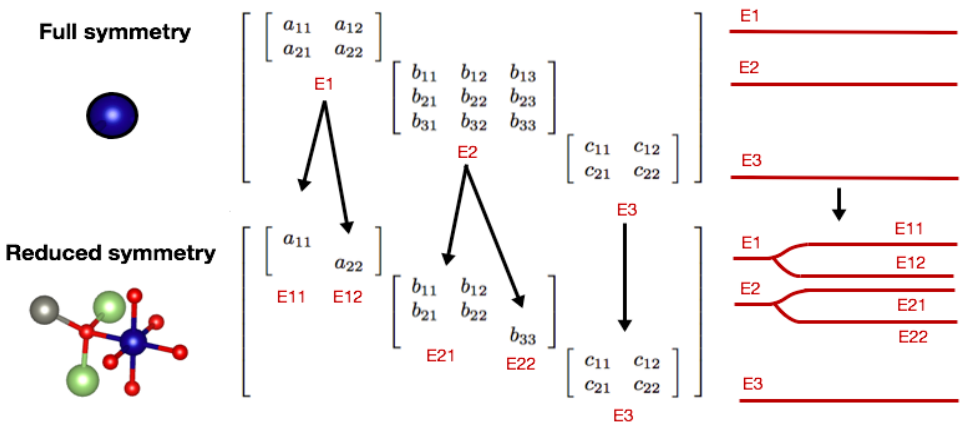

Figure E.1: A schematic example of the spitting of energy levels due to a reduction of the symmetry from a free chromium atom to a chromium atom in an octahedral defect. In the middle a block matrix is presented and the splitting of the energy levels (illustrated at the right) is equivalent with the reduction of the blocks in this matrix.

the perturbation potential for every wavefunction that belongs to an irreducible representation. The strategy in calculating the splitting of the energy levels thus consist of reducing the previous irreducible representation in irreducible representation of the reduced symmetry caused by the perturbation potential. These irreducible representation are then related to wavefunctions transforming like this irreducible representation or in other words belonging to it. The expectation value of the wavefunctions related to the different irreducible representation is then calculated to obtain a first order splitting of the energy levels[3].

[3]Only one expectation value should be calculated for every irreducible representation as the other degenerate wavefunction give the same eigenvalue.

Appendix F

Crystal field for a d^n configuration

When more one valence electron is present, in the d-orbitals, electron repulsion has to be considered. The crystal field potential or electron repulsion is considered as a perturbation depending on the the crystal strength. This causes to tackle the problem of calculating the perturbation energy as a function of the crystal field strength. The precise calculated perturbation is not done but the procedure is illustrated. Group theory is here applied to obtain a significant reduction of calculation (see appendix for brief summary of E).

F.1 Strong crystal field

If the crystal field is strong the electron repulsion can be considered as a perturbation of the crystal field. The unperturbed electronic configuration are given by (see section 4.6.2) e_g^n, $t_{2g}e_g^{n-1}$, ... , t_{2g}^n with an energy of $t_{2g}^k e_g^{n-k}$ given by

$$E(k) = (-4k + 6(n-k))Dq \tag{F.1}$$

The electron repulsion is now added as a perturbation. The splitting of the energy levels given by F.1 is now easily obtained by applying group theory. A configuration given by $t_{2g}^k e_g^{n-k}$ has eigenfunctions that transform according to $t_{2g}^k \otimes e_g^{n-k}$ where, the wavefunctions are approximated by product like wavefunctions. A reduction of this representation to the symmetry group of the Hamiltonian give the qualitative splitting of the different unperturbed energy levels[1]. In an octahedral d^3 configurations the unperturbed strong field electronic configurations split in the corresponding irreducible representations

$$t_{2g}^3 \rightarrow {}^4A_2, {}^2E, {}^2T_1, {}^2T_2$$

$$t_{2g}^2 e_g \rightarrow {}^4T_1, {}^4T_2, {}^2A_1, {}^2A_2, 2({}^2E), 2({}^2T_1), 2({}^2T_2)$$

$$t_{2g}e_g^2 \rightarrow {}^4T_1, 2({}^2T_1), 2({}^2T_2)$$

[1] A configuration where two electrons are in a different state (e_g or t_{2g}) this procedure is quite simple however when more then two electrons are in the same state the Pauli principle excludes certain irreducible representation. The possible irreducible representation are now found by looking directly at the transformation of the different eigenfunction.

$$e_g^3 \rightarrow^2 E$$

Each irreducible representation is generated by linear combination of product like (unperturbed) wavefunctions. The degeneracy of $^{2S+1}\Gamma$ is given by $(2S+1)\Gamma$ where gamma is the dimension of the irreducible representation (1 for A_1, A_2, B_1 and B_2, 2 for E and 3 for T_1 and T_2). Only wavefunctions corresponding to different irreducible representation give a different expectation value therefore only the expectation value of one representative wavefunction corresponding to an irreducible representation should be calculated for the electron repulsion perturbation. In the splitting of the t_{2g} configurations following expectation values will have to be calculated:

$$\langle t_{2g}^3(^4A_2)|V|t_{2g}^3(^4A_2)\rangle, \langle t_{2g}^3(^2E)|V|t_{2g}^3(^2E)\rangle, \langle t_{2g}^3(^2T_1)|V|t_{2g}^3(^2T_1)\rangle, \langle t_{2g}^3(^2T_2)|V|t_{2g}^3(^2T_2)\rangle$$

where $V = \dfrac{e^2}{r_{12}} + \dfrac{e^2}{r_{23}}$ is the electron repulsion.

F.2 Medium crystal field

When the crystal field is reduced in strength also expectation values of common irreducible representations from different electronic configurations ($t_{2g}^k e_g^{n-k}$) has to be considered. This interaction is called the configuration interaction and leads to an eigenvalue equation between irreducible terms of different configurations. In the octahedral configurations we will have a secular equation for $^2T_1$, $^2T_2$, ^2E, $^4T_1$. Because of this configuration interactions extra matrix elements have to be calculated, for example

$$\langle t_{2g}^3(^2T_2)|V|t_{2g}^2 e_g(^2T_2)\rangle.$$

F.3 Weak crystal field

With a weak crystal field the procedure is reversed and the octahedral crystal field is considered as a perturbation. The irreducible representations are then first derived for a typical free ion. These are the common LS terms with symbol S, P, D, F, ... For a d^3 configurations these irreducible representations are given by ^2P, $2(^2D)$, ^2F, ^2G, ^2H and ^4P, ^4F. These terms are then reduced to the octahedral or tetrahedral symmetry group leading to the same terms as previous.

Appendix G

Splitting energy of octahedral complex

In this appendix we summarize the different energies in Table. G.1 indicated in Fig. 6.2.

	ΔE_1	ΔE_2	ΔE_3	λ_1	λ_2	Δ/B
11a	2.123	0.819	3.941	584	322	1.87
11b	2.242	0.510	4.077	553	304	1.97
11c	2.408	0.592	4.123	515	300	2.12
12a	2.356	0.819	3.852	526	322	2.07
12b	2.358	0.820	3.834	525	323	2.07
13a	2.354	0.757	3.889	527	319	2.07
13b	2.414	0.777	3.949	513	314	2.12
21a	2.296	0.561	4.082	540	304	2.02
21b	2.387	0.530	4.121	519	296	2.10
23b	2.491	0.779	4.082	498	304	2.19
Undoped	2.466	0.789	4.064	502	305	2.17

Table G.1: The different energy differences between chromium states seen in Fig. 6.2.

List of Figures

List of Tables

Bibliography

[1] J. Hölsä, "Persistent Luminescence Beats the Afterglow - 400 Hundred Years of Persistent Luminescence," *Electrochemical Society Interface, The 18(2009)4,42-45.*

[2] H. F. Brito, J. Hölsä, T. Laamanen, M. Lastusaari, M. Malkamäki, and L. C. V. Rodrigues, "Persistent luminescence mechanisms: human imagination at work," *Optical Materials Express*, vol. 2, pp. 371–381, Apr. 2012.

[3] N. Basavaraju, K. R. Priolkar, D. Gourier, S. K. Sharma, A. Bessière, and B. Viana, "The importance of inversion disorder in the visible light induced persistent luminescence in Cr^{3+} doped AB_2O_4 (A = Zn or Mg and B = Ga or Al)," *Phys. Chem. Chem. Phys.*, vol. 17, no. 3, pp. 1790–1799, 2015.

[4] A. Bessière, S. K. Sharma, N. Basavaraju, K. R. Priolkar, L. Binet, B. Viana, A. J. J. Bos, T. Maldiney, C. Richard, D. Scherman, and D. Gourier, "Storage of Visible Light for Long-Lasting Phosphorescence in Chromium-Doped Zinc Gallate," *Chemistry of Materials*, vol. 26, pp. 1365–1373, Feb. 2014.

[5] D. Gourier, A. Bessière, S. Sharma, L. Binet, B. Viana, N. Basavaraju, and K. R. Priolkar, "Origin of the visible light induced persistent luminescence of cr^{3+}-doped zinc gallate," *Journal of Physics and Chemistry of Solids*, vol. 75, pp. 826–837, July 2014.

[6] S. Sharma, D. Gourier, B. Viana, T. Maldiney, E. Teston, D. Scherman, and C. Richard, "Persistent luminescence of $A2o4 : Cr^{3+}$ (A=Zn, Mg, B=Ga, Al) spinels: New biomarkers for in vivo imaging," *Optical Materials*, vol. 36, pp. 1901–1906, Sept. 2014.

[7] T. Maldiney, A. Bessière, J. Seguin, E. Teston, S. K. Sharma, B. Viana, A. J. J. Bos, P. Dorenbos, M. Bessodes, D. Gourier, D. Scherman, and C. Richard, "The in vivo activation of persistent nanophosphors for optical imaging of vascularization, tumours and grafted cells," *Nat Mater*, vol. 13, pp. 418–426, Apr. 2014.

[8] L. Oudijk, F. van Nederveen, C. Badoual, F. Tissier, A. S. Tischler, M. Smid, J. Gaal, C. Lepoutre-Lussey, A.-P. Gimenez-Roqueplo, W. N. Dinjens, E. Korpershoek, R. de Krijger, and J. Favier, "Vascular Pattern Analysis for the Prediction of Clinical Behaviour in Pheochromocytomas and Paragangliomas," *PLoS ONE*, vol. 10, Mar. 2015.

[9] D. Lockwood, D. Einstein, and W. Davros, "Diagnostic imaging: radiation dose and patients' concerns," *Cleveland Clinic Journal of Medicine*, vol. 73, pp. 583–586, June 2006.

[10] Y. Zhuang, Y. Katayama, J. Ueda, and S. Tanabe, "A brief review on red to near-infrared persistent luminescence in transition-metal-activated phosphors," *Optical Materials*, vol. 36, pp. 1907–1912, Sept. 2014.

[11] R. Hill, J. Craig, and G. Gibbs, "Systematics of the spinel structure type," *Physics and Chemistry of Minerals*, vol. 4, no. 4, pp. 317–339, 1979.

[12] S.-H. Wei and S. B. Zhang, "First-principles study of cation distribution in eighteen closed-shell $A^{\mathrm{ii}}B_2^{\mathrm{iii}}\mathrm{o}_4$ and $A^{\mathrm{iv}}B_2^{\mathrm{ii}}\mathrm{o}_4$ spinel oxides," *Phys. Rev. B*, vol. 63, p. 045112, Jan 2001.

[13] N. Basavaraju, K. R. Priolkar, D. Gourier, A. Bessière, and B. Viana, "Order and disorder around Cr^{3+} in chromium doped persistent luminescent AB_2O_4 spinels," *Phys. Chem. Chem. Phys.*, vol. 17, no. 16, pp. 10993–10999, 2015.

[14] M. K. Jayaraj, *Anoop G i.* PhD thesis, Cochin University of Science and Technology, 2008.

[15] R. Pandey, J. D. Gale, S. K. Sampath, and J. M. Recio, "Atomistic simulation study of spinel oxides: zinc aluminate and zinc gallate," *Journal of the American Ceramic Society*, vol. 82, no. 12, pp. 3337–3341, 1999.

[16] A. Bessière, S. Jacquart, K. Priolkar, A. Lecointre, B. Viana, and D. Gourier, "$ZnGa_2O_4$: Cr^{3+}: a new red long-lasting phosphor with high brightness," *Optics express*, vol. 19, no. 11, pp. 10131–10137, 2011.

[17] S. K. Sharma, A. Bessière, N. Basavaraju, K. R. Priolkar, L. Binet, B. Viana, and D. Gourier, "Interplay between chromium content and lattice disorder on persistent luminescence of $ZnGa_2O_4$: Cr^{3+} for in vivo imaging," *Journal of Luminescence*, vol. 155, pp. 251–256, Nov. 2014.

[18] X. Duan, J. Liu, Y. Wu, F. Yu, and X. Wang, "Structure and luminescent properties of Co^{2+}/Cr^{3+} co-doped $ZnGa_2O_4$ nanoparticles," *Journal of Luminescence*, vol. 153, pp. 361–368, Sept. 2014.

[19] J. Hafner, "Ab-initio simulations of materials using VASP: Density-functional theory and beyond," *Journal of Computational Chemistry*, vol. 29, pp. 2044–2078, Oct. 2008.

[20] J. P. Perdew, K. Burke, and M. Ernzerhof, "Generalized gradient approximation made simple," *Phys. Rev. Lett.*, vol. 77, pp. 3865–3868, Oct 1996.

[21] W. Kohn, "Nobel Lecture: Electronic structure of matter-wave functions and density functionals," *Reviews of Modern Physics*, vol. 71, no. 5, pp. 1253–1266, 1999.

[22] K. Capelle, "A bird's-eye view of density-functional theory," *Brazilian Journal of Physics*, vol. 36, no. 4A, pp. 1318–1343, 2006.

[23] A. Savin, F. Colonna, and R. Pollet, "Adiabatic connection approach to density functional theory of electronic systems," *International Journal of Quantum Chemistry*, vol. 93, pp. 166–190, Jan. 2003.

[24] A. J. Cohen, P. Mori-Sánchez, and W. Yang, "Challenges for Density Functional Theory," *Chemical Reviews*, vol. 112, pp. 289–320, Jan. 2012.

[25] X.-M. Tong and S.-I. Chu, "Density-functional theory with optimized effective potential and self-interaction correction for ground states and autoionizing resonances," *Physical Review A*, vol. 55, no. 5, p. 3406, 1997.

[26] Y. Niquet, M. Fuchs, and X. Gonze, "Exchange-correlation potentials in the adiabatic connection fluctuation-dissipation framework," *Physical Review A*, vol. 68, Sept. 2003.

[27] O. Gunnarsson, "Band model for magnetism of transition metals in the spin-density-functional formalism," *Journal of Physics F: Metal Physics*, vol. 6, p. 587, Apr. 1976.

[28] F. Maldonado, C. Novillo, and A. Stashans, "Ab initio calculation of chromium oxide containing Ti dopant," *Chemical Physics*, vol. 393, pp. 148–152, Jan. 2012.

[29] J. A. Cline, A. A. Rigos, and T. A. Arias, "Ab initio study of magnetic structure and chemical reactivity of Cr_2O_3 and its (0001) surface," *The Journal of Physical Chemistry B*, vol. 104, no. 26, pp. 6195–6201, 2000.

[30] N. Troullier and J. L. Martins, "Efficient pseudopotentials for plane-wave calculations," *Physical Review B*, vol. 43, no. 3, p. 1993, 1991.

[31] "Pseudopotential," Mar. 2015. Page Version ID: 650715630.

[32] P. E. Blöchl, "Projector augmented-wave method," *Phys. Rev. B*, vol. 50, pp. 17953–17979, Dec 1994.

[33] G. Kresse and D. Joubert, "From ultrasoft pseudopotentials to the projector augmented-wave method," *Phys. Rev. B*, vol. 59, pp. 1758–1775, Jan 1999.

[34] H. J. Monkhorst and J. D. Pack, "Special points for Brillouin-zone integrations," *Physical Review B*, vol. 13, pp. 5188–5192, June 1976.

[35] M. Scheffler and V. Blum, *Theoretische Festkörperphysik I and II*. Technische Universität Berlin, 2008.

[36] M. A. Boyko and I. V. Abarenkov, "Crystal band structure from the embedded cluster," *International Journal of Quantum Chemistry*, vol. 113, pp. 1877–1883, July 2013.

[37] T.-C. Chiang, J. A. Knapp, M. Aono, and D. E. Eastman, "Angle-resolved photoemission, valence-band dispersions $e(\overline{k})$, and electron and hole lifetimes for GaAs," *Physical Review B*, vol. 21, no. 8, p. 3513, 1980.

[38] A. Damascelli, "Probing the low-energy electronic structure of complex systems by ARPES," *arXiv preprint cond-mat/0307085*, 2003.

[39] K. C. Pandey and J. C. Phillips, "Nonlocal pseudopotentials for ge and gaas," *Phys. Rev. B*, vol. 9, pp. 1552–1559, Feb 1974.

[40] P. Brommer and D. Quigley, "Automated effective band structures for defective and mismatched supercells," *Journal of Physics: Condensed Matter*, vol. 26, p. 485501, Dec. 2014.

[41] A. Ajoy, K. V. R. M. Murali, and S. Karmalkar, "Brillouin zone unfolding of complex bands in a nearest neighbour tight binding scheme," *Journal of Physics: Condensed Matter*, vol. 24, p. 055504, Feb. 2012.

[42] T. Boykin and G. Klimeck, "Practical application of zone-folding concepts in tight-binding calculations," *Physical Review B*, vol. 71, Mar. 2005.

[43] W. Ku, T. Berlijn, and C.-C. Lee, "Unfolding First-Principles Band Structures," *Physical Review Letters*, vol. 104, May 2010.

[44] M. Tomi, H. O. Jeschke, and R. Valent, "Unfolding of electronic structure through induced representations of space groups: Application to Fe-based superconductors," *Physical Review B*, vol. 90, Nov. 2014.

[45] V. Popescu and A. Zunger, "Extracting E versus $\overline{k}$ effective band structure from supercell calculations on alloys and impurities," *Physical Review B*, vol. 85, Feb. 2012.

[46] P. V. C. Medeiros, S. Stafström, and J. Björk, "Effects of extrinsic and intrinsic perturbations on the electronic structure of graphene: Retaining an effective primitive cell band structure by band unfolding," *Physical Review B*, vol. 89, Jan. 2014.

[47] P. V. Medeiros, S. S. Tsirkin, S. Stafström, and J. Björk, "Unfolding spinor wavefunctions and expectation values of general operators: Introducing the unfolding-density operator," *arXiv preprint arXiv:1409.5343*, 2014.

[48] O. Rubel, A. Bokhanchuk, S. J. Ahmed, and E. Assmann, "Unfolding the band structure of disordered solids: From bound states to high-mobility Kane fermions," *Physical Review B*, vol. 90, Sept. 2014.

[49] F. Bruneval, N. Vast, and L. Reining, "Effect of self-consistency on quasiparticles in solids," *Physical Review B*, vol. 74, July 2006.

[50] J. F. Janak, "Proof that $\frac{$\partial${}e}{$\partial${}{n}_{i}}=$\epsilon${}$ in density-functional theory," *Physical Review B*, vol. 18, pp. 7165–7168, Dec. 1978.

[51] C. Göransson, W. Olovsson, and I. A. Abrikosov, "Numerical investigation of the validity of the Slater-Janak transition-state model in metallic systems," *Physical Review B*, vol. 72, Oct. 2005.

[52] S. Sanna, T. Frauenheim, and U. Gerstmann, "Validity of the Slater-Janak transition-state model within the LDA + U approach," *Physical Review B*, vol. 78, Aug. 2008.

[53] J. P. Perdew, R. G. Parr, M. Levy, and J. L. Balduz, "Density-functional theory for fractional particle number: Derivative discontinuities of the energy," *Phys. Rev. Lett.*, vol. 49, pp. 1691–1694, Dec 1982.

[54] L. J. Sham and M. Schlüter, "Density-functional theory of the energy gap," *Phys. Rev. Lett.*, vol. 51, pp. 1888–1891, Nov 1983.

[55] T. Stein, J. Autschbach, N. Govind, L. Kronik, and R. Baer, "Curvature and Frontier Orbital Energies in Density Functional Theory," *The Journal of Physical Chemistry Letters*, vol. 3, pp. 3740–3744, Dec. 2012.

[56] P. Mori-Sánchez, A. J. Cohen, and W. Yang, "Localization and Delocalization Errors in Density Functional Theory and Implications for Band-Gap Prediction," *Physical Review Letters*, vol. 100, Apr. 2008.

[57] C. Di Valentin, S. Botti, and M. Cococcioni, *First principles approaches to spectroscopic properties of complex materials*. 2014.

[58] K. Capelle, N. A. Lima, M. F. Silva, and L. N. Oliveira, "Density-functional theory for the Hubbard model: numerical results for the Luttinger liquid and the Mott insulator," in *The Fundamentals of Electron Density, Density Matrix and Density Functional Theory in Atoms, Molecules and the Solid State*, pp. 145–168, Springer, 2003.

[59] C. Persson and S. Mirbt, "Improved electronic structure and optical properties of sp-hybridized semiconductors using LDA+U SIC," *Brazilian journal of physics*, vol. 36, no. 2A, pp. 286–290, 2006.

[60] W. G. Aulbur, L. Jönsson, and J. W. Wilkins, "Quasiparticle Calculations in Solids," in *Solid State Physics* (H. E. a. F. SPAEPEN, ed.), vol. 54, pp. 1–218, Academic Press, 1999.

[61] J. Heyd, G. E. Scuseria, and M. Ernzerhof, "Hybrid functionals based on a screened coulomb potential," *The Journal of Chemical Physics*, vol. 118, no. 18, pp. 8207–8215, 2003.

[62] J. Paier, M. Marsman, K. Hummer, G. Kresse, I. C. Gerber, and J. G. ángyán, "Screened hybrid density functionals applied to solids," *The Journal of Chemical Physics*, vol. 124, no. 15, pp. –, 2006.

[63] A. Schleife, F. Fuchs, J. Furthmüller, and F. Bechstedt, "First-principles study of ground- and excited-state properties of MgO, ZnO, and CdO polymorphs," *Physical Review B*, vol. 73, June 2006.

[64] S. J. Pearton, C. R. Abernathy, M. E. Overberg, G. T. Thaler, D. P. Norton, N. Theodoropoulou, A. F. Hebard, Y. D. Park, F. Ren, J. Kim, and L. A. Boatner, "Wide band gap ferromagnetic semiconductors and oxides," *Journal of Applied Physics*, vol. 93, no. 1, p. 1, 2003.

[65] H.-J. Freund, "Introductory lecture: Oxide surfaces," *Faraday Discuss.*, vol. 114, pp. 1–31, 1999.

[66] L. Zhang, M. Kuhn, and U. Diebold, "Growth, structure and thermal properties of chromium oxide films on Pt(111)," *Surface Science*, vol. 375, pp. 1–12, Mar. 1997.

[67] H. H. Tippins, "Optical absorption and photoconductivity in the band edge of -Ga_2O_3," *Physical Review*, vol. 140, no. 1A, p. A316, 1965.

[68] H. Dixit, N. Tandon, S. Cottenier, R. Saniz, D. Lamoen, B. Partoens, V. Van Speybroeck, and M. Waroquier, "Electronic structure and band gap of zinc spinel oxides beyond LDA:$ZnAl_2O_4$, $ZnGa_2O_4$ and $ZnIn_2O_4$," *New Journal of Physics*, vol. 13, p. 063002, June 2011.

[69] W. Setyawan and S. Curtarolo, "High-throughput electronic band structure calculations: Challenges and tools," *Computational Materials Science*, vol. 49, pp. 299–312, Aug. 2010.

[70] C. Freysoldt, B. Grabowski, T. Hickel, J. Neugebauer, G. Kresse, A. Janotti, and C. G. Van de Walle, "First-principles calculations for point defects in solids," *Reviews of Modern Physics*, vol. 86, pp. 253–305, Mar. 2014.

[71] J.-H. Cha and H.-W. Choi, "Luminescence Characteristics of $ZnGa_2O_4 : Mn^{2+}, Cr^{3+}$ Phosphor and Thick Film," *Transactions on Electrical and Electronic Materials*, vol. 12, pp. 11–15, Feb. 2011.

[72] D. Errandonea, R. S. Kumar, F. J. Manjon, V. V. Ursaki, and E. V. Rusu, "Post-spinel transformations and equation of state in ZnG_2O_4: Determination at high-pressure by in situ x-ray diffraction," *Physical Review B*, vol. 79, Jan. 2009. arXiv: 1005.0264.

[73] S. Leyre, E. Coutino-Gonzalez, J. Joos, J. Ryckaert, Y. Meuret, D. Poelman, P. Smet, G. Durinck, J. Hofkens, G. Deconinck, and P. Hanselaer, "Absolute determination of photoluminescence quantum efficiency using an integrating sphere setup," *Review of Scientific Instruments*, vol. 85, no. 12, p. 9, 2014.

[74] M. Gaft, R. Reisfeld, and G. Panczer, *Modern luminescence spectroscopy of minerals and materials*. Springer Science & Business Media, 2005.

[75] G. Racah, "Theory of complex spectra. i," *Phys. Rev.*, vol. 61, pp. 186–197, Feb 1942.

[76] G. Racah, "Theory of complex spectra. ii," *Phys. Rev.*, vol. 62, pp. 438–462, Nov 1942.

[77] Y. Tanabe and S. Sugano, "On the absorption spectra of complex ions, iii the calculation of the crystalline field strength," *Journal of the Physical Society of Japan*, vol. 11, no. 8, pp. 864–877, 1956.

[78] Y. Tanabe and S. Sugano, "On the absorption spectra of complex ions. i," *Journal of the Physical Society of Japan*, vol. 9, no. 5, pp. 753–766, 1954.

[79] Y. Tanabe and S. Sugano, "On the absorption spectra of complex ions ii," *Journal of the Physical Society of Japan*, vol. 9, no. 5, pp. 766–779, 1954.

[80] R. C. Powell, *Physics of Solid-State Laser Materials*. Springer Science & Business Media, Mar. 1998.

[81] "TanabeSugano diagram," May 2015. Page Version ID: 660573603.

[82] Y. Freiman and H. Jodl, "Solid oxygen," *Physics Reports*, vol. 401, pp. 1–228, Nov. 2004.

[83] C. Kittel, *Introduction to Solid State Physics 8th Edition by Charles Kittel*.

[84] "A refinement of the crystal structure of gallium : Zeitschrift für Kristallographie - Crystalline Materials."

[85] A. W. Hull and W. P. Davey, "Graphical determination of hexagonal and tetragonal crystal structures from x-ray data," *Phys. Rev.*, vol. 17, pp. 549–570, May 1921.

[86] H. F. McMurdie, M. C. Morris, E. H. Evans, B. Paretzkin, W. Wong-Ng, L. Ettlinger, and C. R. Hubbard, "Standard x-ray diffraction powder patterns from the jcpds research associateship," *Powder Diffraction*, vol. 1, pp. 64–77, 6 1986.

[87] H. Wang, Y. He, W. Chen, Y. W. Zeng, K. Stahl, T. Kikegawa, and J. Z. Jiang, "High-pressure behavior of -Ga_2O_3 nanocrystals," *Journal of Applied Physics*, vol. 107, no. 3, p. 033520, 2010.

[88] K. Lejaeghere, V. Van Speybroeck, G. Van Oost, and S. Cottenier, "Error Estimates for Solid-State Density-Functional Theory Predictions: An Overview by Means of the Ground-State Elemental Crystals," *Critical Reviews in Solid State and Materials Sciences*, vol. 39, pp. 1–24, Jan. 2014.

[89] A. R. Phani, S. Santucci, S. Di Nardo, L. Lozzi, M. Passacantando, P. Picozzi, and C. Cantalini, "Preparation and characterization of bulk $ZnGa_2O_4$," *Journal of materials science*, vol. 33, no. 15, pp. 3969–3973, 1998.

[90] D. T. Morelli and G. A. Slack, "High Lattice Thermal Conductivity Solids," in *High Thermal Conductivity Materials* (S. L. Shindé and J. S. Goela, eds.), pp. 37–68, Springer New York, 2006.

[91] B. X. R. H. Cheng, "Characterization of the native Cr_2O_3 oxide surface of CrO_2," *Applied Physics Letters*, vol. 79, pp. 3122–3124, 2001.

[92] H. He, M. A. Blanco, and R. Pandey, "Electronic and thermodynamic properties of -Ga_2O_3," *Applied Physics Letters*, vol. 88, no. 26, p. 261904, 2006.

[93] A. Kushwaha, "Vibrational, elastic properties and sound velocities of $ZnGa_2O_4$ spinel," *Computational Materials Science*, vol. 85, pp. 259–263, Apr. 2014.